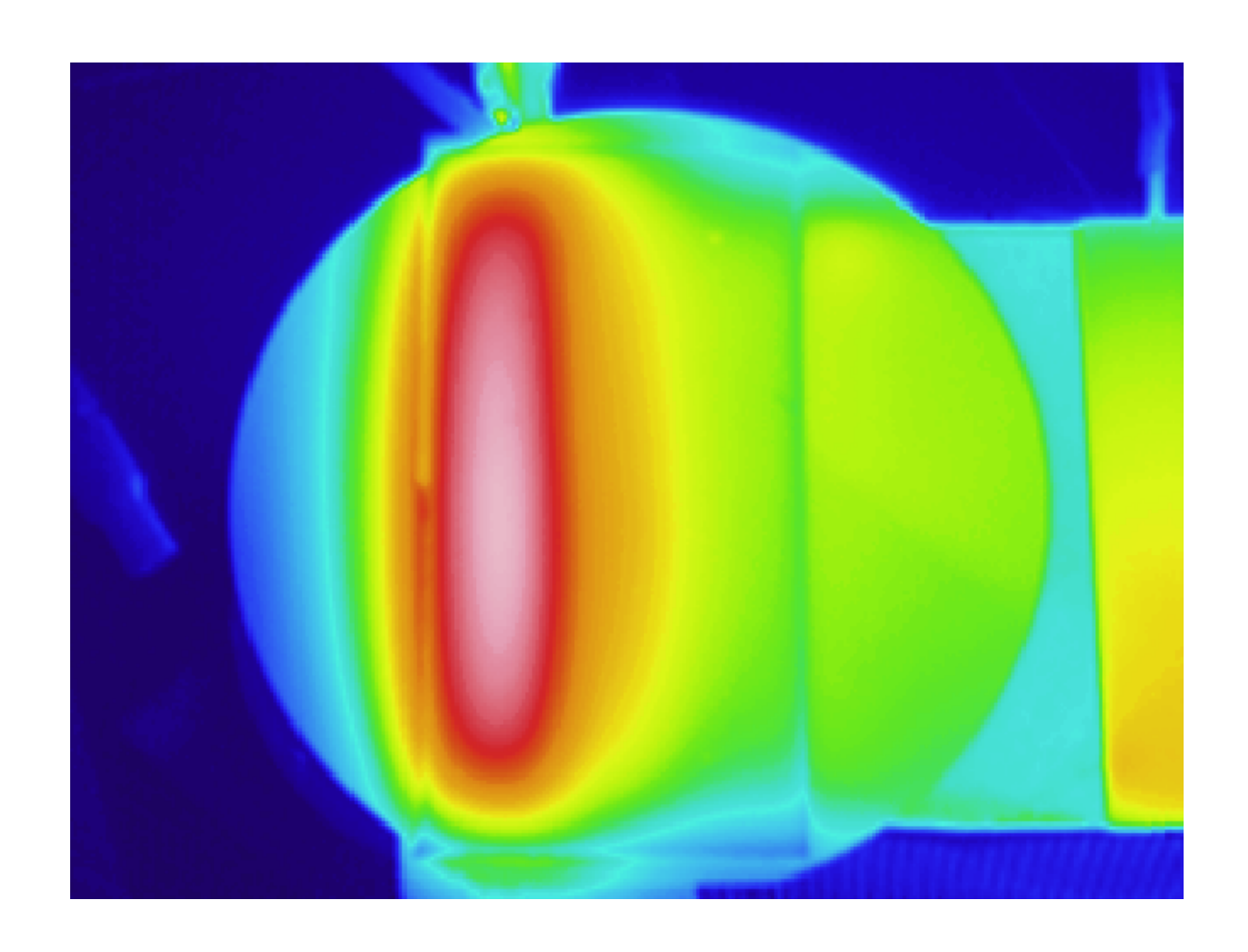
DESIGN AND FABRICATION OF A CONTINUOUS-FLOW PCR CHIP

13th of October 2025



Nanobiotechnology Department of Materials and Production, Aalborg University

Acknowledgements

This thesis would not have been possible without the help of our supervisors Evamaria Petersen and Leonid Gourevitch at Aalborg University, whose assistance has been invaluable.

We would also like to express our appreciation to faculty at the DTU institute, in particular Maria Dimaki, for arranging and coordinating use of the DTU cleanroom, and Elena Lopez Aymerich, for her assistance in navigating the DTU Nanolab and its equipment.



Aalborg University

Nanobiotechnology Fibigerstræde 16 Aalborg

Title:

Design and Fabrication of a Continuous-flow PCR Chip

Semester:

9th - 10th semester

Project period:

 3^{rd} of September 2024– 13^{th} of October 2025

Email:

lpe19@student.aau.dk

Supervisors:

Evamaria Petersen Leonid Gourevitch

Number of pages:

72

Number of pages in appendix:

1

Finish date:

13th of October

Abstract:

This paper examines a continuous-flow microfluidic PCR chip for its potential to enable the rapid generation of mutant DNA libraries. Traditional PCR methods, while foundational in molecular biology, are limited by lengthy thermal cycling times and expensive automation. Microfluidic PCR chips offer a promising alternative to achieve rapid thermal cycling and reduced reaction times. This project focuses on the design, fabrication, and optimization of a serpentine, continuous-flow PCR chip, using a resistive heater and a Peltier element to define the denaturation and annealing zones, respectively, and leveraging the inbetween gradient to form the extension zone. The chip design was modeled using COMSOL Multiphysics. Molds of the chips were fabricated using photolithography and deep reactive ion etching (DRIE), followed by polydimethylsiloxane (PDMS) casting and bonding to a glass substrate using plasma bonding. The chip's thermal performance was evaluated using infrared imaging, and PCR amplification was tested with various primer sets. Bovine serum albumin (BSA) was utilized to passivate the surface of the microchannels, limiting inhibition of *Taq* polymerase. The results highlight PDMS delamination, nonspecific primer annealing, and inhibition of PCR reagents as significant challenges to address.

Preface

This project is written by 3^{nd} & 4^{th} -semester master students from Aalborg University. The project was supervised by associate professors Evamaria Petersen and Leonid Gurevich. The project was written in the period of September 2^{ed} 2024, to October 13^{th} 2025. This project focuses on designing and fabricating a continuous-flow PCR chip. Furthermore, the concept of the continuous-flow PCR chip has been designed, simulated, fabricated, and further discussed.

The citation style used in this project was the IEEE style, and all references are summarized in the bibliography. The figures through this project were named figure "X.X" [example figure 2.1] like the tables were named table "X.X" [example table 2.1] and the equations "(X.X)" [example equation (2.1)].

Next generation tools were utilized for proofreading.

Aalborg University, 13th of October 2025.

Jimmi Mortensen	Lasse Strange Pedersen

Resumé

Dette studie undersøger en mikrofluidisk PCR-chip med henblik på dens potentiale til at muliggøre hurtig generering af mutant-DNA-biblioteker. Traditionelle PCR-metoder, selvom de er grundlæggende inden for molekylærbiologi, er begrænset af lange termiske cyklustider og dyr automatisering. Mikrofluidiske polymerasekædereaktion-chips tilbyder et lovende alternativ til at opnå hurtig termisk cyklus og reducerede reaktionstider. Projektet gennemgår den teoretiske baggrund af polymerasekædereaktion og fejl-tilbøjelig polymerasekædereaktion, fotolitografi og reaktiv ion ætsning, og giver et overblik over hvordan COMSOL Multiphysics-software kan simulere en mikrofluidisk chip.

I fokus for projektet er design, fremstilling og optimering af en slangeformet, kontinuerligstrømnings-polymerasekædereaktion-chip, der anvender en modstandsvarmer og et Peltier-element til at definere henholdsvis denaturerings- og annealing-zonerne og udnytter temperaturgradienten imellem til at danne extensionszonen. Chip-designet blev modelleret ved hjælp af COMSOL Multiphysics-software, med kanaldimensioner af 50x90 μ m, 70x90 μ m, og 90x90 μ m. Trykfaldet gennem chippen med 30 cyklusser er beregnet for tre væsker (vand, paraffin olie, og TMC-3283) til at drive væsken. På grund af manglende materiale data, blev olien Payrole Electra anvendt i simulationerne som erstatning for paraffin olie.

Støbeforme til chippene blev fremstillet ved hjælp af fotolitografi og dyb reaktiv ionætsning, efterfulgt af støbning i polydimethylsiloxan (PDMS) og binding til et glasunderlag ved hjælp af plasma-binding. Protokollerne for plasmid isolation, agarose gelelektroforese, og polymerasekædereaktion er præsenteret.

Chippens termiske ydeevne blev evalueret ved hjælp af infrarød kamera, og polymerasekædereaktion blev testet med forskellige primersæt. Bovint serum albumin (BSA) blev anvendt til at begrænse absorptionen af *Taq* polymerase. Resultaterne peger på PDMS-delaminering, uspecifik primer-annealing og absorberende reagenser som betydelige udfordringer, der skal overvindes. For at undgå brug af miljøskadelige specialolier, kan man designe chippen med større kanaler for at forhindre delaminering.

Contents

1	Intr	oduction	1
	1.1	Polymerase Chain Reaction	4
		1.1.1 Error Prone Polymerase Chain Reaction	7
	1.2	PCR Chip Inhibition	7
	1.3	Photolithography	0
	1.4	Etching	3
		1.4.1 Dry Etch	4
2	Chir	Design 2	1
_	-	COMSOL Model	
		2.1.1 COMSOL Physics	
		2.1.2 Meshing	
3			5
	3.1	Microfabrication	
		3.1.1 Etching	
		3.1.2 PDMS & Plasma Bonding	
	3.2	Experimental Setup	
	3.3	Bacterial Growth Medium	
	3.4	Chemical Transformation of <i>E. coli</i>	
	3.5	Plasmid isolation	
	3.6	Agarose Gel Electrophoresis	
	3.7	PCR in Tube	
	3.8	PCR on Chip	
	3.9	COMSOL Studies	3
4	Rest	ults & Discussion 3	6
	4.1	Mold Fabrication	.2
		4.1.1 Molds Fabrication & Investigation	
	4.2	Testing of Chips	.9
	4.3	Polymerase Chain Reaction	1
		4.3.1 Plasmid Isolation & PCR	1
		4.3.2 Color Assay	2
		4.3.3 PCR on a Chip	4
5	Disc	eussion 6	1
	5.1	The Design and Fabrication of the Chip	1
	5.2	Chip Delamination	
		5.2.1 PCR & UV	
		5.2.2 Inhibition	5

<u>C</u> c	Contents Aalborg Un			
6	Conclusion	67		
Bi	ibliography	68		
A	Appendix A.1 GeneJET Plasmid Miniprep Kit	A1		

Introduction 1

Polymerase Chain Reaction (PCR), developed by Kary Mullis in 1983, revolutionized molecular biology by providing a rapid, specific, and highly sensitive technique for amplifying defined segments of DNA from minimal starting material *in vitro*.[1] PCR mimics natural DNA replication through cycles of thermal denaturation, primer annealing, and enzymatic extension to exponentially amplify a target DNA sequence. Through just a few cycles of PCR, a single DNA molecule can be amplified to produce several million copies. The profound impact of PCR was recognized when Mullis was awarded the 1993 Nobel Prize in Chemistry, shared with Michael Smith, underlining the technique's transformative role in modern biosciences. [2, 3]

Following the invention of PCR, the development of dedicated thermal cycling instruments (thermocyclers) enabled the precise and reproducible control of temperature cycles, greatly improving the consistency of PCR reactions. In 1988, implementation of heat-resistant DNA polymerases derived from *Thermus aquaticus* i.e., *Taq* polymerase, eliminated the need to manually replenish the enzyme after each PCR cycle. The discovery of thermostable DNA polymerase enabled full automation of the process and facilitated the widespread adoption of PCR across molecular biology laboratories worldwide.[3, 4]

In the subsequent years, PCR technology underwent rapid diversification through the development of specialized variants tailored to distinct experimental needs. Hot-start PCR minimizes non-specific amplification by employing enzymatic inhibitors, such as antibodies or modifications of *Taq* polymerase, that suppress activity at low temperatures, thereby "hot-starting" the PCR reaction.[4] Real-time PCR (qPCR) introduced fluorescence-based detection systems that allow quantitative monitoring of DNA amplification during each cycle, providing a means for accurate nucleic acid quantification [5]. Multiplex PCR extended the technique's capacity by allowing simultaneous amplification of multiple target sequences within a single reaction, a capability that proved critical for applications in forensic DNA profiling and pathogen detection[6]. In parallel, isothermal amplification methods were developed as alternatives to conventional PCR. These techniques utilize enzyme-mediated strand displacement rather than thermal cycling to achieve DNA amplification at constant temperatures, making them particularly suitable for point-of-care diagnostic applications.[7–10].

Collectively, these innovations have established PCR as a foundational technology across diverse fields, including clinical diagnostics (infectious disease detection, genetic disorder screening) [11], and forensic science (DNA fingerprinting) [12].

Protein engineering, in particular, garnered interest and momentum once PCR was

established due to the potential applications.[13] Advances in protein engineering have resulted in a greater understanding of enzymatic functions, which have greatly contributed to pharmaceuticals, green chemistry, and biofuels. The subject of protein engineering started in the early 1980s as recombinant versions of natural proteins, using human insulin and producing it recombinant in other organisms.[14] Enzymatic reactions have gradually replaced novel traditional chemical reactions in catalytic systems due to their inherent advantages of high selectivity, environmental safety, mild reaction conditions, and simple reaction steps.[15]

Although naturally occurring enzymes have tremendous potential in biocatalytic synthesis, they may require alterations to be used in industrial applications. This may include improving protein thermostability or optimizing enzymatic activity for a specific reaction. The most effective ways to solve these problems are to locate novel enzymes with specific functionality in diverse environments, or to modify existing enzymes to obtain particular desired functionality. Compared to searching for and locating entirely new enzymes, it is relatively straightforward to transform known natural enzymes at the molecular level. [14–17]

Within protein engineering, two primary strategies have emerged for modifying enzymes: rational redesign and directed evolution. Rational redesign involves the deliberate introduction of specific mutations-typically through site-directed mutagenesis-to modify enzyme activity, stability, or substrate specificity. This approach requires detailed structural and mechanistic knowledge of the target protein; an incomplete understanding often leads to loss of function. In contrast, directed evolution relies on generating random mutations across the gene of interest, which makes it possible to generate a library of mutant DNA. This method mimics the principles of natural selection but operates over vastly shorter timescales, allowing for the rapid evolution of proteins with enhanced or novel properties [7].

Unfortunately, existing systems for streamlining and automating the generation of large mutant libraries are expensive, space-consuming, and require expertise.[18] However, PCR is not limited to conventional thermocyclers. Over the past three decades, PCR has been increasingly integrated into microfluidic platforms as they offer faster thermal response times and reduced reaction times. Furthermore, microfluidic platforms can be more easily automated.

1.0.0.1 Microfluidic PCR Chips

Traditional PCR relies on thermocyclers, where temperature cycling is constrained by the large thermal mass of both the sample and device. These systems typically achieve heating and cooling rates of only 1-2 °C/s, resulting in lengthy amplification times of 60-120 minutes for 25-35 cycles. [2, 19, 20]

To overcome this limitation, PCR has been adapted to microfluidic devices that feature a significantly higher surface-to-volume ratio (SVR). The enhanced heat transfer associated with smaller thermal masses enables faster temperature ramping and substantially reduces reaction times to tens of minutes. In such systems, the overall reaction duration primarily

depends on the number of thermal cycles and/or the flow rate required to achieve complete amplification. [19]

In 1998, Kopp *et al.* [21] demonstrated one of the first PCR microfluidic devices by employing a continuous-flow design with a serpentine channel layout. In this approach, the PCR mixture is injected into the chip and sequentially passes through spatially separated temperature zones analogous to those in conventional PCR. Using this configuration, a 10 μ L sample successfully completed 20 PCR cycles in just 90 seconds.

There are several microfluidic PCR devices used in the literature with differing designs and approaches, but the most common, which mimics the PCR process, can roughly be separated into three methods: Space domain PCR, Time domain PCR, and Digital PCR. Although other microfluidic devices exist, these make use of other DNA amplification techniques, such as isothermal nucleic acid amplification.

Space domain PCR devices operate by continuously moving the sample through spatially distinct temperature regions. Examples of these include the serpentine channel layout[21], using two or three heat sources[21–23], or radial design incorporating one heating source[24]. The temperature zones vary by design, having annealing and extension in the same temperature zone or divided into two separate zones. Some variants utilize oscillatory flow, where the sample repeatably moves back and forth between heating zones by syringe pumps[25]. Space domain PCR devices are typically simpler to design and implement compared to other configurations. [2, 26]

Time domain PCR devices, by contrast, more closely resemble conventional thermocyclers. Here, stationary samples in micro-chambers undergo active heating and cooling, and the temperature profile is controlled temporally rather than spatially. These systems require more sophisticated thermal management to achieve rapid and accurate temperature transitions of the small regions of the chambers.[2]

In digital PCR, the reaction mixture is partitioned into thousands of microliter or nanoliter-scale droplets (water-in-oil emulsions) or subchambers, each ideally containing zero or one copy of the target DNA sequence. Amplification within each partition allows for absolute quantification of the target DNA using fluorescent probes.[2, 27, 28]

Project Aim

Technological advances have enabled extensive automation of PCR, with thermocyclers and robotic liquid-handling systems minimizing manual intervention. Yet, these platforms are largely isolated from downstream applications of the amplified DNA. In enzyme engineering, for instance, random mutagenesis generates diverse variants, most of which lack improved function. [29] Identifying beneficial mutations requires multiple cycles of transformation, expression, and screening - processes that remain labor-intensive and low-throughput.

Integrating amplification, transformation, and screening into a continuous, automated

workflow would streamline this process, but conventional robotic systems are complex, expensive, and space-intensive. Given that these reactions typically occur at the microscale, microfluidic technologies offer a compact and efficient alternative.

Microfluidic PCR chips enable rapid thermal cycling, precise reagent handling, and the potential integration of downstream biochemical processes.[19] As such, they represent a pathway towards streamlining and automating the generation of large, diverse mutant libraries to accelerate the discovery of functional biomolecules and therapeutics.

The focus of this study is on continuous-flow microfluidic PCR, a form of space domain PCR, owing to its relative simplicity and potential for integration into lab-on-a-chip systems. A key challenge in such designs lies in maintaining uniform temperatures within each thermal zone. Temperature inconsistencies can lead to reduced product yield and non-specific amplification, issues that may be aggravated by prolonged exposure to denaturation temperatures or excessive transition times between heating zones.[20] Furthermore, PCR components within microfluidic environments are often susceptible to surface adsorption because of the inherently high surface-to-volume ratio of microchannels. This adsorption can inhibit the reaction by sequestering enzymes or nucleic acids, although the extent of this effect strongly depends on the materials and surface properties of the microfluidic device.[30, 31]

Project Goal

This project aims to develop a microfluidic PCR device capable of serving as a component in an automated library generation platform - a continuous-flow microfluidic PCR chip designed for DNA amplification.

1.1 Polymerase Chain Reaction

Polymerase Chain Reaction (PCR) is an *in vitro* DNA replication technique used to generate copies of a specific DNA fragment. Essentially, PCR is done with a mixture containing the DNA template, two different short single-stranded oligonucleotides called primers, defining the DNA fragment amplification, a DNA polymerase, the four deoxyribonucleotide triphosphates (dATP, dCTP, dGTP, and dTTP), a salt with a divalent cation (i.e., Mg2+), and a buffer with a simple salt with monovalent ions (i.e., Na+). PCR consists of three consecutive phases of denaturation, annealing, and extension. Upon completion of these steps, one copy of the DNA is synthesized[32, 33]; this is termed a PCR cycle and is typically repeated 25–40 times for 2 ^{25–40} copies. A PCR cycle is illustrated in figure 1.1. In each consecutive step, a specific biochemical process occurs, which is explained below.

During the denaturation phase, double-stranded DNA (dsDNA) is separated into single-stranded DNA (ssDNA). This process typically occurs at approximately 94 $^{\circ}$ C, where the stabilizing hydrogen bonds between complementary strands are disrupted. [33] Hydrogen bonds between DNA strands are highly specific. Each nucleotide consists of a phosphate group, deoxyribose sugar, and one of four bases: adenine (A), guanine (G), cytosine (C), or thymine (T). The genetic code depends on their linear sequence. According to the Watson–Crick model, adenine pairs with thymine (A = T) via two hydrogen bonds and

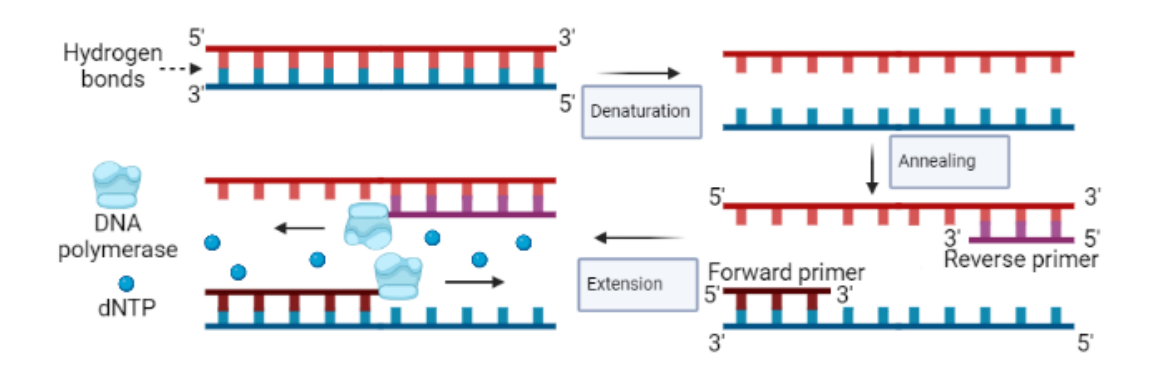


Figure 1.1: Main PCR steps. The double-stranded DNA is denatured, allowing a pair of primers to hybridize to single-stranded DNA. Lastly, the enzymatic polymerase, using deoxyribonucleotide triphosphates (dNTP) as building blocks, elongates the attached primer to synthesize a new DNA molecule. Created with Biorender

cytosine with guanine ($C \equiv G$) via three. Bases rarely bond outside their pairs, unless by modifications.[34, 35]

During the annealing step of PCR, synthetic single-stranded DNA oligonucleotide primers hybridize to their complementary sequences on the denatured DNA templates. The annealing temperature is usually set 3 to 5 °C below the melting temperature of the primer (T_m). T_m is defined as the temperature at which 50% of the primer–template duplexes are dissociated; a lower temperature ensures a higher percentage of hybridization, while still being specific.[35] The T_m is related to the properties of the primer sequence and is influenced by factors such as nucleotide composition, primer length, and the ionic strength of the reaction buffer. Monovalent cations (e.g., Na⁺, K⁺) stabilize the DNA duplex by shielding electrostatic repulsion between the negatively charged phosphate backbones, thereby enhancing primer–template stability. Oligonucleotide primers, generally 18–30 nucleotides in length, are designed to anneal to a specific target region with a free 3' hydroxyl group that serves as the initiation site for DNA polymerase–mediated extension.[32, 33]

Lastly, in the extension phase, DNA synthesis is catalyzed by a thermostable DNA polymerase, typically Taq polymerase. In this step, deoxynucleoside triphosphates (dNTPs) are incorporated sequentially at the primer's free 3' hydroxyl group, extending the primer into a strand by the polymerase. The effective extension rate of Taq polymerase under these conditions is approximately 60-100 bases per second at 72 °C.[34, 36] The catalytic mechanism of DNA polymerase uses magnesium ions (Mg^{2+}), which act as essential cofactors by forming a coordination complex between the components and stabilizing the transition state. The polymerase facilitates the nucleophilic attack of the primer's 3'-hydroxyl group on the incoming dNTP to extend the strand (see figure 1.2). [34]

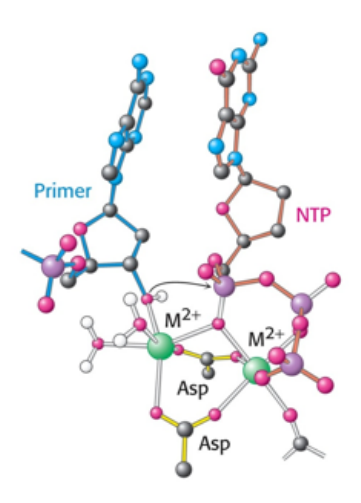


Figure 1.2: An illustration of the primer–polymerase–dNTP complex during PCR amplification. The Primer provides the existing 3'-OH group required for elongation. The DNA polymerase uses magnesium (Mg^{2+}) as a coordinate complex as it catalyzes a reaction between primer and dNTP. Adapted from [34]

Although the Taq polymerase exhibits maximal catalytic activity near 75–80 °C (see figure 1.3), the extension temperature is set lower to preserve the stability of the primer–template duplexes formed during annealing.[35] Although Taq polymerase is a thermostable enzyme, the half-time significantly decreases at temperatures above 94 °C, potentially decreasing the activity. [36, 37]

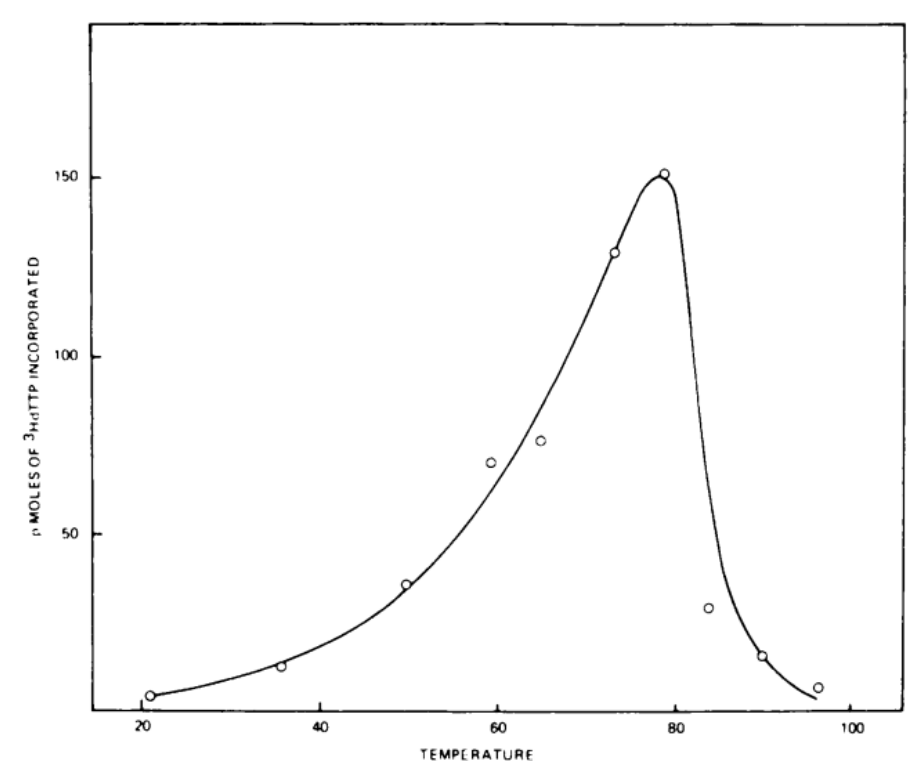


Figure 1.3: Effect of temperature on the activity of the DNA polymerase. DNA polymerase (0.02 U per assay) was incubated for 30 min in the standard reaction mixture at different temperatures. Fractions were then taken, and the conversion of [3H]dTTP into acid-insoluble material was measured. Taken from [37]

At elevated temperatures, above 80 °C, approaching the polymerase optimum, primer hybridization is prone to thermal dissociation, leading to incomplete or inefficient extension. The typical selected temperature of 72 °C ensures both robust enzymatic activity and sufficient primer–template stability to support continuous $5' \rightarrow 3'$ polymerization.

Despite this high degree of specificity, *Taq* polymerases occasionally incorporate mismatched nucleotides; for example, cytosine (C) can aberrantly pair with adenine (A) through the formation of two hydrogen bonds. Such misspairing events can give rise to mutations if left uncorrected and subsequently propagated during replication. The overall frequency of these errors is determined by the fidelity (or error rate) of the polymerase.[34]

1.1.1 Error Prone Polymerase Chain Reaction

Error-prone PCR (epPCR) is a modified PCR technique that aims to lower the fidelity of polymerase to introduce random mutations into a gene sequence. Taq polymerase is typically used due to its comparatively low fidelity (\sim 1 error per 10^5 nucleotides). Taq polymerase lacks the 3' to 5' exonuclease proofreading activity found in other polymerases, which prevents the mutations that occur during DNA replication from being "corrected". The fidelity is further reduced by using unbalanced dNTP concentrations or mutagenic buffers. [38]

Mutagenic buffers are made by replacing the physiologically relevant Mg⁺ ions that serve as co-factor for DNA polymerases, which generally reduces the fidelity of replication. The addition of manganese ions (Mn²⁺) to the PCR mixture in excess, [Mn²⁺] < 100 μ M, has been found to be the most mutagenic compared to other cations; Mn²⁺ increases the rate of incorporation of incoming dNTPs and decreases the equilibrium disassociation constant of [dNTP]. [39]

To achieve mutations, Xu *et al.* [16] suggests using a Mn-dITP PCR method. This method uses Mn²⁺ and 2'-deoxyinosine 5'-triphosphates (dITPs) to increase the miss-recognition and miss-pairing rate, respectively, of *Taq* DNA polymerase. The study achieved a mutation rate of 1–2 mutations per clone with a frequency of 33.3% AT \rightarrow GC, and 25% GC \rightarrow AT (transition), and 16.7% AT \rightarrow TA (transversion) . Other transversal mutations occurred with a frequency of 8.3%.

1.2 PCR Chip Inhibition

Inhibition is a recurring problem in microfluidic PCR chips. [26, 30, 31, 40, 41] Critical components such as DNA, polymerase, or other reagents of the PCR mixture tend to adsorb to the surface of the channel, decreasing DNA synthesis. [42] This is a significant issue compared to conventional PCR methods, which use thermo-cyclers and have a small surface of the reaction container relative to the volume of the PCR mixture. Microchannels, however, have a high surface-to-volume ratio (SVR), causing PCR components to adsorb to the channel surfaces and reducing yield along the chip. See figure 1.4. Additionally, carryover contamination from a previous PCR run can also be an issue, as contaminants desorb. [26, 30, 43]

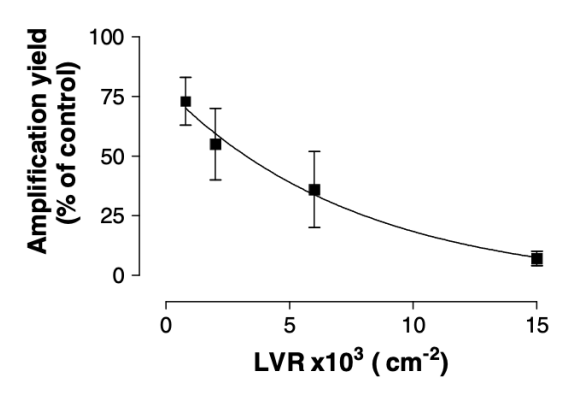


Figure 1.4: Inhibition of PCR yield as a function of length to volume ratio (LVR). PCR samples (20 or 50 μ L) were passed through purified PFA tubing of either 40 cm or 3 m to generate different LV ratios [30]

Several materials are utilized in microfluidics, mainly glass, polymers, and silicon, each with their own degree of adsorption of PCR components. [30, 31] Kodzius *et al.* [31] study investigated the PCR inhibition of primary inhibitory components (DNA and polymerase) when added to common materials for microfluidic devices, including SU-8, SiO₂, Pyrex, and PDMS, see figure 1.5. The study found that adsorption to SiO₂ and Pyrex and PDMS do not have strong PCR inhibitory effects. Specifically, SU-8 was found to be a strong DNA inhibitor, even with the addition of bovine serum albumin (BSA), a commonly used uninhibiting additive (figure not included).

Several surface passivation applications have been utilized to dampen PCR inhibition. Surface passivation may be categorized as passive- and dynamic coatings techniques. In passive coatings, chemical or biological molecules are applied to the microchannel surface prior to the PCR reaction, typically in the fabrication process. There are two methods to passively coat microchannels. Either in the fabrication process, adding a thin layer of a material such as silicon oxide, or silanization of the inner surfaces of the microchannels with a PCR friendly substance. However, silanization is not favored, as it is time-consuming and tedious.[19, 43, 44] A study by Crabtree *et al.* [42] soaked PDMS microchannels in a 1% BSA solution for one hour. The PCR yield, shown as signal-to-noise ratio, increased by 10-40x. When comparing the time spent to enable the silanization of the microchannels and running the PCR process to a conventional PCR, the time savings are negligible.

Additionally, a study by Christensen *et al.* [41] showed that washing the microchannels after silanization results in a significantly decreased PCR efficiency as the passive coat loses its effect, limiting the re-usability (see figure 1.6).

In contrast, dynamic-coating additives are included in the PCR reaction mix. Commonly used dynamic coating additive in PCR microfluidic devices are BSA, polyvinylpyrrolidone (PVP), polyethylene glycol (PEG), and Tween 20. The advantage of dynamic coatings is that they are reapplied with each PCR run. [19, 31, 40, 41, 44, 45]

Of the aforementioned dynamic coating substances, BSA is especially advantageous in the PCR reaction. BSA is often included in the PCR mixture to improve the PCR yield

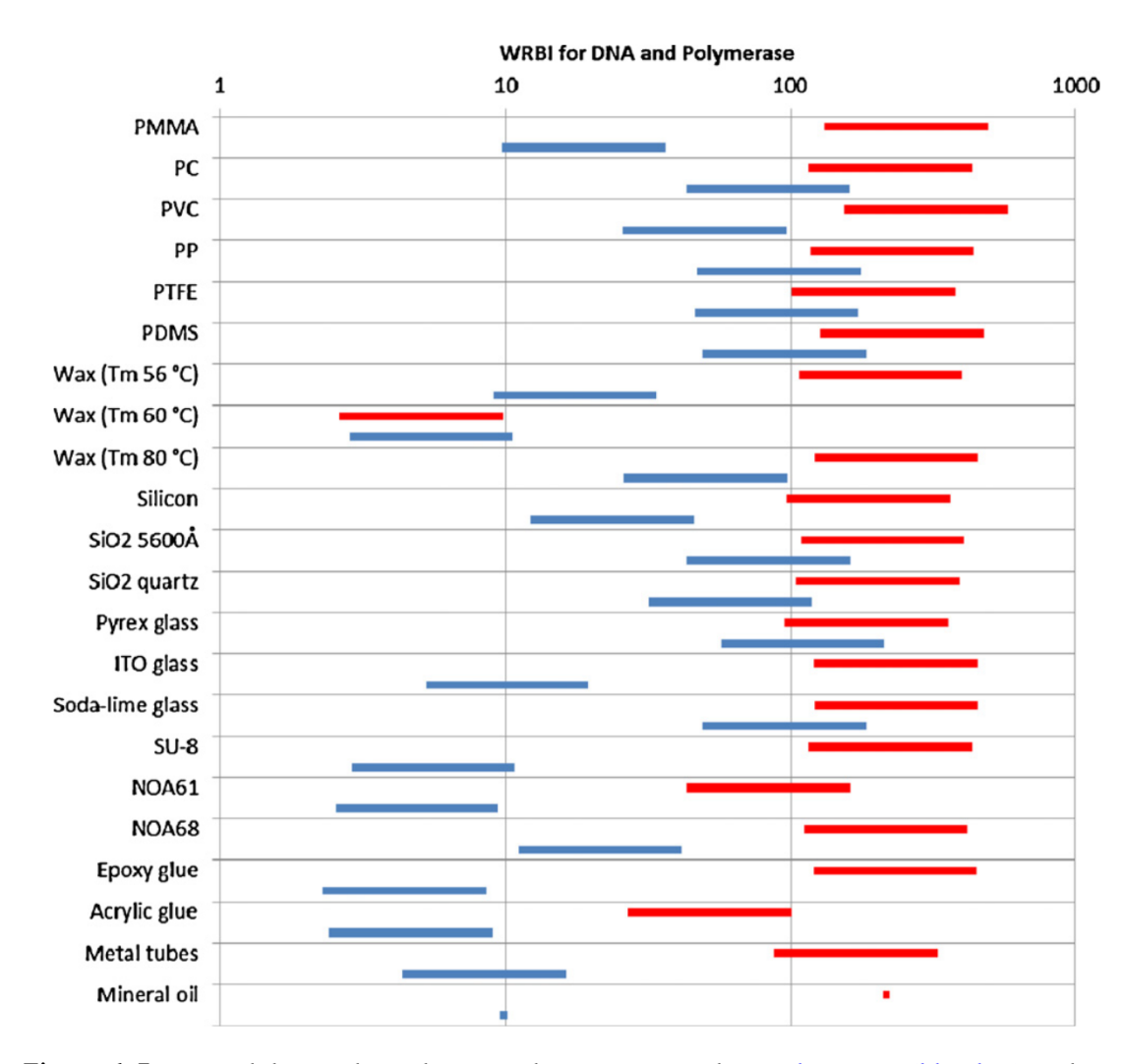


Figure 1.5: PCR inhibition through material interaction with template DNA (blue bar) and DNA polymerase (red bar). The DNA polymerase or template DNA was added after the rest of the PCR mixture had been incubated with the material under test. This was to avoid interaction between the material under test and the DNA polymerase or template DNA. The calculated WRBI (Weighted Relative Band Intensity) range is indicated for each material. WRBI is the ratio between "relative band intensity to "surface area-to-volume ratio". Lower WRBI values indicate inhibition, whereas higher WRBI values mean less inhibition [31].

in microchannels, as BSA competes with polymerase adsorption at the channel walls. When BSA adsorbs to a material such as cured PDMS, the contact angle of the surface becomes hydrophilic. Additionally, BSA facilitates primer annealing, stabilizing DNA and polymerase, acting as an osmo-protectant.[19, 31]

However, even with the advantages of BSA, the yield from the PCR reaction may not necessarily be as great as that of other dynamic coating additives. A study by Chen and Qiu [43] tested a PDMS/glass microfluidic chip with several passivation chemicals in the PCR mixture, such as BSA, PVP, and Tween 20. Of the chemicals tested, the PCR mixtures with Tween 20 showed a higher PCR yield, followed by PVP and BSA, with the lowest PCR yield. The concentrations of PVP and BSA were 1 and 2 mg/ml, and Tween 20 was 10% and 20%.

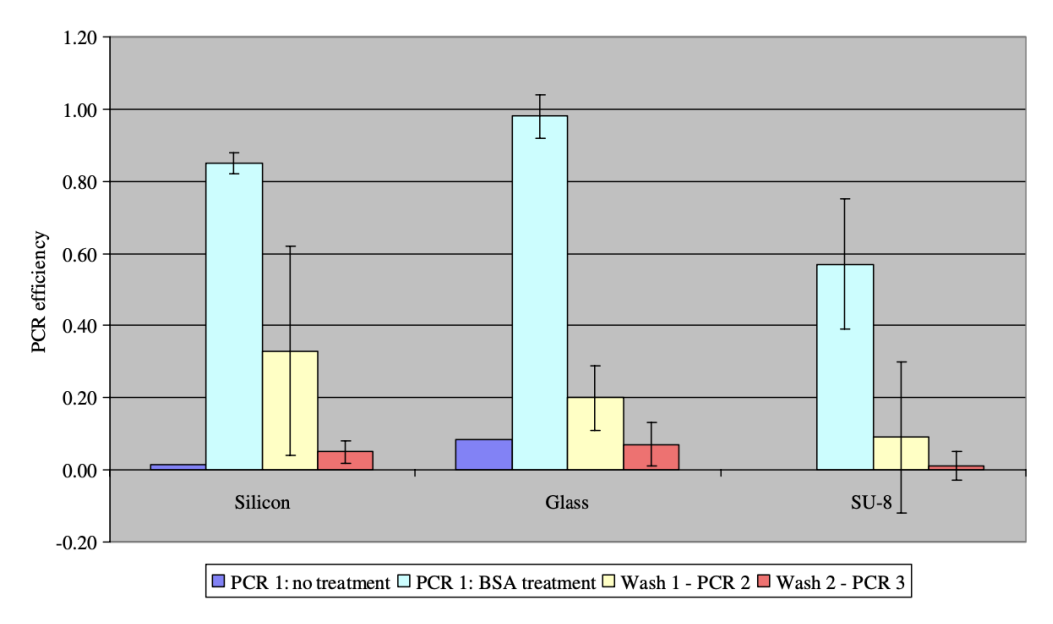


Figure 1.6: The PCR efficiencies after initial BSA treatment and two subsequent washing steps are shown. For comparison, the PCR efficiency with a non-treated sample is also shown. For all three materials, a significant decrease in PCR efficiency is observed after the washing steps, indicating that the BSA can be washed off the materials [41].

In summary, although BSA provides several functional advantages in PCR microfluidic systems; including suppression of polymerase adsorption, enhancement of surface hydrophilicity, and stabilization of reaction components, its efficiency in yield improvement appears limited when compared to alternative dynamic coatings such as Tween 20 and PVP, particularly under the tested concentration conditions. However, this may depend on the PCR chip used.

1.3 Photolithography

Photolithography is a microfabrication technique used to define and transfer highly precise patterns in the micro- to nanometer-scale onto a variety of substrates, including metals, oxides, nitrides, and semiconductors such as silicon and its derivatives. [46–48] The photolithographic process (often followed by an etching sequence) consists of three primary steps; resist coating, exposure, and development. These are schematically illustrated in figure 1.7.[46–48]

Preparing the substrate with an adhesion promoter is critical to ensure effective bonding of the photoresist to a cleaned surface. The substrate is first subjected to thermal dehydration to eliminate atmospheric moisture, leaving a thin layer of native silicon oxide. This oxide layer allow for subsequent reactions between the surface and the adhesion promoter. A widely used promoter is hexamethyldisilazane[(CH₃)₃Si]₂NH (HMDS). The chemical reaction between HMDS and the silicon oxide surface is illustrated in figure 1.8. The native silicon oxide is exposed to HMDS vapor under heat, where the hydroxyl (OH) groups on the oxide surface replace the amine of HMDS and bond with the trimethylsilyl groups, releasing ammonia. This surface methylation increases the hydrophobicity, thereby enhancing the adhesion of a hydrophobic photoresist.[46]

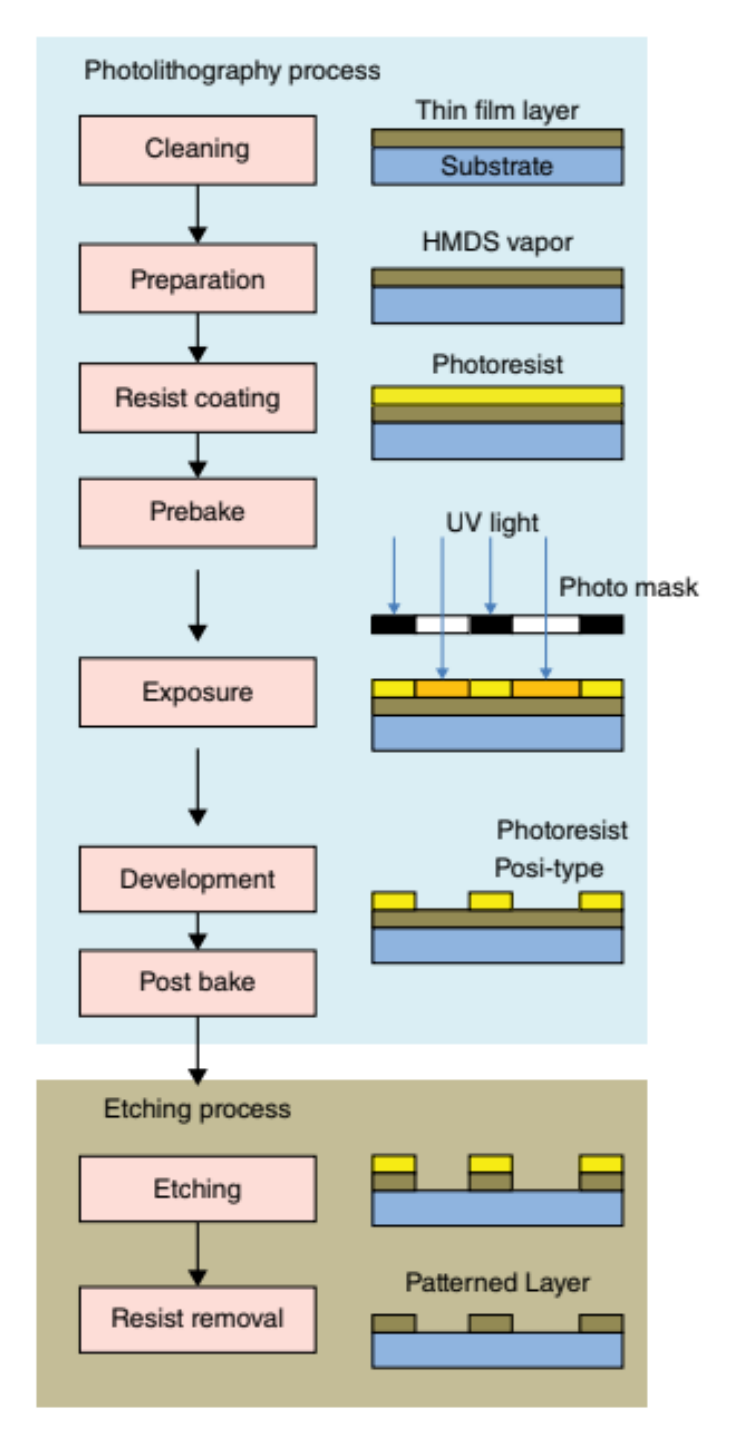


Figure 1.7: Overview of the general photolithography and etching process flow.[47]

After the adhesion promoter has reacted with the substrate and any excess has evaporated, a liquid photoresist layer is applied by spin coating to achieve a uniform film distribution. The resist may be dispensed either statically (onto a stationary wafer) or dynamically (onto a rotating wafer). During spin coating, the substrate is accelerated to high rotational speeds, generating centrifugal forces that spread the resist across the wafer surface while simultaneously removing excess material. This process results in a thin, uniform resist film, typically on the order of a few micrometers in thickness. The final film thickness is inversely correlated with the spin speed, acceleration, and spin duration. Empirically

Figure 1.8: a) Thermal dehydration of a hydrated native oxide on a silicon substrate, and b) The adhesion-promoting agent, hexamethyldisilazane (HMDS), forms a water-resistant film on the surface of a wafer that prevents developer from undercutting the resist during the development process. [46]

derived spin curves, specific to the photoresist formulation, are commonly employed to determine optimal parameters for achieving the desired coating thickness. A soft bake is performed to dry the resist by evaporating excess residual solvent on a heated plate. [46–48]

Following the soft-bake, the coated substrate is exposed to ultraviolet (UV) radiation to induce crosslinking through a photomask containing the desired pattern for transfer. Photoresists are broadly categorized as either positive or negative, depending on their response to UV irradiation. This is related to the following step of development, where a developer solution is used to remove undesired parts of the resist. In positive resists, the unexposed regions remain relatively insoluble in the developer solution, whereas the exposed regions undergo photochemical decomposition, rendering them soluble. Conversely, negative resists exhibit the opposite behavior: the unexposed regions remain soluble, while the exposed regions become insoluble due to UV-induced crosslinking or polymerization, which significantly enhances their resistance to the developer. [46, 47]

Many resists require a post-exposure bake (PEB) following exposure to promote additional chemical reactions or diffusion processes within the resist. PEB is particularly important for improving sidewall quality in the resist profile, which can otherwise be degraded by interference effects during exposure. For example, in resists such as AZ MiR 701, interaction between incident and substrate-reflected light can give rise to standing waves, resulting in periodic variations along the resist sidewalls after development. Performing a PEB enables the diffusion of the activated photoactive compound (PAC) along its concentration gradient into adjacent unactivated regions, thereby mitigating standing-wave effects and producing smoother sidewalls. [46, 48, 49]

Specific resists require a post-exposure bake (PEB) step following exposure to promote additional chemical reactions or diffusion processes within the resist. PEB affects how the resist functions in the later development step. PEB of chemically amplified resists (CARs) will initiate the few photoacids created in exposure, to catalyze chemical reactions of the resist polymer, resulting in polymer solubility in development. [50] Some negative resists require PEB to increase crosslinking of exposed areas, making it insoluble for the later step of development. For some positive resists, PEB is particularly important for improving sidewall quality in the resist profile, which can otherwise be degraded by interference effects during exposure. For example, in resists such as AZ MiR 701, interaction between incident and substrate-reflected light can give rise to standing waves, resulting in periodic variations along the resist sidewalls after development. Performing a PEB enables the diffusion of the activated photoactive compound (PAC) along its concentration gradient into adjacent unactivated regions, thereby mitigating standing-wave effects and producing smoother sidewalls. [46, 48, 49]

The subsequent step is development, in which the photoresist-coated substrate is immersed in a developer solution designed to selectively dissolve the soluble regions of the resist, thereby transferring the photomask pattern onto the substrate. Modern lithographic processes typically employ metal-ion-free developers to prevent contamination that could compromise device performance or long-term reliability. The most common is based on tetramethylammonium hydroxide (TMAH). TMAH is particularly effective because of its strong alkalinity, which facilitates the dissolution of soluble photoresist polymers. Unlike metal hydroxides, TMAH does not introduce mobile ionic species that can diffuse into semiconductor devices and degrade their electrical characteristics. [46–48] The common method for resist development is the puddle process, in which the developer solution is dispensed onto the substrate, creating a puddle.

Following development, a hard bake (or post-bake) is typically performed to remove residual solvents, volatile organics, and absorbed moisture from the photoresist. This thermal treatment densifies and stabilizes the resist, thereby improving its mechanical strength, adhesion, and resistance to chemical or plasma attack during subsequent fabrication steps such as etching and ion implantation, while maintaining integrity in a vacuum.[46, 47]

Although optional, measurement and inspection are critical process-control steps to verify that the patterned resist features meet the specifications, detecting defects, and ensuring proper alignment. This ensures that the substrate is ready for further processing in subsequent etching or pattern transfer methods. [46]

1.4 Etching

The pattern in the resist is transferred onto the underlying substrate through either wet or dry etching techniques. In wet etching, liquid-phase chemical reagents (commonly acids) selectively dissolve the exposed substrate material. In contrast, dry etching relies on gaseous species in a plasma at low temperatures to etch the substrate via chemical reactions, physical ion bombardment, or a combination of both. The primary distinction

between these approaches lies in their etch profiles. Wet etching is generally isotropic, resulting in uniform material removal in all directions, whereas dry etching can be either isotropic or anisotropic, with the latter enabling directional etching essential for high-resolution pattern transfer in micro- and nanoscale fabrication. [47, 51, 52]

1.4.1 Dry Etch

A common problem with isotropic dry etching is the occurrence of undercutting, wherein material is removed laterally beneath the resist mask. This effect alters the transferred pattern, leading to deviations in the final substrate feature dimensions relative to the original resist design. Consequently, anisotropic dry etching is often preferred, as it enables highly directional material removal and the formation of sidewalls that are nearly vertical.[47, 51, 52] A schematic comparison of the resulting etch profiles for isotropic and anisotropic processes is presented in figure 1.9.

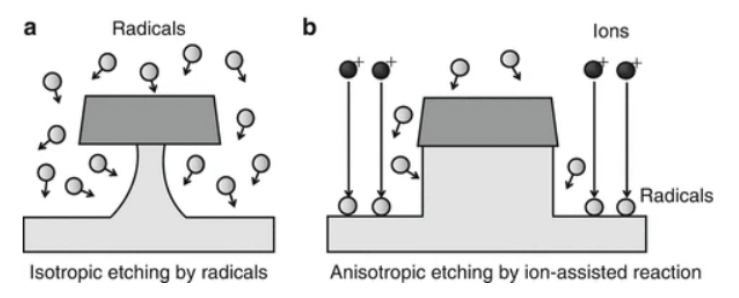


Figure 1.9: Concept of isotropic and anisotropic etching. Radicals etch in all directions, while ions can assist in directional etching, used in dry etching.[52]

The dry etching mechanism can be sorted into four steps: (i) ions and radicals are formed in the plasma. (ii) These species are transported to the substrate; ions are directed almost vertically towards the substrate, whereas radicals perform Brownian motion. (iii) Both adsorb to the surface of the substrate and react, forming etch products. (iv) The by-products desorb.

1.4.1.1 Weak Ionized Plasma - Dry Etch

Plasma is generated in a pressurized vacuum chamber between two electrodes. When a radio frequency (RF) power is applied, electrons are accelerated by the resulting electric field and collide with neutral gas molecules in the chamber. If the electron energy exceeds the ionization energy of the molecule, the collision produces positively charged ions and additional free electrons; electron-induced dissociation generates more accelerated electrons. The resulting cascade sustains a weakly ionized plasma, in which typically less than 0.01% of gas molecules are ionized. The electron and ion densities are roughly equal and are referred to as the plasma density. Plasma density typically ranges from $10^{-9} - 10^{-12} cm^{-3}$ and the ionization degree of $10^{-4} cm^{-3}$. However, this depends on the pressure and the number of gas molecules.[47, 52]

1.4.1.2 Collisions in Plasma

Electrons that have gained energy in plasma undergo various types of collisions with atoms and neutral gas molecules. These collisions are termed elastic and inelastic collisions. Elastic collisions transfer kinetic energy without altering the internal energy of the molecule with which they collide, whereas inelastic collisions involve energy transfer, leading to internal excitation, resulting in excitation, ionization, and dissociation. The primary mechanisms responsible for etching are ionization and dissociation, generating ions and radicals, respectively.[47, 51–53]

Excitation: The energy provided by the colliding electron enables a bound electron to jump to a higher energy level. The excited state is highly unstable and exists only for around 10 ns before returning to its ground state. During this transition, a photon is emitted, causing the identifiable plasma glow.

Ionization: An electron is expelled from the outermost electron shell if the energy of the colliding electron is higher than the ionization voltage[52], resulting in the following simple reaction: $A + e^- \longrightarrow A^+ + 2e^-$ Ion Electron

Dissociation: If the kinetic energy provided by the collision is greater than the binding energy of the molecule, the molecule is split. This results in the formation of volatile radicals. [52]

1.4.1.3 Reactive Ion Etching

In dry-etching systems, a widely adopted approach is reactive ion etching (RIE). The configuration consists of an upper and a lower electrode plate, with the lower electrode coupled to a blocking capacitor. When an RF frequency is applied to the electrodes, most commonly at 13.56 MHz, an electric field is created between the plate electrodes. At this frequency, the electric field rapidly changes direction; approximately 13.56×10^6 times per second. Due to their relatively large mass, ions and neutral species cannot respond effectively to the rapid oscillations of the electric field and instead undergo random thermal motion within the plasma. In contrast, electrons, being nearly four orders of magnitude lighter, can follow the oscillating field and periodically strike the electrodes.[52]

The blocking capacitor induces a negative self-bias potential on the lower electrode due to charge imbalance. This time-averaged potential, known as the DC bias (V_{DC}) , generally ranges from tens to hundreds of volts depending on the applied RF power. As a result, the lower electrode remains predominantly negative during the RF cycle (see figure 1.10), repelling most electrons and forming an ion sheath region that is largely depleted of electrons, see figure 1.11. Because of this depletion, electron-driven collision reactions in the sheath are suppressed. [47, 52, 53]

The plasma bulk is quasi-neutral, highly conductive and, therefore, approximately equipotential, characterized by the plasma potential (V_p) . At the sheath-plasma boundary,

positive ions experience acceleration toward the negatively biased electrode under the potential drop ($-V_{DC}$). The ions thus acquire a kinetic energy of $V_{DC}+V_p$, with a direction towards the lower electrode. The resulting ion bombardment etches the substrate.[51, 52]

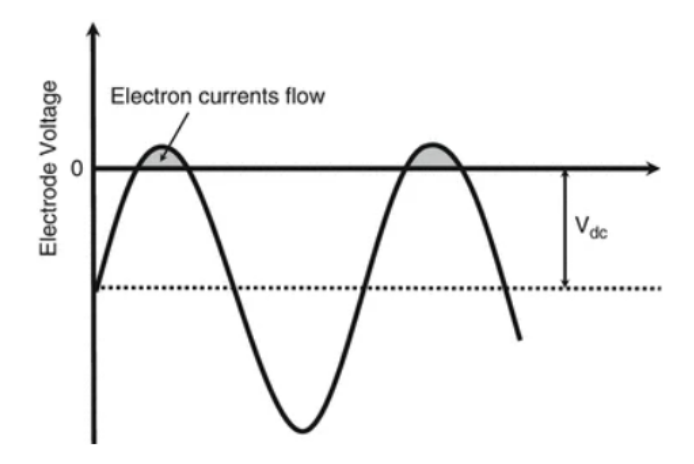


Figure 1.10: This time-averaged potential, known as the DC bias (V_{DC}) at the lower electrode plate.[52]

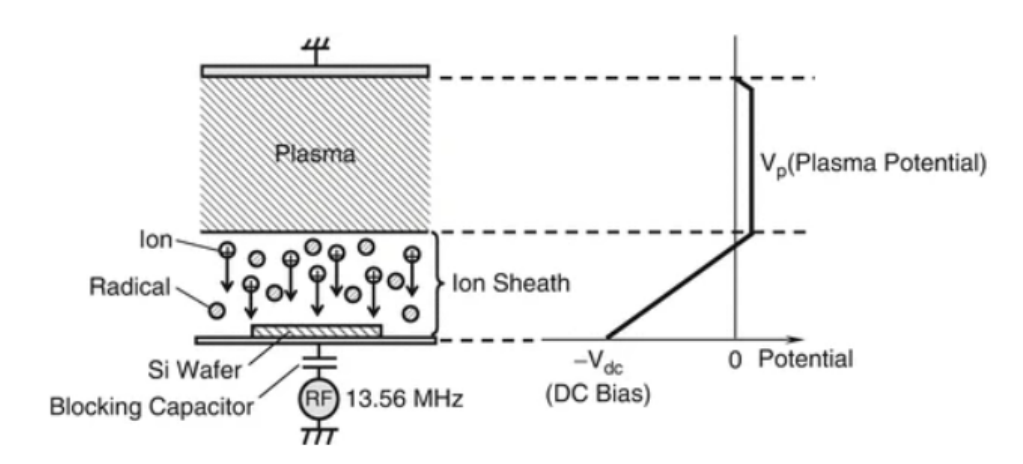


Figure 1.11: The potential between the electrodes, consisting of positive V_p across the plasma, and negative towards the lower electrode due to V_{DC} . [52]

The etch mechanism is dependent on the species generated in the plasma. If primarily ions are formed, the result is an anisotropic etch in the vertical direction, as opposed to the isotropic etch achieved by radicals diffusing and adsorbing to the substrate's surface at random. The etch rate produced by physical ion bombardment scales with the incident ion energy. In reactive ion etching (RIE), ion-assisted etching is the dominant process, as it enables anisotropic profiles by combining directional ion bombardment, which activates surface sites, with chemically reactive radicals that drive etching at higher rates. This synergistic interaction between physical and chemical effects is the primary mechanism governing dry etching.[51, 52]

Ion-assisted etching can generally proceed via two mechanisms: energetic or passivation-mediated. In the energetic mechanism, incident ions bombard the substrate surface, transferring momentum and breaking chemical bonds, which facilitates radical-induced surface reactions. When ion energy strongly influences the etch rate, this process is referred to as energetically ion-assisted etching. Under such conditions, increasing ion energy significantly accelerates etching, as ion irradiation enhances both the activation of surface sites and the reactivity of adsorbed radicals.[47, 52]

As ion bombardment largely targets the horizontal surfaces and breaks the horizontal protective layers, vertical passivation is maintained, resulting in the desired anisotropic etch direction, and etching by radicals is limited in the horizontal direction and is thus suppressed. The effectiveness of ion-assisted anisotropic etching depends strongly on the specific combination of etch gases and substrate materials. For example, in the etching of silicon (Si) by halogen species (F^+, Cl^+, Br^+) , the role of ion energy varies significantly. Etching driven by Cl^+ and Br^+ ions exhibits a strong dependence on ion energy, whereas F^+ -induced etching is comparatively less sensitive to increases in ion energy. When the etch rate is only weakly dependent on ion energy, the process is primarily governed by neutral radicals rather than ions. In such cases, passivation ion-assisted etching is employed. This approach introduces a protective gas that dissociates in the plasma and deposits a polymer-like passivation layer onto the substrate surface. Ion bombardment preferentially removes this passivation layer from horizontal surfaces, exposing them to radical attack, while the vertical sidewalls remain protected. As a result, lateral etching by radicals is suppressed, and anisotropy is achieved through selective preservation of the vertical passivation. [47, 51, 52]

1.4.1.4 **RIE Issues**

The chamber pressure during a RIE process is crucial. With higher pressure, the increased density of neutral species in the ion sheath increases the rate of collision and causes more ion scattering (scattering can be formulated as the relationship between the sheath distance d_{is} and the mean free path λ). See figure 1.12. RIE pressure is about 1-100 mTorr (or 0.133-13.33 Pa).

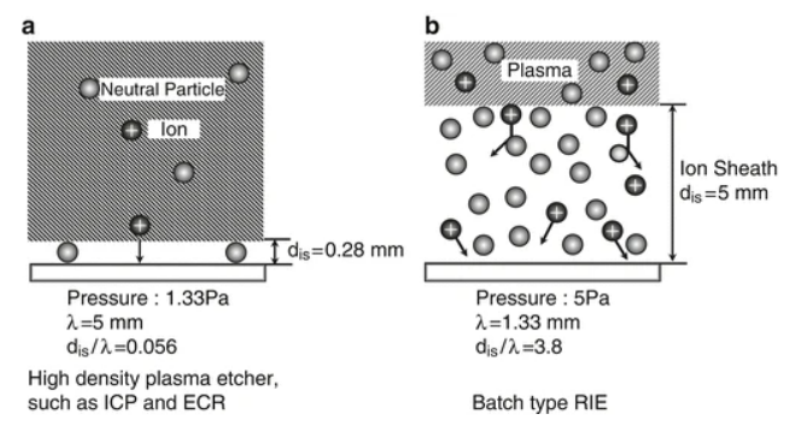


Figure 1.12: Ion scattering in the ion sheath due to pressure and ion sheath height. Taken from [52]

As a consequence, the etch rate of fine patterns and small mask openings is limited (see figure 1.13), as fewer ions can enter. This effect is typically referred to as RIE lag and occurs when a lower concentration of reactive species that reaches the bottom of narrow mask patterns. This can be alleviated by entering the low-pressure regime.

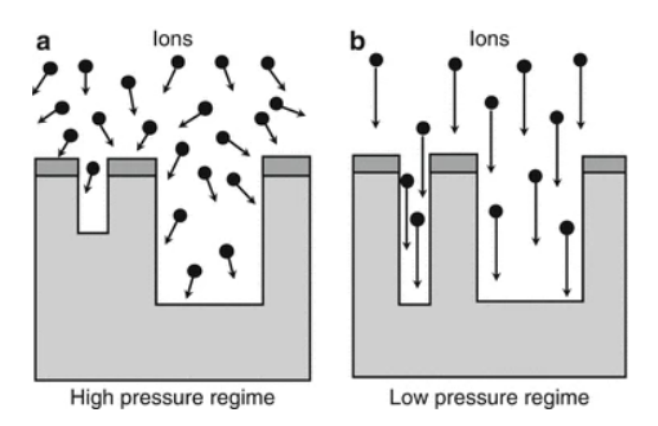


Figure 1.13: Effect of the ion directionality in fine patterning resists, in high and low pressure regimes. Taken from [52]

Additionally, the already limited ions entering small openings of the resist can collide with etching by-products, restricting the movement of the ions further to the trench bottom and the inability of etch by-products from leaving. Collisions with radicals are also a possibility, and can result in changes in the dependence in profile shape. [52, 54]

1.4.1.5 DRIE & the Bosch Process

Deep reactive ion etching (DRIE) is an alternative dry etching technique with several advantages over RIE. The Bosch process is a DRIE technique with process parameters that achieve high etch rate, high aspect ratio, straight sidewalls, and small sidewall scalloping. This Bosch process is a cyclic process consisting of three steps: passivation of the sidewalls (deposition), removal of the protective layer specific surfaces by ions (break), and radical reaction (etch). [51, 55]

The passivation step is achieved by introducing a gas such as C_4F_8 . In plasma, several dissociation reactions of the molecular ring C_4F_8 occur, resulting in radical CxFy fragments, which reassemble into a polymeric film that is deposited on the substrate surface. The key dissociation reaction is not agreed upon, but the fluorine-to-carbon ratio is typically 1.2-1-6 with a CF_2 concentration of 27-35% when power is increased. The break step refers to the removal of the passivation layer on horizontal surfaces through ion bombardment at low pressure, while the passivation polymer is left on the vertical surfaces. This protects the side walls during etching, when an etching gas such as SF_6 is introduced. Similarly to C_4F_8 , the dissociation reaction of SF_6 can result in several fragments, such as the following reaction [52, 54, 56]:

 $SF_6^- + e^- \longrightarrow 2e^- + SF_5^+ + F^-$ The products are meta-stable SF_5^+ , and the reactive etching species F^{\bullet} adsorbs to, and reacts with, the surface of silicon. The resulting product desorbs from the surface, removing the silicon. See the following reaction.

$$Si \xrightarrow{+} 4F \xrightarrow{-} SiF_4$$

Substrate radical gas

The Bosch process can be illustrated as in 1.14.

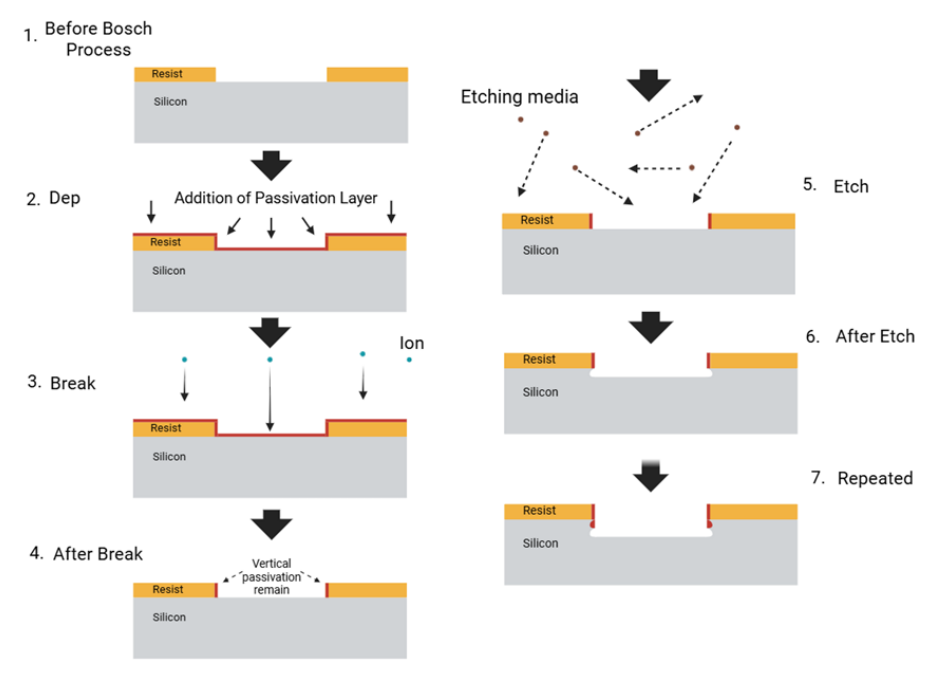


Figure 1.14: Concept of the Bosch Process, illustrating the substrate during, and after each step of Dep, Break, and Etch. Unlike the illustration, in reality, the (photo)resist is also etched, but this is negligible for only two cycles.

The break and etch steps are separate in the Bosch process to prevent the passivation and etch gases from reacting. Bates *et al.* [57] reported that the addition of C_4F_8 to SF6 plasma reduces the availability of F radicals, while also increasing the deposition of the passivation film.

1.4.1.6 Bosch Process Parameters

The relevant parameters of the Bosch Process are the choice of passivation and etching gases, the chamber pressure, and the platen and coil powers. The coil power is related to the control of species generated in the plasma. During the deposition phase, the passivation gas is introduced under medium pressure. In the break step, the pressure is lowered to maximize the inelastic mean free path of the ions, because potential gasmolecule collisions would change the ion impact angle. The platen power driving the electric field is also increased. [52] Lastly, the etch step increases the amount of the etching gas to improve the etch rate, platen power is lowered, and pressure is increased, allowing fluorine radicals to be the primary factor of etching. [51]

Oxygen can also be added to the plasma (< 5%) to the SF6 plasma, as it increases the density of F atoms, while also decreasing the probability of recombination of F atoms with ion species, which O_2 can disassociate and react with SF_x radicals. At higher O_2 (>7.5%), F-atoms are consumed to form Si_xO_yFz on the surface of the substrate, passing

the surface, and the etch rate is affected by the thickness of this layer. [53]

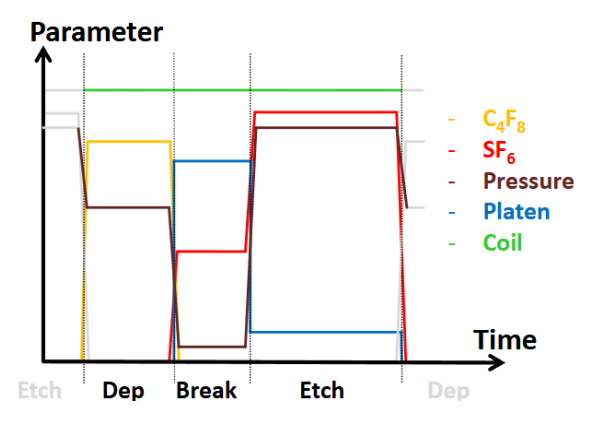


Figure 1.15: Bosch Process parameters during each step: Dep, Break, and Etch.[51]

After etching, the photo resist and vertical passivation polymer are removed using a chemical solution.[47]

1.4.1.7 Deep Etching Effects

The etch profile is linked to the etch rate. A low etch rate is favored for achieving low etch depth in a substrate, allowing a more controlled and precise etch. High etch rate, however, is preferred for deep etch samples, achieving fast etching, but at the cost of precise etch depth. Fluorine radicals are known to be highly reactive with silicon, in comparison to other halogen radicals, such as bromine and chlorine, and are thus widely used to achieve a fast etch rate. In addition, the etch rate depends on a phenomenon called the loading effect (or just loading). Because radicals are limited in the system, a larger exposed area in need of etching results in a slower etch rate as radicals are consumed due to an excessive substrate pattern. This can result in the photo resist being stripped away before by ion bombardment, before it reaches the desired depth. [51–53]

Chip Design 2

The chip employs a serpentine design to guide the PCR mixture through three temperature zones that correspond to the denaturation, annealing, and extension temperatures. Figure 2.1 illustrates the design.

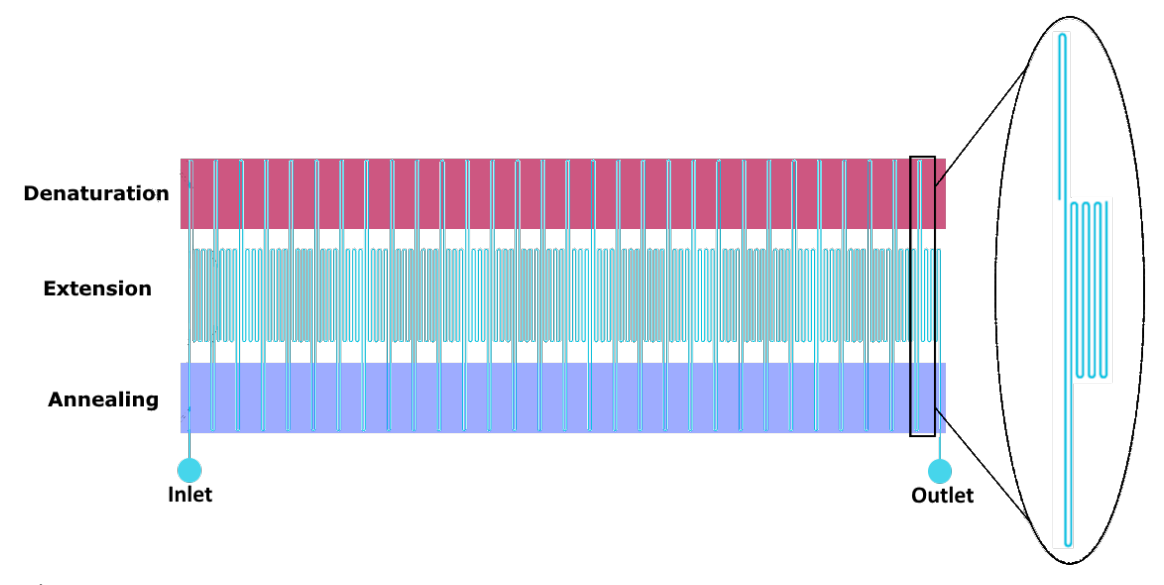


Figure 2.1: Schematic of a serpentine chip design. From the inlet, the fluid is transported from the annealing zone to the denaturation zone, before looping within the extension zone. The insert shows a complete cycle.

Two separate heaters define the denaturation and annealing zones, while the temperature gradient between these zones forms the extension zone. Uniformity in the temperature zones is a central problem for the integration of PCR on continuous-flow chips. With the above design, it is primarily the uniformity of the extension zone that is problematic. Installing a thermal mass underneath the extension zone is essential for an even distribution of heat and establishing a uniform zone. Other factors include the substrate material and heater placement. To investigate the temperature distribution on the chip, and determine the exact design specifications, a model of the system is simulated using the COMSOL Multiphysics Software V.6.3.0.335.

2.1 COMSOL Model

A model system is designed based on the specifications of past successful studies as well as the availability of materials. [21, 58–60]

NB4 2. Chip Design

The time required to for the polymerase to replicate the target can be calculated as t=L/U, where L is the length of the amplicon, and U is the activity of the polymerase. The chip will be designed for testing with a cutinase DNA template, 1077 nucleotides (nt) in length, with primers. The size of the amplicon the polymerase has to build for each strand is 1059 nt. Assuming the low end of polymerase activity, 60 nt/s, the theoretical extension time is 17.7 s.

The model is designed with channel dimensions of 90x50 μm (WxH), as was used by Kopp et~al. [21] to successfully amplify a 1kbp amplicon. The max length of a segment is 23 mm, between the furthest points within the denaturation and annealing zones, which could allow for the chip to fit onto a microscope slide commonly used in microfluidics. To ensure enough time for a full extension, the channel loops six times for a total of seven passes within the extension zone. This results in a ratio of 1: 3.5: 1 between each zone; not accounting for regions of transient temperatures. The straight segments are connected by turns designed as tori with a major and minor radius of 180 μm and 90 μm , respectively. This results in 180 μm of separation between each channel segment.

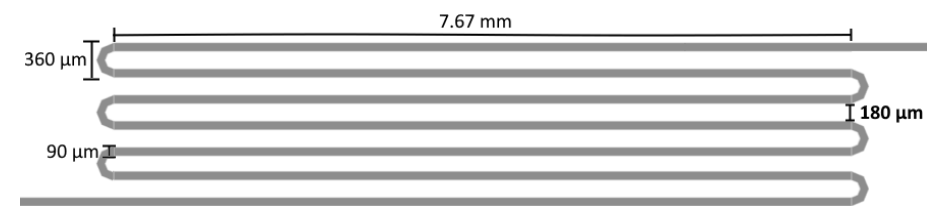


Figure 2.2: Zoomed in, top-down view of the extension loop. The channels are 90 μm wide, with 180 μm of separation between neighboring channels.

For the temperature of the extension zone to be uniform, a thermal mass 11 mm wide is placed beneath the extension zone, see figure 2.3. As seen in the insert of figure 2.1, one end of the channel continues into the denaturing zone; the other into the annealing zone. This defines one cycle. With a max length of 23 mm, and a width of $2160\mu m$ per cycle, the chip could theoretically fit 30 cycles onto a microscope slide commonly used in microfluidics. The heaters are separated from the extension thermal mass by 1mm. See figure 2.3.

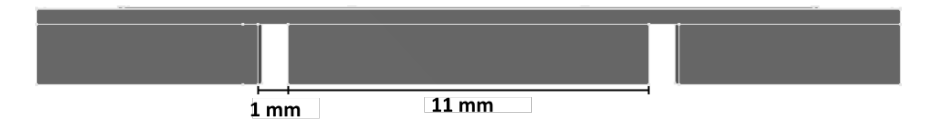


Figure 2.3: Side view of the chip, which shows the distance between heaters and the thermal mass.

To complete the model, an additional segment between annealing and denaturation is introduced before the first cycle to accommodate an inlet in the annealing zone. The last cycle ends in the annealing zone, which is then defined as an outlet. See figure 2.1. For practical concerns, the inlet and outlet were extended 1 $\rm mm$ away from the channel structure. The footprint of the channel structure then becomes 24x65.16 $\rm mm$.

2.1.1 COMSOL Physics

The chip is modeled in COMSOL using the physics modules "laminar flow" and "heat transfer in solids and fluids". The laminar flow module introduces the Navier-Stokes equation (eq. 2.1), along with the continuity equation for the conservation of mass for an incompressible fluid (eq. 2.2).

$$\rho \frac{\partial \mathbf{u}}{\partial t} + \rho (\mathbf{u} \cdot \nabla) \mathbf{u} = -\nabla p + \mu \nabla^2 \mathbf{u} + \mathbf{F}$$
 (2.1)

$$\nabla \cdot \mathbf{u} = 0 \tag{2.2}$$

 ${\bf u}$ is the velocity field, ρ is the fluid density, p is the pressure, μ is the dynamic viscosity, and ${\bf F}$ represents external forces such as gravity.

The heat transfer module introduces the equations for energy conservation (eq. 2.3) and thermal radiation to the ambient (eq.).

$$\rho C_p \left(\frac{\partial T}{\partial t} + \mathbf{u} \cdot \nabla T \right) = \nabla \cdot (k \nabla T) + Q$$
 (2.3)

$$-\mathbf{n} \cdot \mathbf{q} = \epsilon \sigma (T_{amb}^4 - T^4) \tag{2.4}$$

 C_p is specific heat capacity; T is temperature; t is time; k is thermal conductivity; Q is change in energy from a heat source or sink; \mathbf{n} is the normal vector of the surface; \mathbf{q} is heat transfer per unit area; ϵ is the surface emissivity; σ is the Stefan-Boltzmann constant; T_{amb} is the ambient temperature; and T is the surface temperature. When evaluating eq. 2.3 for solid material, the convection term $\mathbf{u} \cdot \nabla T$ reduces to 0.

Equations (2.1)–(2.3) are coupled through the velocity field. As these equations are non-linear, COMSOL uses the finite element method (FEM) to solve them numerically. FEM is a strategy to achieve approximate solutions to partial differential equations by dividing the system into smaller subdomains. For each subdomain, the governing equations are converted to their respective weak forms and approximated using polynomials for easier computation.

2.1.2 Meshing

The process of dividing the system into subdomains is referred to as "meshing". Straight channel segments are represented by a structured quadrilateral mesh mapped onto the cross-section of the channel with a maximum element size of 18 μm and swept through the segment volume. The turns are meshed with free tetrahedrals. A boundary layer node implements seven boundary layers, the first of which is 0.5 μm thick, increasing by 50% each layer. The resulting mesh of the channel structure has an average quality of 0.67 based on maximum angle - with 1 being perfect and 0 degenerate. The minimum element quality is 0.11. Figure 2.4a illustrates a cross-section of a channel with the resulting mesh.

NB4 2. Chip Design

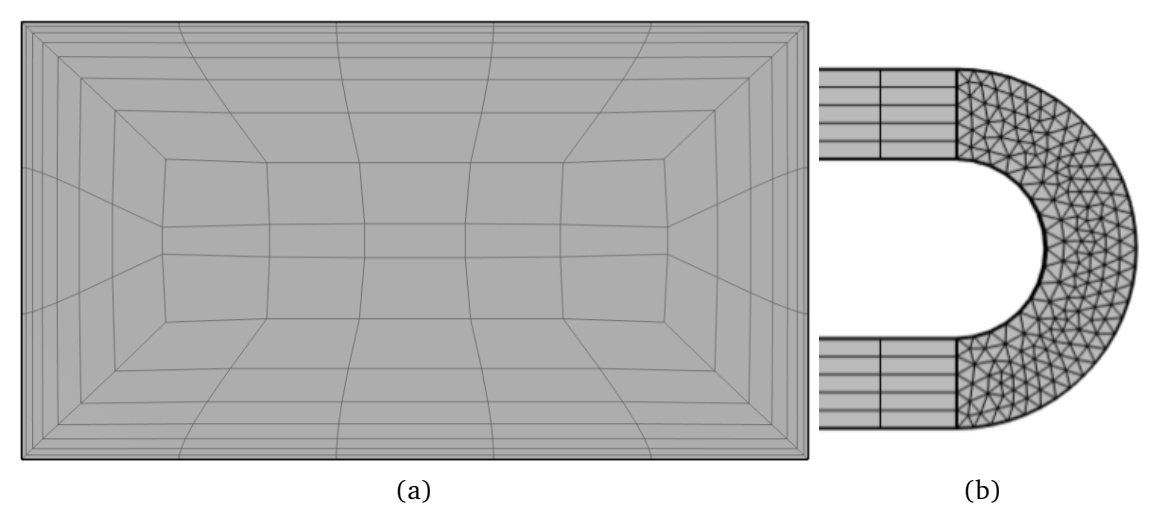


Figure 2.4: (a) Cross-section of a channel segment. The boundary layer closest to the channel walls is 3 μm thick, increasing by 50% each layer for 7 layers. (b) Mesh of a turn segment viewed from above.

The center thermal mass is meshed with a coarse-structured quadrilateral surface swept through the volume. The remaining geometry is meshed using a free tetrahedral mesh.

Methods & Materials 3

Table 3.1: Chemicals used in this project.

Chemical	CAS No.	Lot No.	Supplier
Tryptone	91079-40-2	P0199W	VWR
Yeast extract		M0186W	VWR
Sodium chloride	7647-14-5	23B214016	VWR
Agar	9002-18-0		Sigma-Aldrich
Ampicillin			In-house stock
SOC outgrowth medium		10152375	New England Biolabs
Tris base	77-86-1		Sigma-Aldrich
Glacial Acetic acid	64-19-7	15F100502	VWR
EDTA pH 8			In house
Agarose	9012-36-6	19G0256361	VWR
Ethidium Bromide	1239-45-8	SLBF7132V	Sigma-Aldrich
Ethanol	64-17-5	21E054025	VWR
GeneJET plasmid miniprep kit		00714520	Thermo Fisher Scientific.
TMC-3283 Electronic Fluid	86508-42-1	25-440	TMC Industries
Paraffin Oil	8012-95-1	STBG7873	Sigma-Aldrich
Trichloro(1H,1H,2H,2H-perfluorooctyl)silane	78560-45-9		Sigma-Aldrich
184 Silicone Elastomer KIT	63148-62-9	0006387182	SYLGARD [®]

Table 3.2: Chemicals used for PCR.

Chemical	CAS No.	Lot No.	Supplier
dNTPs mix			New England Biolabs
$MgCl_2$ (50mM)	7786-30-3	3121929	Thermo Fisher Scientific
10x PCR buffer		3113172	Thermo scientific
1 kb DNA Ladder		0071708	New England BioLabs
Gel loading dye purple 6x - no SDS	B7024S (Catalog no.)	10043909	New England BioLabs
AccuGene®Molecular biology water	7732-18-5	8MB248	Lonza

Table 3.3: Enzymes, plasmids, and cells used in this project.

Biological Material	Description	Supplier	
Taq polymerase (recombinat)	CAS. No. 9012-90-2 Lot No.: 3141943	Thermo Fisher Scientific	
NEB [®] 5-alpha F'/ ^q	lot: 10162569, DH5 α derivative	New England Biolabs	
pFCPEX1D	pET11a plasmid w. cutinase	In house	
Purified BSA 100X	Lot No. :0061011, conc.: 10 mg/mL	New England BioLabs	

Name	Sequence	T_m °C
pET11a1rev	5'-CCT CTT GCG GGA TAT CCG-3'	52.6
pET11a2for	5'-GAT GTC GGC GAT ATA GGC-3'	50.3
CutAparev	5'-AGG AAC TCA GGG GCA GG-3'	51.9
CutStyfor	5'-CCG ACA GGA CCA AGG TC-3'	51.9
CutKpnrev	5'-TGC GGC GCT AGA GGT AC-3'	51.9
CutSmafor	5'-TAT GCC CGG GGT TCA AC-3'	49.5

Table 3.4: Primers used for PCR. The supplier is TAG Copenhagen A/S.

3.1 Microfabrication

3.1.0.1 Wafer Preparation

Four-inch silicon wafers were cleaned and used for lithography and dry etching to fabricate molds of the serpentine channel structure. Adhesion, resist deposition, and soft bake were carried out on a SUSS Microtec Gamma Cluster System. In the adhesion step, wafers were dehydrated by baking at 120 °C in a vacuum chamber (\sim 0.35 bar). Hexamethyldisilazane (HMDS) was introduced into the chamber via chemical vapor deposition (CVD) for 30 s using dry nitrogen as a carrier gas. After the HMDS step, the chamber was purged with nitrogen, leaving a \sim 1.5 $\mu \rm m$ HMDS layer on the wafer surface. The wafers were then cooled before resist application.

3.1.0.2 Resist Deposition

The positive photoresist AZ MiR 701(29 cps) was applied using spin coating. To minimize wetting issues and backside contamination, the resist was dispensed dynamically at a low spin speed. 3 mL of resist was dispensed while spinning at 800 rpm for 15 s. In order to achieve a thicker film coating, the resist was subsequently allowed to dry at 600 rpm for 75 s before the spin-off. The spinoff is performed at 3000 rpm for 10 s, yielding a resist thickness of \sim 4 μ m. The wafers then underwent a soft bake at 90 °C for 90 s using proximity heating at a 1 mm gap. This is one of DTU's standard processes.

3.1.0.3 Exposure & Development

The resist was exposed using a MLA150 WMII maskless aligner. The channel mask template was prepared in advance, while the inlet and outlet circles were manually defined on the machine. The exposure used a 375 nm laser diode array, with an initial setting of -6 defocus and a dose of 800 mJ/cm². Due to defects observed on the first test mold (mold no. 1), the dose was decreased to 760 mJ/cm² for all subsequent molds.

A Post-exposure bake was carried out at 110 °C in contact mode for 60 s, and the exposed pattern was developed in 2.38% TMAH (AZ 726 MIF) using puddle development. The development rate was \sim 2 $\mu \rm m/min$.

3.1.1 Etching

The pattern was etched into the silicon substrate using the Bosch process with a STS-Pegasus DRIE system from STPS Technologies. Etching conditions were first evaluated on mold no. 1 using the DTU "Process A" recipe to determine the etch rate and possible etch depth at 20 °C.

Process A consists of two stages: An initial sequence of 11 mandatory cycles and a variable number of additional cycles (X) that determine the etch depth (see table 3.5). The total cycle counts for each mold are summarized in table3.6. Mold2 also has two rounds of etching, as this was the first wafer used with a different loading area. Mold 1 used a box of +5 mm from developed structures, while mold2-4 used a box area of +10 mm.

Table 3.5: Deposition and Etch Process Parameters. Time in seconds (s), gas flow in standard cubic centimeters per minute (sccm), RF and platen power in watts (W), and pressure in mTorr.

Name	Cyc.	c. Temp.	Deposition step				Etch step								
Ivaille	Cyc.	Temp.	Time	Pres.	C ₄ F ₈	SF ₆	O_2	Coil	Time	Pres.	C ₄ F ₈	SF ₆	O_2	Coil	Platen
Step 1	11	20	4	25	200	0	0	2000	7.0	25(1.5s) 90»150	0	350(1.5s) 550	-	2800	120»140 (1.5s) 45
Step 2	X	20	–	23	200		U	2000	7.0	25(1.5s) 150	U		3	2000	140 (1.5s) 45

Table 3.6: Number of etch cycles in the Bosch process for each mold.

	Dry Etch	
Mold no.	Cycles in 1st round of etching	Cycles in 2nd round of etching
1	11+20	11+10
2	11 + 22	11+17
3	11 + 22	
4	11+41	

Mold1 used a lower loading area, but this was increased to slow down etching and increase the area used for PDMS, so the surface matches when later bonding it to glass.

3.1.1.1 Profilometer

Before finalizing the cycle parameters, mold no. 1 was analyzed with a profilometer to measure etching depth per cycle. The instrument used was a Dektra XTA profilometer, equipped with a 45° cone-shaped stylus, featuring a 5 μm tip. A line scan length of 500 μm was used during scanning.

3.1.1.2 Antistiction Coating

The etched structure would be used as mold for polydimethylsiloxane (PDMS). To limit PDMS adhesion, the molds were coated with perfluorodecyltrichlorosilane (FDTS) using a MVD 100 by Applied Microstructures, inc. The protocol, named STAMP2 in the specific systems, is shown in figure 3.1.

	Power	250 Watts				
	Time	300 seconds				
		Name	FDTS2			
	Chemical # 1 (vapor order 1)	Line no.	2			
		Cycles	4			
		Pressure	0.500 Torr			
Repeated 4 times		Name	Water			
Repeated 4 times	Chemical # 2 (vapor order 2)		1			
	Chemical # 2 (Vapor Order 2)	Cycles	1			
		Pressure	18 Torr			
	Processing	Time	900 seconds			
	Purge	Cycles	5			

The STAMP2 process sequence

Figure 3.1: Fabrication process using the STAMP2 process from DTU.

3.1.2 PDMS & Plasma Bonding

A PDMS gel with embedded serpentine channels was produced using a 1:10 mixture of curing agent and silicone elastomer. The silicon wafer mold was secured between two PMMA sheets, fastened with screws. One part of the holder contained a 5 mm-high cavity aligned with the etched region of the mold to contain the liquid PDMS. The mixture was degassed in a vacuum oven, with repeated cycles of vacuum release to eliminate air bubbles, and then cured for 3 h at 80 °C.

After curing, the PDMS sheet was carefully peeled off and plasma-bonded to a 4" Pyrex wafer. Both surfaces were treated in a PDC-002-CE plasma cleaner at 500 mTorr for 2 min to activate the surfaces. The PDMS and glass were then brought into contact and placed in an oven at 65 °C for 10 min to complete bonding. Lastly, a 75x11x3 mm copper plate was glued with silver epoxy underneath the extension zone, to limit movable components in the final setup. The finalized products are called PCR chips.

A PiezoBrush PZ3 plasma pin, from Relyon Plasma, was also tested to bond the Pyrex and PDMS; however, the resulting seal was inadequate, and the method was not pursued further.

3.2 Experimental Setup

The experimental setup used to heat the chips was constructed from available materials to closely replicate the chip design described in section 2. An electronic control box containing the necessary heat controllers, platinum temperature sensors, and display modules was assembled for this purpose (see figure 3.2).



Figure 3.2: The electrical box is responsible for the electronics related to the heating.

The displays were connected to show the real-time temperature measured by the platinum sensors (Pt1000), while the heaters were configured to reach and maintain a set temperature. Two separate heat sources were employed: a Peltier element for the annealing region and a resistive heater for the denaturation region.

Initially, an aluminum block was used to dissipate heat from the Peltier element; however, this configuration resulted in excessive heating of the Peltier element. To improve cooling efficiency, a repurposed fan was subsequently integrated to cool the aluminum block. The resistive heater did not require active cooling.

Copper plates, sized to match the heating elements, with thermal paste ensured good thermal contact with the heaters. Various thermally conductive materials were used as an interface between the chip and the copper plates, and were evaluated for good thermal contact while maintaining sufficient heat transfer. Specifically, a 0.5 mm graphene sheet of thermal conductivity of 10 W/m·K, and silicone thermal pads with thicknesses of 1.0 mm and 1.5 mm, and thermal conductivities of 8 W/m·K and 2 W/m·K, respectively. The final version of the experimental setup is shown in figure 3.3.



Figure 3.3: The final experimental setup.

3.3 Bacterial Growth Medium

To perform PCR tests, plasmid DNA templates were isolated from bacterial cultures. Two types of Lysogeny Broth (LB) media were prepared to support the growth of *E.coli* harboring the pFCPEX1D plasmid, which carries the desired cutinase gene. The

formulation of the LB medium is shown in table 3.7. One LB medium was used as a liquid culture medium, while the other was prepared with agar to create solid growth plates.

The LB media were prepared and sterilized by autoclaving at 121 °C for 30 minutes. After autoclaving, ampicillin was added to the LB-agar medium once it had cooled to approximately 60 °C. Both the agar plates and the LB broth were subsequently stored at 4 °C. For liquid LB medium, ampicillin was not added for storage but instead added immediately before use, as the antibiotic is unstable when kept at 4 °C for extended periods.

Table 3.7: Recipe for LB-media in bluecap bottles. Agar is only added to the media solution used to make growth plates. The ampicillin was added after being autoclaved.

Chemicals	Concentration	
Tryptone	10 g/L	
Yeast extract	5 g/L	
NaCl	5 g/L	
Agar	15 g/L	
Ampicillin	100 mg/L	

3.4 Chemical Transformation of E. coli

pFCPEX1D plasmid was inserted into *E. coli* DH5 α cells. 40 μ L *E. coli* DH5 α cell solution and 5 μ L pFCPEX1D plasmid were carefully mixed in an Eppendorf tube. Another Eppendorf tube with 10 μ L *E. coli* DH5 α cells was used as a control.

These Eppendorf tubes were incubated on ice for 20 minutes and then heat shocked at 42 °C for 1 minute. After heat shock, the tubes were placed in ice again, where 0.5 mL pre-warmed SOC growth medium (at 37 °C) was added. The tubes with cells and SOC medium were shaken for 1 hour at 37 °C at 450 rpm. Afterward, the control tube was added and spread on a LB-Amp plate. The same was done for two pFCPEX1D sample plates, where 150 μ L was added to one LB-Amp-plate and 350 μ L was added on the other. All plates were then grown overnight at 37 °C and stored at 4 °C for later use.

3.5 Plasmid isolation

Two colonies from the sample plate were transferred to two tubes with 5 mL of liquid LB-medium and 10 μ L ampicillin of a stock solution of 100 mg/mL. These cell tubes were incubated at 37 °C and 240 rpm overnight. Following overnight growth, the cell tubes were centrifuged at 6000 rpm for 7 minutes at 6 °C. The liquid was discarded, leaving the cell pellet. A GeneJET plasmid Miniprep kit was used to isolate the plasmid solution in two tubes with 50 μ L Elution buffer each, see Appendix A.1.

3.6 Agarose Gel Electrophoresis

A 1% Agarose solution in Tris-Acetate EDTA (TAE) buffer was used to analyze DNA samples.

3.6.0.1 Tris-Acetate EDTA Buffer

A 250 mL 50x TAE buffer is made with the following chemicals in the table 3.8:

Table 3.8: Chemicals for 50x TAE buffer

Chemicals	Amount
Tris base (2M)	60.5 g
EDTA(0.05M)	25 mL
Glacial Acetic acid(1M)	14.27 mL

These components are added to milli-Q water and mixed. pH is adjusted to 8.2-8.4 with the complementary base if necessary, and the volume is adjusted to 250 mL with additional milli-Q water. The solution is autoclaved and stored at room temperature. This can be diluted to 1x TAE buffer with milli-Q water for the gel electrophoresis process.

3.6.0.2 Agarose solution

A 1% agarose in 1x TAE buffer for casting of the electrophoresis gel. The solution was heated in a microwave repeatedly for 30 seconds until the agarose completely melted. The gel solution was stored at 60 $^{\circ}$ C for later use.

3.6.0.3 Gel for electrophoresis

For each gel casting, approximately 35 mL of 1% agarose solution was added to a beaker with 0.5 μ L ethidium bromide (EtBr). The solution was poured into a prepared casting tray, and a plastic comb was lowered into the solution for sample wells. After solidification, the comb was removed, and the gel was transferred to a gel electrophoresis chamber filled with 1xTAE buffer to submerge the gel.

Samples were prepared by mixing 5 μ L PCR-product and 1 μ L of 6x loading dye. The samples were deposited adjacent to a 5 μ L 1kb DNA ladder. The gel electrophoresis was run for 45 min at 95V. The gel was later exposed to UV and analyzed using the GelDoc ENDUROTM GDS TOUCH II system.

3.7 PCR in Tube

A standard protocol was used to generate PCR products. The chemicals, primers, and Taq polymerase concentrations and volumes used for 50 μ L PCR are listed in table 3.9. The primers used during this project are listed in table 3.4.

Chemicals	Volume and Concentration	
Molecular biology water	$34.5~\mu L$	
Primer 1	$0.5~\mu\mathrm{L}$ (of a $100\mathrm{pmol}/\mu\mathrm{L}$ or $100\mu\mathrm{M}$)	
Primer 2	$0.5~\mu\mathrm{L}$ (of a $100\mathrm{pmol}/\mu\mathrm{L}$ or $100\mu\mathrm{M}$)	
dNTPs (200 μ M)	$2 \mu L$ (of a 20nmol/ μL solution)	
$MgCl_2$ (3 mM)	6 μ L (of a 25mM solution)	
10x PCR buffer	5 μ L	
Template	$1~\mu\mathrm{L}$	
Taq polymerase	$0.5~\mu\mathrm{L}$	
Total	50 μ L	

Table 3.9: Chemicals and enzymes are used for a standard PCR.

The DNA template is the isolated pFCPEX1D plasmid. The chemicals add up to 50 μ L, which is added to PCR tubes for the thermocycler (TurboCycler from BLUE-RAY BIOTECH). The *Taq* polymerase was added last and was kept at -20°C until use.

The general PCR program used on the thermocycler is listed in table 3.10.

Table 3.10: The PCR thermal program cycle. Steps 2-4 are repeated 30 times. The 3rd step depends on the primer set used and is $3-5^{\circ}$ C under their T_m .

Step	Time	Temperature	
1st	5 minutes	94 °C	
2nd	30 seconds	94 °C	
3rd	30 seconds	Primer dependent	
4th	1 minute	72 °C	
5th	10 minutes	72 °C	
6th	Until removed	4 °C	

3.8 PCR on Chip

During operation, the standard 50 μ L PCR mixture described in table 3.9 was introduced into the setup using a 25 μ L injection loop (see figure 3.4). Initially, sample loading was performed using a glass syringe, however, this was later replaced with pipette tips cut to fit the tubing. After loading the PCR sample, a switch on the injection loop assembly was flipped to introduce the PCR mixture into the system. The sample was pumped through polytetrafluoroethylene (PTFE) tubing into the chip, with 30 PCR cycles, by a continuous oil phase using a syringe pump at a flow rate of 1.5 μ L/min. This procedure was also evaluated using two different PCR buffer formulations as the continuous phase: a 1x PCR buffer and a 1x PCR buffer adjusted to pH 6.4. The temperature of each zone was measured using an infrared thermal camera, and the set temperature adjusted accordingly in an attempt to achieve temperatures of 92 °C, 72 °C, and 48 °C in the denaturation, extension, and annealing zones, respectively.

Fluorescein disodium salt was added to the standard PCR mixture in different concentrations to visualize the PCR mixture during flow in the chip.

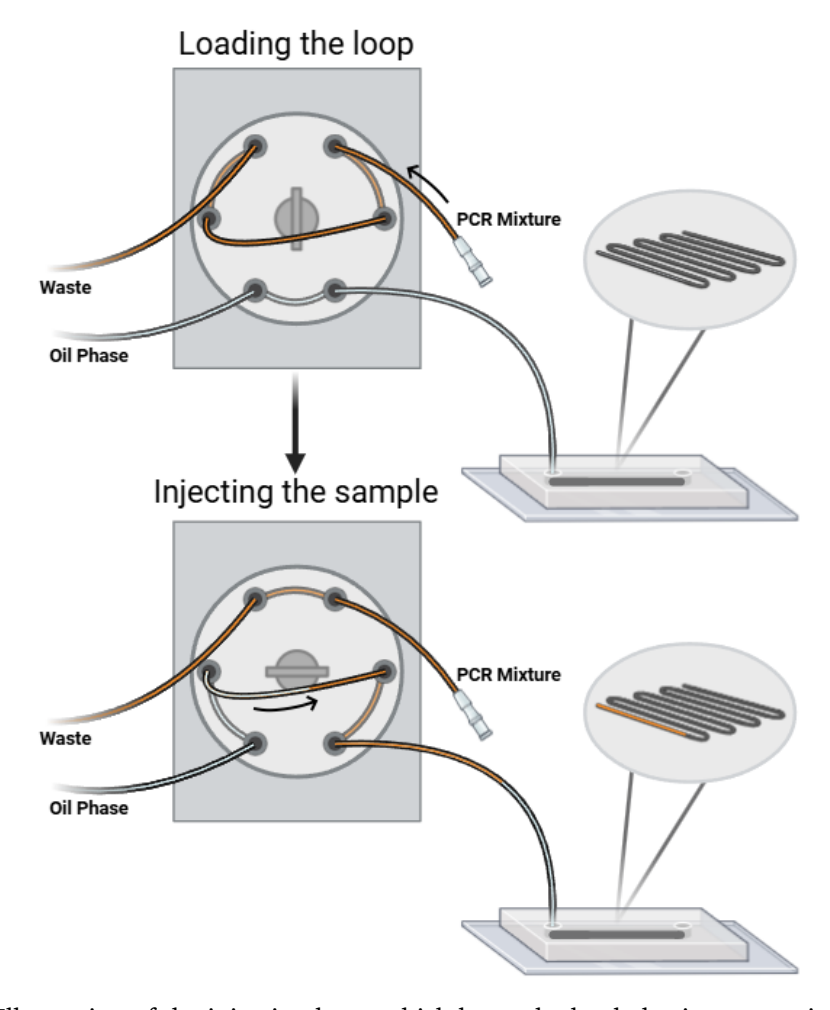


Figure 3.4: Illustration of the injection loop, which has to be loaded prior to running the sample. **LOADING**: The PCR mixture is run to fill the center tube, with any excess volume discarded through the waste outlet. The oil phase is run to fill the connection to the chip. **INJECTION**: A dial on the back of the loop switches the interior connections. The center tube, now filled with PCR mixture, is connected to the oil phase and can be run through the chip "sandwiched" between the two oil phases.

3.9 COMSOL Studies

The design of the chip is modeled and simulated in COMSOL Multiphysics. The physics interfaces included are "Heat Transfer in Solids and Fluids", "Laminar Flow", "Surface-to-Surface Radiation", "Nonisothermal Flow", and "Heat Transfer with Surface-to-Surface Radiation". The interface "Phase Field in Fluids" was used to simulate the water-oil phase boundary.

Heat Transfer in Solids and Fluids

Using the interface's default nodes, the channel domains are defined as fluid, and all remaining domains as solid. "Boundary Heat Source" nodes are introduced to define a constant temperature where the heating elements contact the chip, and a "Surface-to-Ambient Radiation" node is applied at every boundary exposed to the surroundings. Options not explicitly mentioned are left at default values.

Laminar Flow

This interface is only applied to the channel structure. All the default nodes are unchanged, notably the no-slip boundary condition at the surface of the channels. An inlet and outlet are introduced, using a fully developed flow boundary condition for both. The inlet is defined by a flow rate, and the outlet with an average relative pressure of 0. Options not explicitly mentioned are left at default values.

Surface-to-Surface Radiation

This interface is used to account for heat radiation through the gap that separate the heating elements and the center thermal mass. It is only applied to surfaces facing each other. Options not explicitly mentioned are left at default values.

Phase Field in Fluids

In the "Phase Field Model" node, the parameter controlling interface thickness is set to equal half the maximum element size in the mesh. All sidewalls are defined as wetted walls. The contact angle with PDMS and silica is defined as 107° and 58.5°, respectively.

Coupling Interfaces

"Nonisothermal Flow" and "Heat Transfer with Surface-to-Surface Radiation" are multiphysics interfaces that couple "Heat Transfer in Solids and Fluids" with "Laminar Flow" and "Surface-to-Surface Radiation", respectively. Options not explicitly mentioned are left at default values.

Materials

Table 3.11 includes all the materials used for the COMSOL simulations.

Material	Property	Value	Domain	
	Dynamic Viscosity			
Water	Heat Capacity	Built-in function	Fluid	
	Density		riuiu	
	Thermal Conductivity			
	Dynamic Viscosity	Interpolated function ¹		
Oil	Heat Capacity	$2650~\mathrm{J/(kgK)}$	Fluid	
Oli	Density	$0.910~\mathrm{kg/m^3}$	riuiu	
	Thermal Conductivity	$0.337~\mathrm{W/(mK)}$		
	Dynamic Viscosity	Interpolated function ²		
TMC-3283	Heat Capacity	$1100 \; \mathrm{J/(kgK)}$	Fluid	
1WC-5205	Density	$1820~\mathrm{kg/m^3}$	Tulu	
	Thermal Conductivity	$0.066~\mathrm{W/(mK)}$		
	Surface Emissivity	0.85		
PDMS	Heat Capacity	$1460 \mathrm{\ J/(kgK)}$	Channel Walls	
FDMS	Density	$970~\mathrm{kg/m^3}$	Chamile wans	
	Thermal Conductivity	$0.16~\mathrm{W/(mK)}$		
	Surface Emissivity	0.85		
Silica	Heat Capacity	$740 \; \mathrm{J/(kgK)}$	Substrate	
Silica	Density	$2203 \mathrm{\ kg/m^3}$		
	Thermal Conductivity	$1.38~\mathrm{W/(mK)}$		
Float Glass	Heat Capacity	$730 \mathrm{\ J/(kgK)}$		
	Density	$2440 \mathrm{\ kg/m^3}$	Separator	
	Thermal Conductivity	$0.937~\mathrm{W/(mK)}$		
Copper	Surface Emissivity	0.04		
	Heat Capacity	$385~\mathrm{J/(kgK)}$	Thermal Mass	
	Density	$8960 \mathrm{\ kg/m^3}$	THEITHAI MASS	
	Thermal Conductivity	$400~\mathrm{W/(mK)}$		

Table 3.11: List of materials used for modeling and simulating the chip design.

The oil used for the experiments was paraffin oil. The specifications of the paraffin oil state the viscosity to be between 110 and 230 $\rm mPa \cdot s$ at 20 $^{\circ} \rm C$ by the supplier (Sigma-Aldrich), but no thermal dependence was described. In order to approximate the flow using the paraffin oil, another oil called Paryol Electra was used as a stand-in in COMSOL. Paryol Electra is a sunflower oil produced by A&A Fratelli Parodi with a viscosity of 84 $\rm mPa \cdot s$ at 20 $^{\circ} \rm C$, and the thermal dependence of its viscosity has been investigated. [61]

¹ Temperature dependent viscosity was interpolated using data from [61]

² Temperature dependent viscosity was interpolated using data from [62]

Results & Discussion 4

COMSOL Multiphysics was used to simulate temperature distribution within the channel structure. The result of the simulation using the model setup described in section 2 is represented in figure 4.1, which shows how the temperature changes as water flows through the channel. The flow rate was set to 1.5 μ L/min, and the annealing and denaturation temperatures were set to 48 °C and 92 °C, respectively. Ambient temperature was defined as 20 °C.

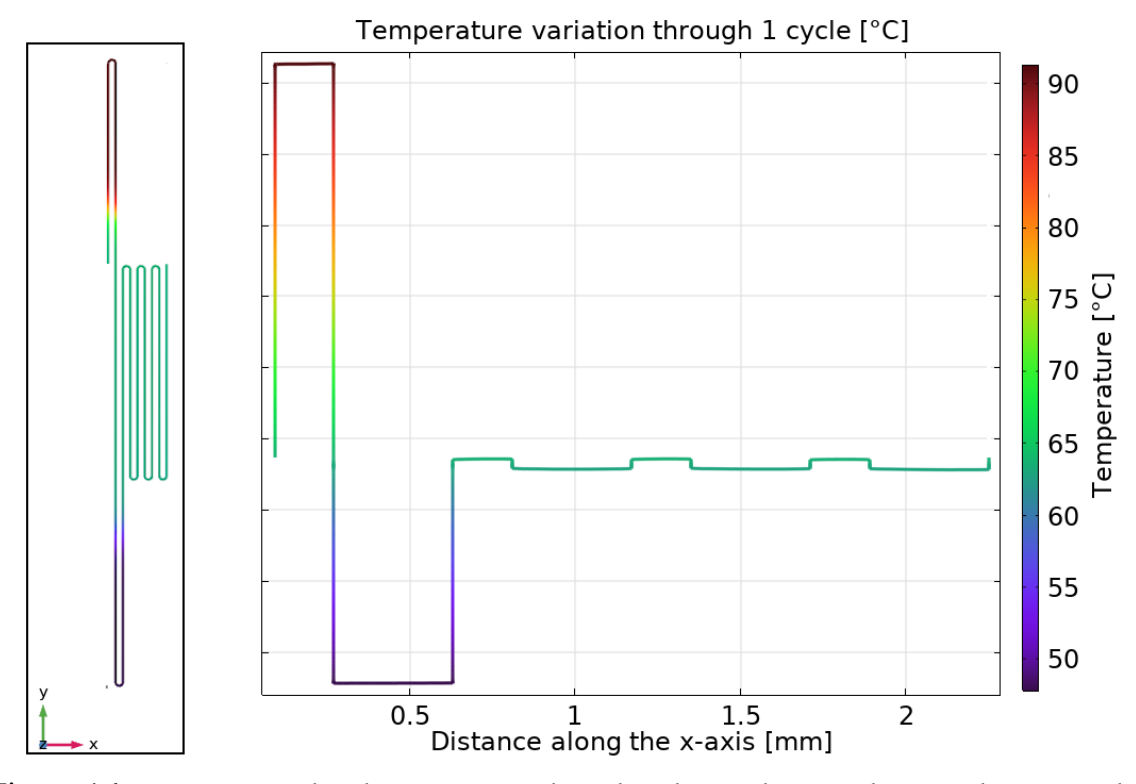


Figure 4.1: Temperature distribution in a single cycle. The gap between heating elements and the center thermal mass is 1mm of air. Flow rate is 1.5 μ L/min. Denaturation and annealing temperatures are 92°C and 48 °C, respectively. **Left**) One cycle on the chip, starting and ending in the denaturation zone, colored to represent the temperature and highlight the three temperature zones. **Right**) Temperature along the central streamline as a function of the x-coordinate, colored to indicate the corresponding channel section of the cycle. The horizontal sections correspond to the turns that connect each section of the channel, and the vertical change represents the change in temperature between subsequent turns.

From figure 4.1, the temperature in the extension zone appears to vary between 62.9 $^{\circ}\mathrm{C}$ and 63.4 $^{\circ}\mathrm{C}$. The possibility of increasing this temperature was investigated in additional simulations. At first, the gap between the denaturation heater and the thermal mass was decreased from 1 $^{\circ}\mathrm{C}$ 1. This raised the temperature to between 68.4 $^{\circ}\mathrm{C}$ 1. This raised the temperature to between 68.4 $^{\circ}\mathrm{C}$ 1.

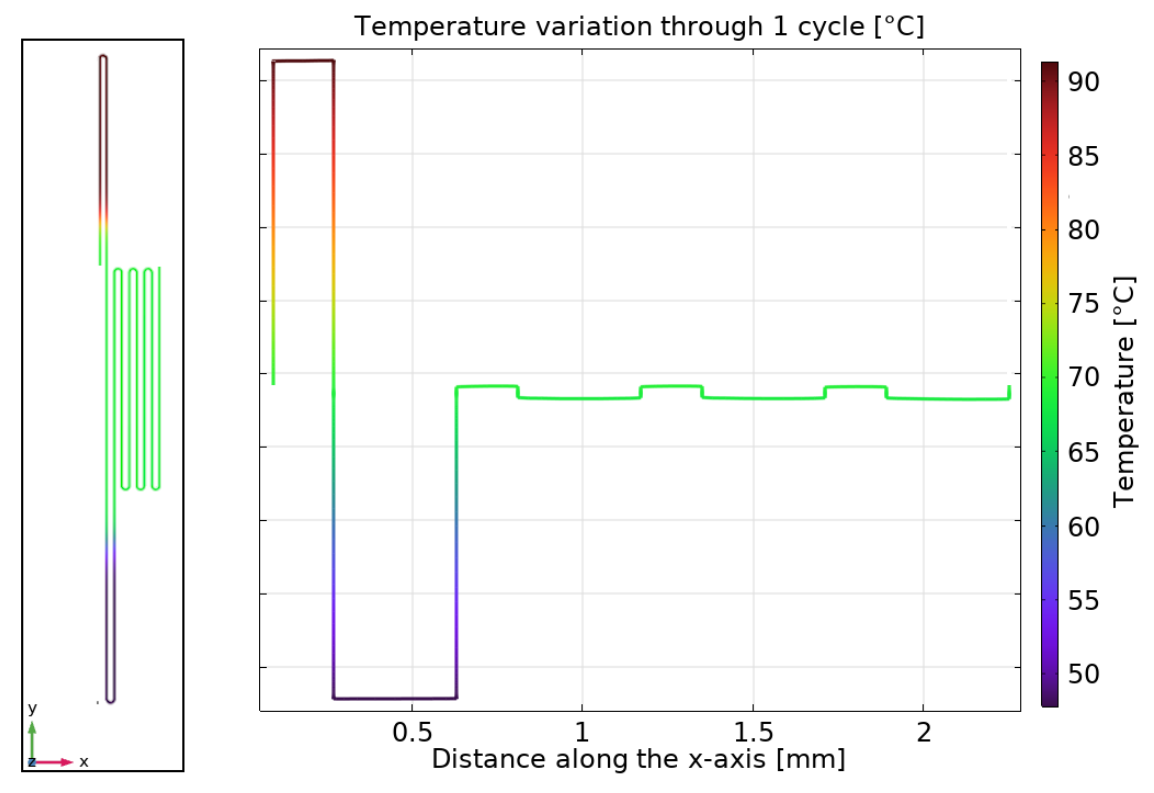


Figure 4.2: Temperature distribution in a single cycle. The gap between the denaturation heating element and the center thermal mass is 0.5mm of air. Flow rate is 1.5 μ L/min. Denaturation and annealing temperatures are 92°C and 48 °C, respectively. **Left**) One cycle on the chip, starting and ending in the denaturation zone, colored to represent the temperature and highlight the three temperature zones. **Right**) Temperature along the central streamline as a function of the x-coordinate, colored to indicate the corresponding channel section of the cycle. The horizontal sections correspond to the turns that connect each section of the channel, and the vertical change represents the change in temperature between subsequent turns.

Then, a simulation using 2 $\rm mm$ of float glass as a separator between the denaturation heater and the thermal mass was performed, see figure 4.3. The extension temperature increased to 71.992-72.486 $^{\circ}$ C.

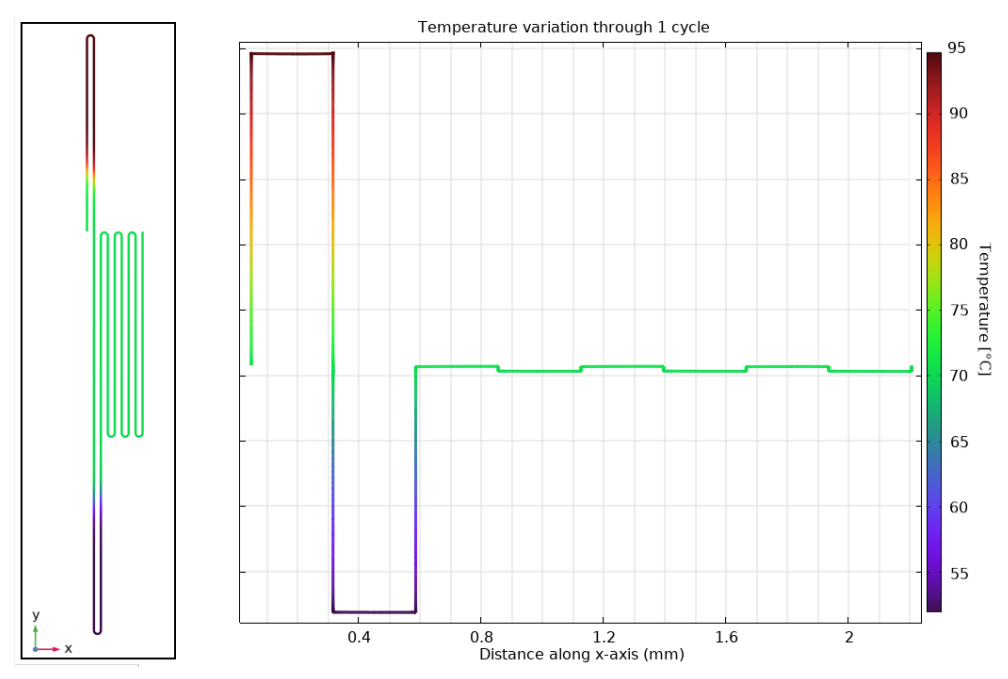


Figure 4.3: Temperature distribution in a single cycle. The gap between the denaturation heating element and the center thermal mass is 2mm of soda-lime glass. Flow rate is 1.5 μ L/min. Denaturation and annealing temperatures are 92°C and 48 °C, respectively. **Left**) One cycle on the chip, starting and ending in the denaturation zone, colored to represent the temperature and highlight the three temperature zones. **Right**) Temperature along the central streamline as a function of the x-coordinate, colored to indicate the corresponding channel section of the cycle. The horizontal sections correspond to the turns that connect each section of the channel, and the vertical change represents the change in temperature between subsequent turns.

Figure 4.4 shows a velocity profile through a turn within the extension zone, with a $1.5\mu L/min$ flow rate. The figure shows how the flow profile changes as the turn initiates, indicated by the lateral shift of the velocity peak. As the flow turns, it speeds up near the inner sidewall before returning to the original flow profile.

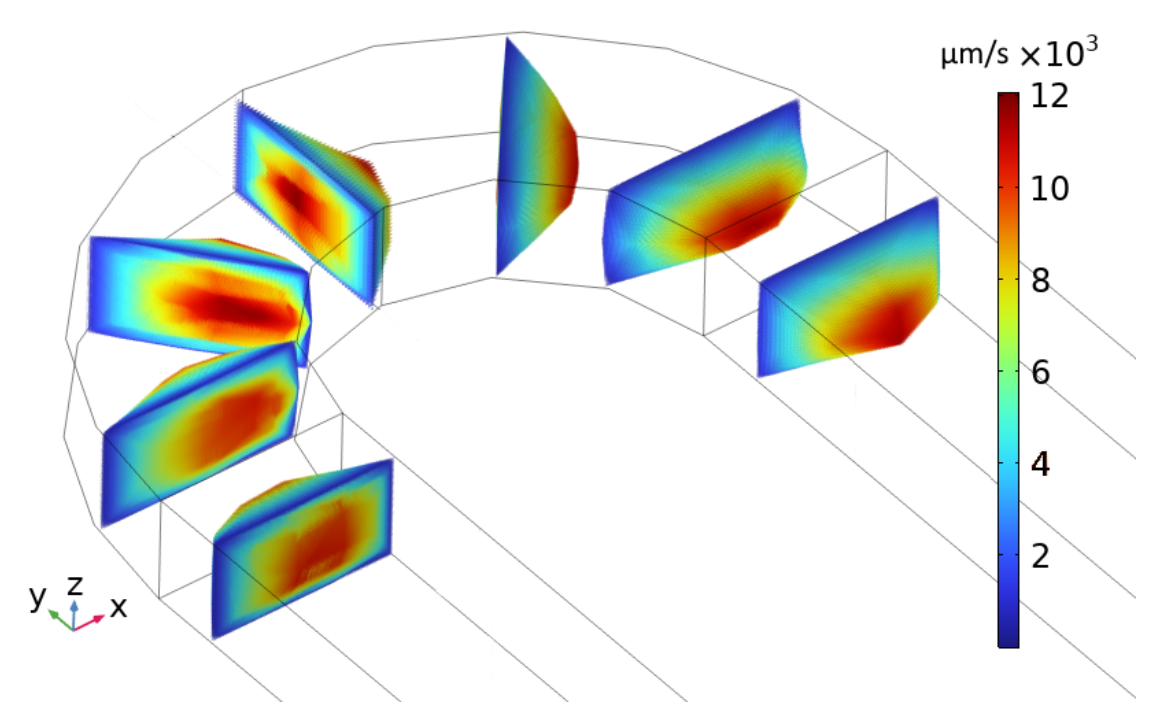


Figure 4.4: Velocity profile of water in a turn. Flow rate is set to $1.5 \mu L/min$

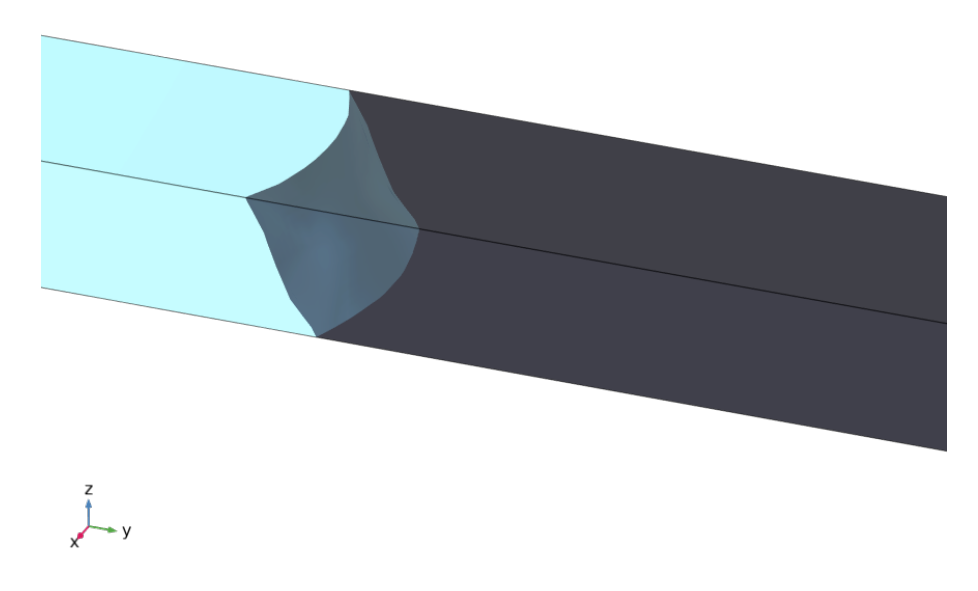


Figure 4.5: Flow profile in a 2-phase phase-field simulation. The channel is filled with oil (dark gray) as water enters through the inlet (light blue). The darker blue represents the boundary between the two immiscible phases.

In order to examine the interface between the water and oil phases, a two-phase flow simulation using the phase field method was performed in a very short segment of the channel.

The interface in figure 4.5 does not match the parabolic flow profile, likely because the laminar flow interface does not account for the contact angle with the sidewalls. The difference in contact angle between PDMS and silica may be the cause of the slanted profile.

The pressure from the inlet across a single cycle at three channel depths was plotted in order to compare the pressure drop when using oil and TMC, using a flow rate of $1.5\mu L/min$. See figure 4.6.

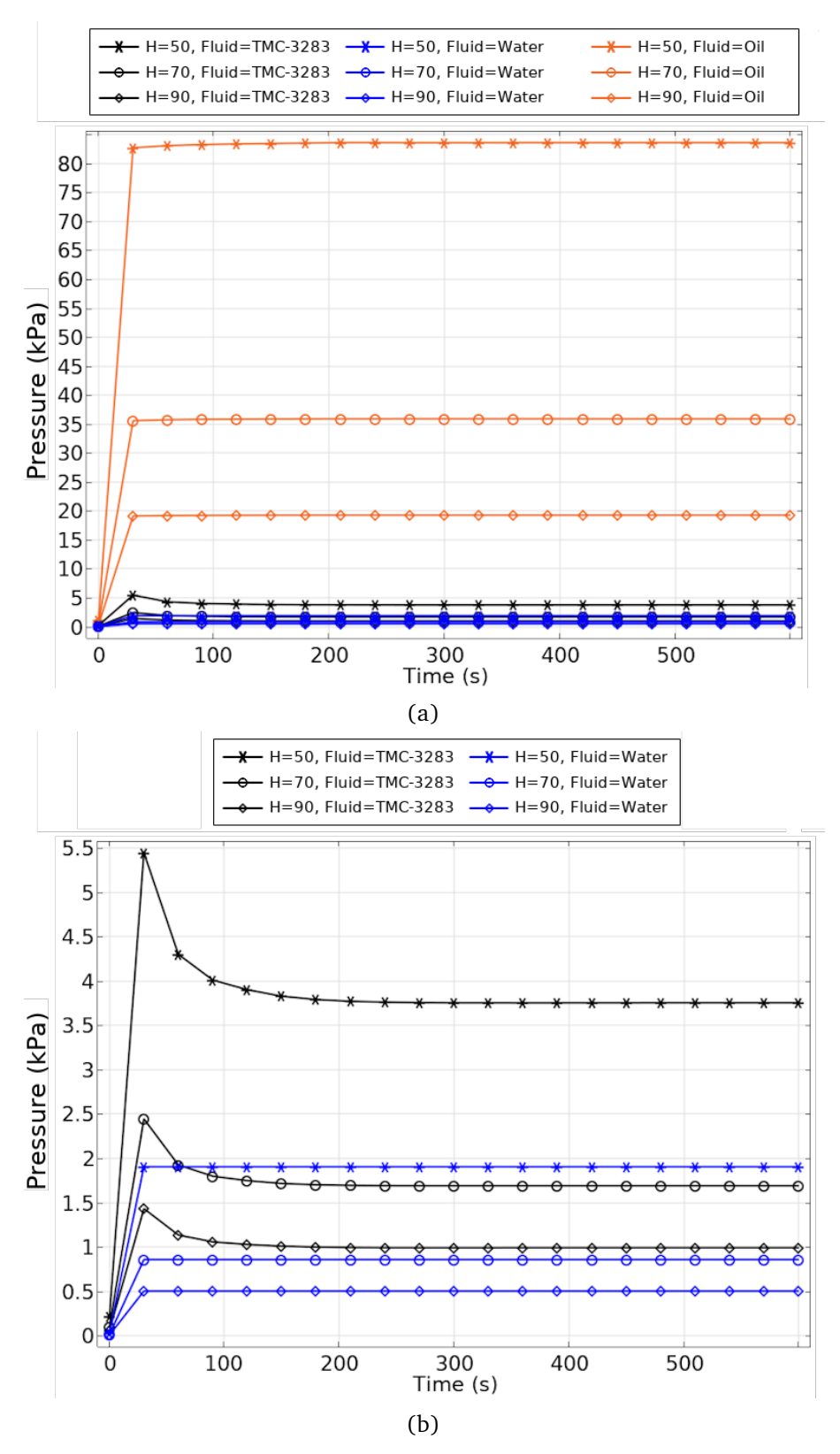


Figure 4.6: **a**) Plot of pressure measured at the inlet over time using a flow rate of $1.5\mu L/min$. The plot illustrates the difference in pressure necessary to drive the flow at the inlet depending on the solution and channel depth. The pressure was measured for simulations using water (blue), TMC-3283 (black), and oil (orange), for three different channel depths; $50\mu m$ (X), $70\mu m$ (\circ), and $90\mu m$ (\diamond . **b**) Zoomed in view of water and TMC-3283 from **a**).

Figure 4.6 highlights the high pressure at the inlet necessary to drive the flow when using oil. As the pressure drop across a channel has a linear dependence with the length of the channel, assuming symmetry and identical flow properties, the pressure drop across a chip with 30 cycles can be calculated. The inlet and outlet connects to the channel structure through additional channel segments that breaks the symmetry (see figure 2.1). To calculate the full pressure drop, the pressure is measured starting after that initial section and multiplied by the number of cycles, after which the pressure drop of the extra section is added. This yields the complete pressure drop, presented in table 4.1

Fluid	Channel Depth		
	$50~\mu\mathrm{m}$	$70~\mu\mathrm{m}$	90 $\mu\mathrm{m}$
Water	$46.379 \; \mathrm{kPa}$	$20.895 \; \mathrm{kPa}$	$12.267~\mathrm{kPa}$
TMC-3283	$91.541~\mathrm{kPa}$	$41.239~\mathrm{kPa}$	$24.195 \; \mathrm{kPa}$
Oil	$2018.982~\mathrm{kPa}$	$878.598~\mathrm{kPa}$	$464.480~\mathrm{kPa}$

Table 4.1: Calculated pressure drop across a chip with channel depths of $50\mu m$, 70 μm , and 90 μm when using water, Oil, or TMC-3283.

4.1 Mold Fabrication

Four silicon wafer molds were fabricated based on the design described in section 2. The depth of each mold depended on the number of etching cycles used during the process. Initially, each silicon wafer was designed to contain two chip molds. However, due to the increased etching "load" from the larger unmasked area, the silicon etch rate decreased. As a result, the photoresist layer was completely stripped before reaching the target depth. To resolve this issue, the design was modified to include only one chip mold per wafer.

4.1.1 Molds Fabrication & Investigation

Mold 1 was used as a test wafer to optimize the fabrication process. After development, Mold 1 showed well-defined channel structures (see figure 4.7). However, several larger channel defects were also observed (figures 4.8a and 4.8b). These defects were present throughout the entire fabrication process. Images of the same areas after etching are shown in figures 4.8c and 4.8d. Such defects could restrict or completely block fluid flow within the silica-PDMS channels fabricated later.

The most significant defect appeared outside the channel structures. This issue is illustrated in the figure 4.9.

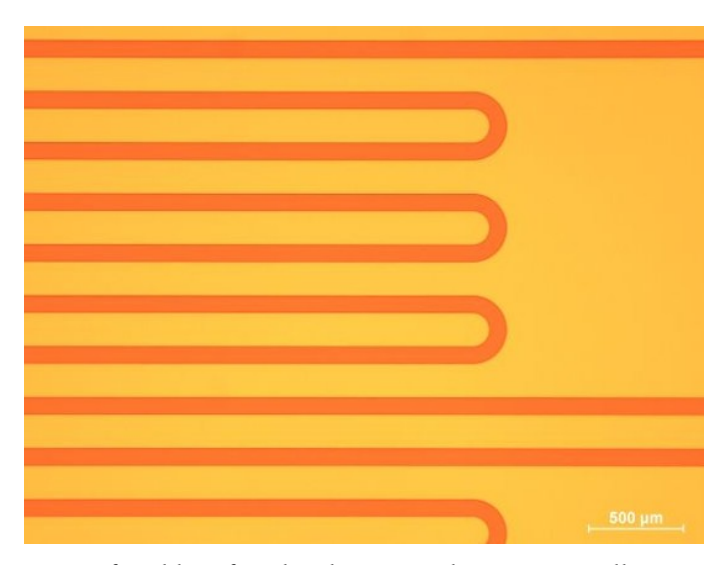


Figure 4.7: Picture of mold 1 after development, showcasing well-structured channels.

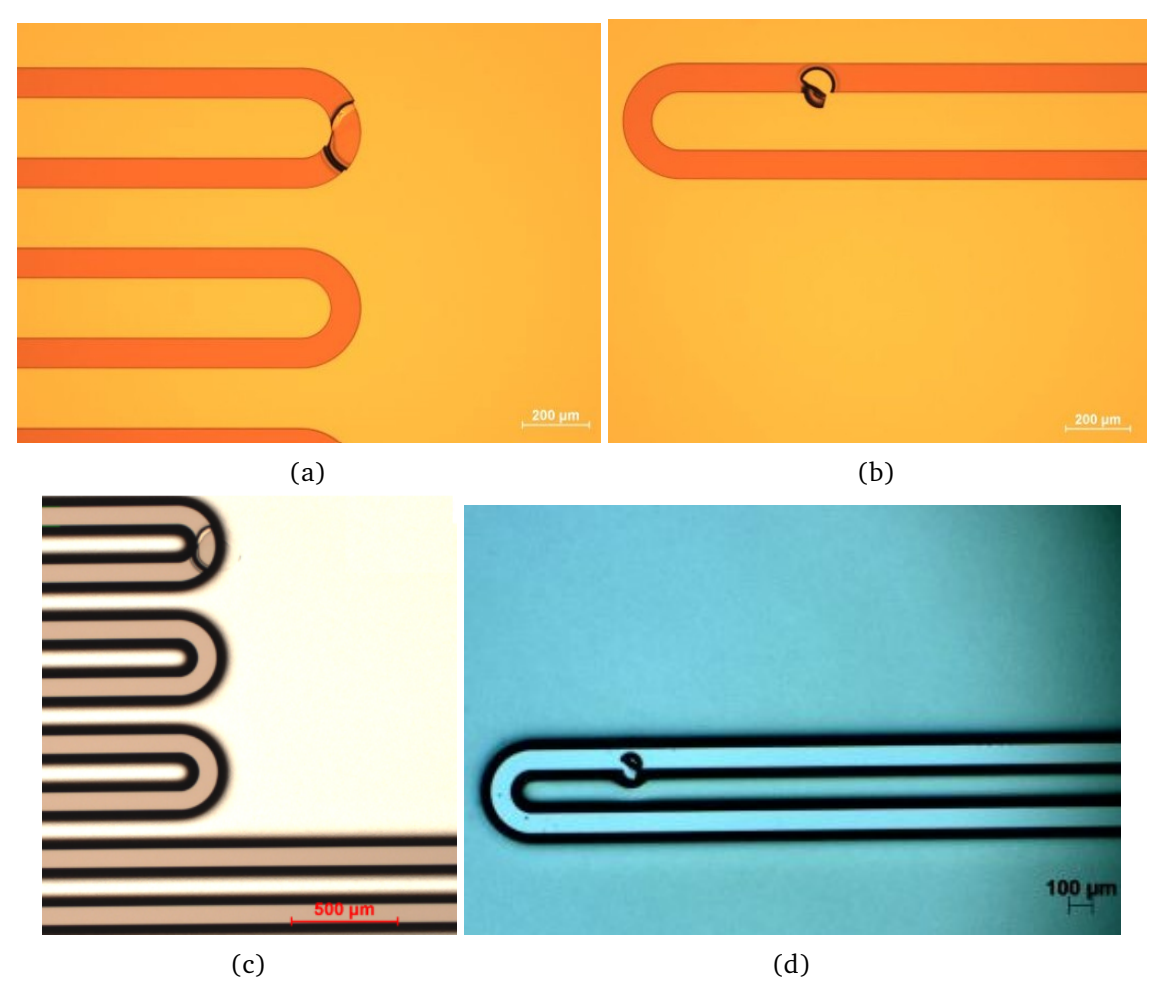


Figure 4.8: a) and b) Channel-related defects on mold 1 after development. c) and d) the same defects after etching.

To minimize this defect, the exposure dose was decreased from 800 to 760 mJ/cm^2 . This adjustment reduced the size of the defect outside the channels, although it remained visible

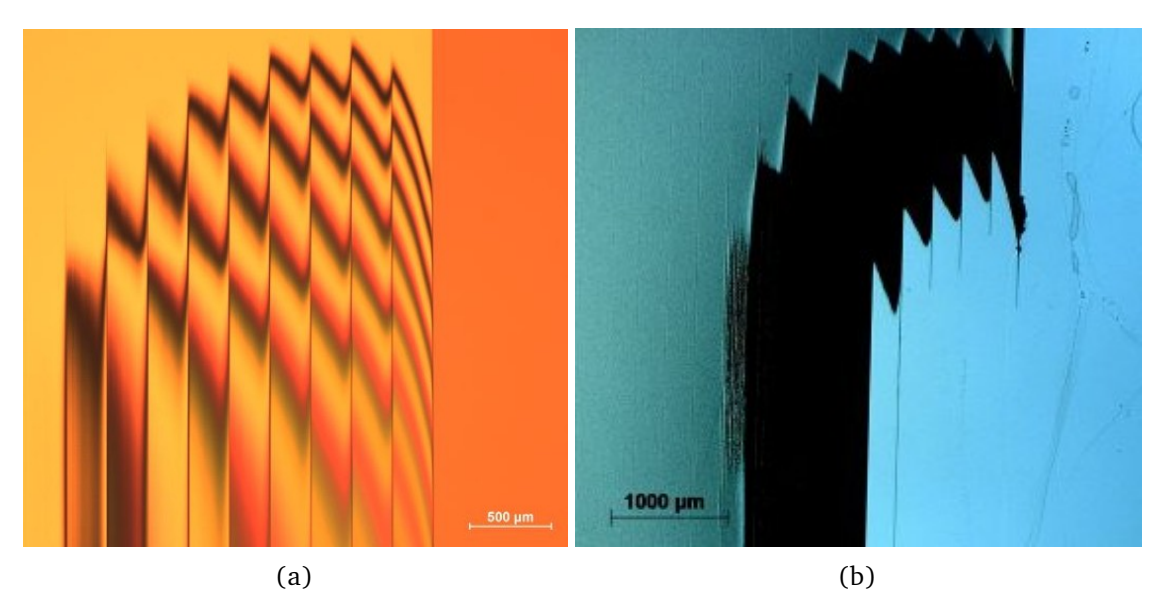


Figure 4.9: a) Mold 1 development defect, unrelated to channel structures, and b) the same defect after etching. The size of the defect is approximately 2.5 mm

on mold 2 and 4. An example from mold 2 is shown in figure 4.10a, where the defect appears approximately 1000 μ m less pronounced. Since this defect was not associated with the channel structures, and the channels themselves remained well-formed, the increased exposure dose was maintained. Only a few minor channel-related artifacts were observed on mold 2, such as illustrated in figure 4.10b.

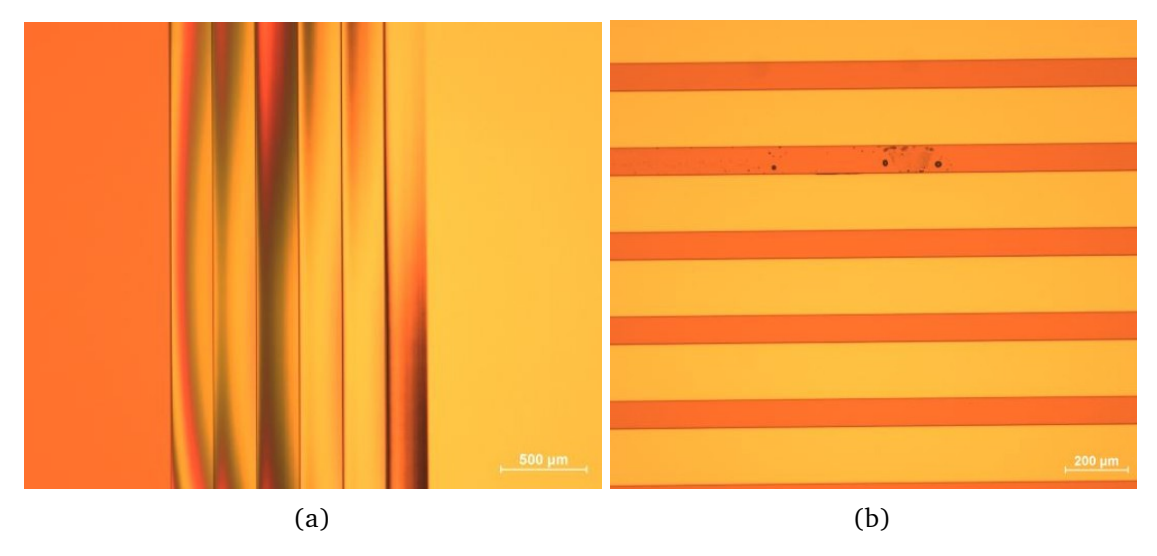


Figure 4.10: a) Mold 2 with a similar development defect to mold 1, but less pronounced, with a size of 1.5 mm. b) Example of artifacts on mold 2 after development.

Defects or artifacts related to mold 3 were nearly absent, with only a single minor artifact observed. An overview of the channels and this artifact is shown in figure 4.11.

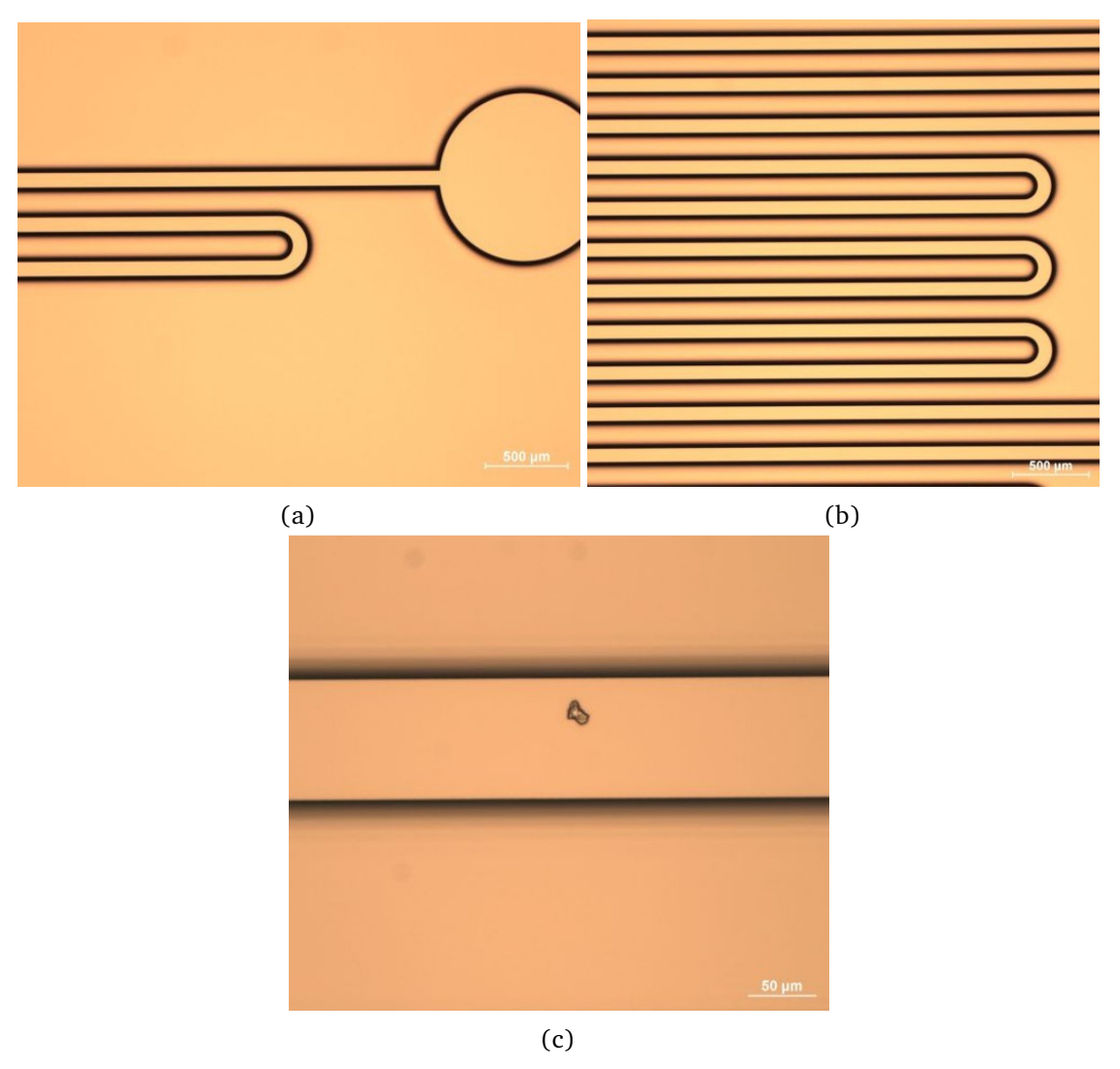


Figure 4.11: Mold 3 with well-defined channel structure of a) the inlet part, b) overview of channels, and c) the only channel-related artifact

Finally, mold 4 displayed several small channel-related defects after etching, as shown in figure 4.12. Compared to mold 1, the defects on mold 4 occurred more frequently but were less impactful on the channel structure.

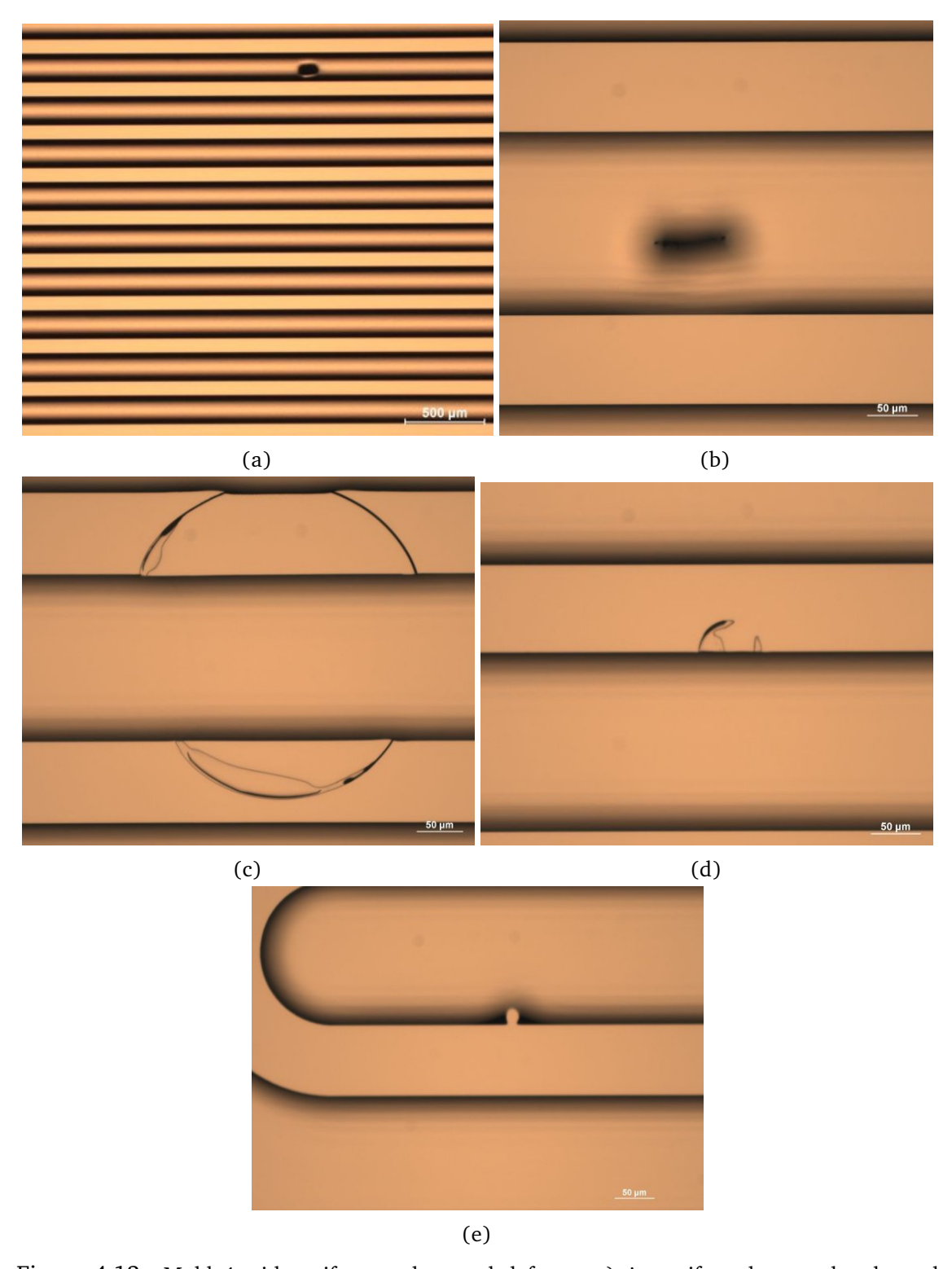


Figure 4.12: Mold 4 with artifacts and several defects. a) An artifact close to the channel structures, and b) an enhanced image of the same artifact in a). c), d), and e) bubble channel defects.

Since the fabricated molds used for PDMS sheet casting mold 2–4 were produced with the same lithography mask, exposure dose, and loading area, the only variation between them was in the vertical direction due to differences in etching depth. The channel widths

measured for molds 2–4 ranged from 89.14 to 89.75 μ m, which is very close to the target width of 90 μ m. Examples of these measurements are shown in figure 4.13.

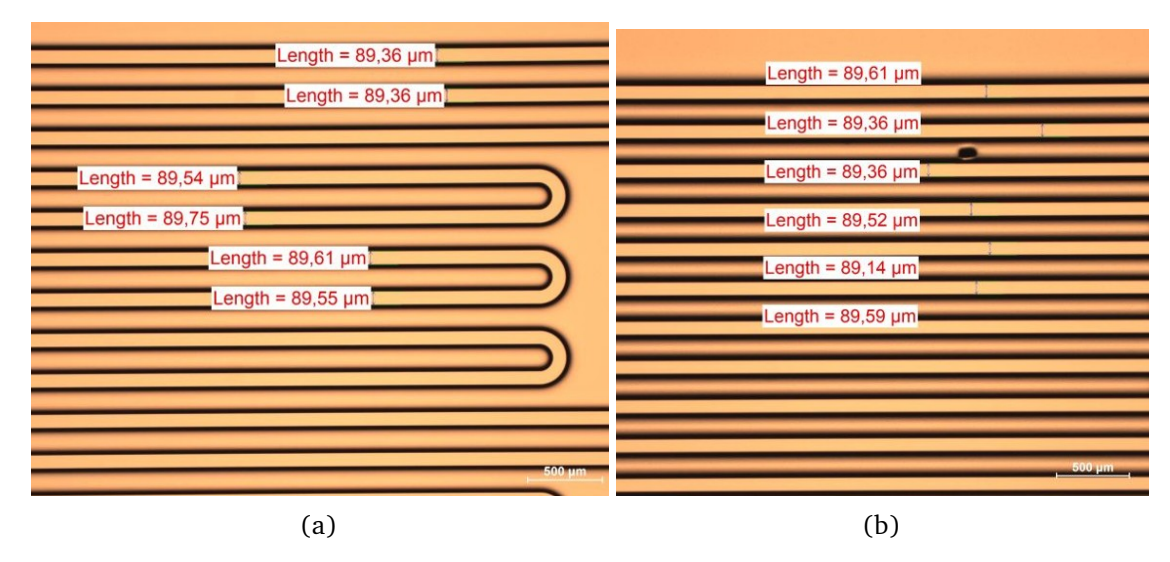


Figure 4.13: Channel width measurements after etching of a) mold 3 and b) mold 4

4.1.1.1 Profilometer measurements

The etched depth of each mold was measured using a profilometer. Mold 1 was used to test etching parameters and determine the number of etching cycles required to achieve a specific depth. Initially, 31 cycles (see table 3.6) produced a depth of approximately 56.5 μ m (figure 4.14a), followed by an additional 21 cycles, resulting in a total depth of 82.5 μ m (52 cycles in total).

Since the target etch depth was 50 μ m according to the chip design, the loading area was intentionally increased by 5 mm (10 mm from structures) for each side for molds 2–4, which reduced the etch depth per cycle. Mold 2 was used to test the new loading area. After 33 cycles, it reached an etching depth of approximately 48 μ m. Although this was close to the desired depth, mold 3, which exhibited fewer development artifacts and defects, was selected to achieve the 50 μ m depth. The etching cycles for mold 2 were continued for an additional 28 cycles to reach an estimated depth of 90 μ m for a rectangular channel, based on the measured etch rate per cycle. Mold 4 was designed with a target depth between molds 2 and 3, approximately 50% deeper than mold 3.

The etching depth differed to potentially study the inhibitory effect of PCR components based on channel size. The measured depths and corresponding cycle counts for all molds are summarized in table 4.2.

Finally, PDMS was cast on the fabricated molds. Inlets and outlets were then punched, and the PDMS layers were bonded to silica wafers using a plasma activation technique.

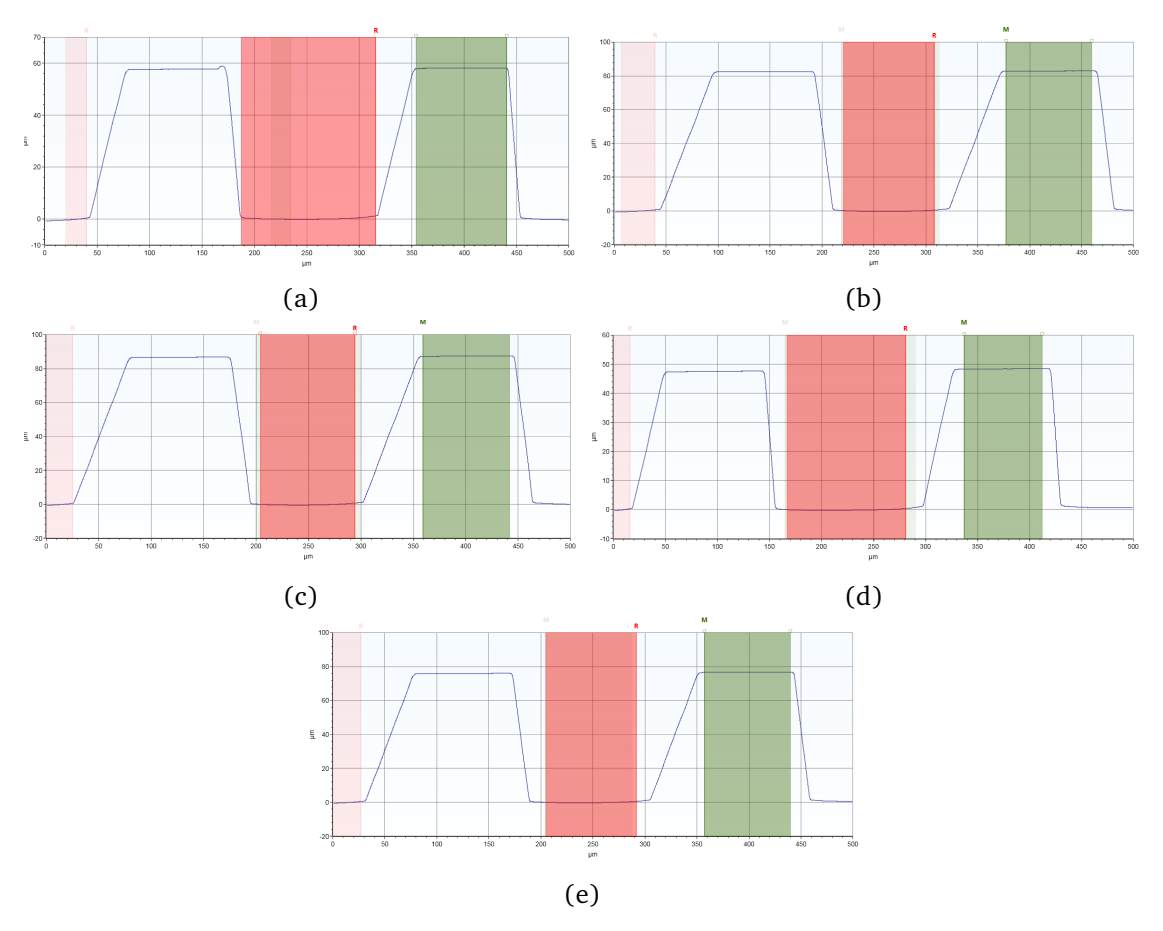


Figure 4.14: Topographic measurement across two channel segments of a) mold 1 after 1st round of etching, and b) after 2ed round of etching. c) Mold 2 after 2ed round of etching, d) mold 3, and e) mold 4 after etching. Measurements were done on a Dektak XTA Stylus Profiler at DTU Nanolab. The red and green selection zones represent the data points used to find the average height of the channels.

Table 4.2: The measured depths and corresponding cycle counts for all molds are summarized

WAFER	Measured Depth [μm]		Total Etch Cycles
	Left Structure	Right Structure	
1	82.503	82.925	52
2	86.723	87.461	61
3	47.588	48.456	33
4	75.903	76.669	52

4.1.1.2 Summary of mold fabrication

Among the molds fabricated for PDMS sheet, of molds using the same exposure dose and loading area, molds 2 and 3 were the most suitable for fabrication of PDMS sheets. They exhibited no defects within the channel structures and only a few minor artifacts, while representing the lowest and highest etch depths achieved of all wafers, respectively. These were chosen as the main molds for wafer chip fabrication.

4.2 Testing of Chips

Initially, graphene sheets were applied and tested on each heated copper plate. However, this resulted in poor thermal contact with the wafer chip. The copper plates, having been cut using a hydraulic press, were slightly twisted and curved, leading to uneven surface contact. Consequently, temperature variations of up to 16°C (80°C-96°C) were observed across the denaturation region of the chip when measured using an infrared (IR) camera on the PDMS layer. Since such temperature non-uniformity was unsuitable for the PCR components, alternative thermal interface materials were investigated.

During testing, an IR camera was used to measure the temperature directly on the substrate. For this purpose, the bare substrate of a non-functional chip was used, as PDMS is known to absorb infrared radiation. However, the temperatures measured with the Pt1000 sensors were different from those measured with the IR camera, even after repositioning the sensors closer to the channel position.

Since the sensors could not overlap the channels directly, the sensor readings were disregarded, and the target temperatures of the heat controllers were adjusted accordingly to favor the temperatures measured with the IR camera.

Since the sensors could not overlap the channels directly, the IR camera was used to measure the temperature set by the heat controllers, targeting 94 °C and 48 °C in denaturation and annealing, respectively. The sensor readings were disregarded.

When a 1.5 mm silicone thermal pad was used, the wafer chips adhered adequately to the pad despite the unevenness of the copper plates. However, due to the pad's relatively low thermal conductivity (2 W/m·K) and thickness, it responded slowly to heating and cooling changes by the heaters to uphold the temperature. This resulted in greater temperature inconsistency compared to the graphene sheets (88-98 °C, i.e, variation of 10°C).

Finally, the use of a clay-like 1 mm silicone thermal pad provided partial adhesion between both the copper plate and the wafer chip. Nevertheless, incomplete contact in parts of the denaturation region caused temperature variations of approximately 5 °C. These inconsistencies could be mitigated by adding small supplementary pieces of the clay-like silicone pad to regions identified by the IR camera as having poor thermal contact. This reduced the variation to $\pm 1~\rm ^{\circ}C.$

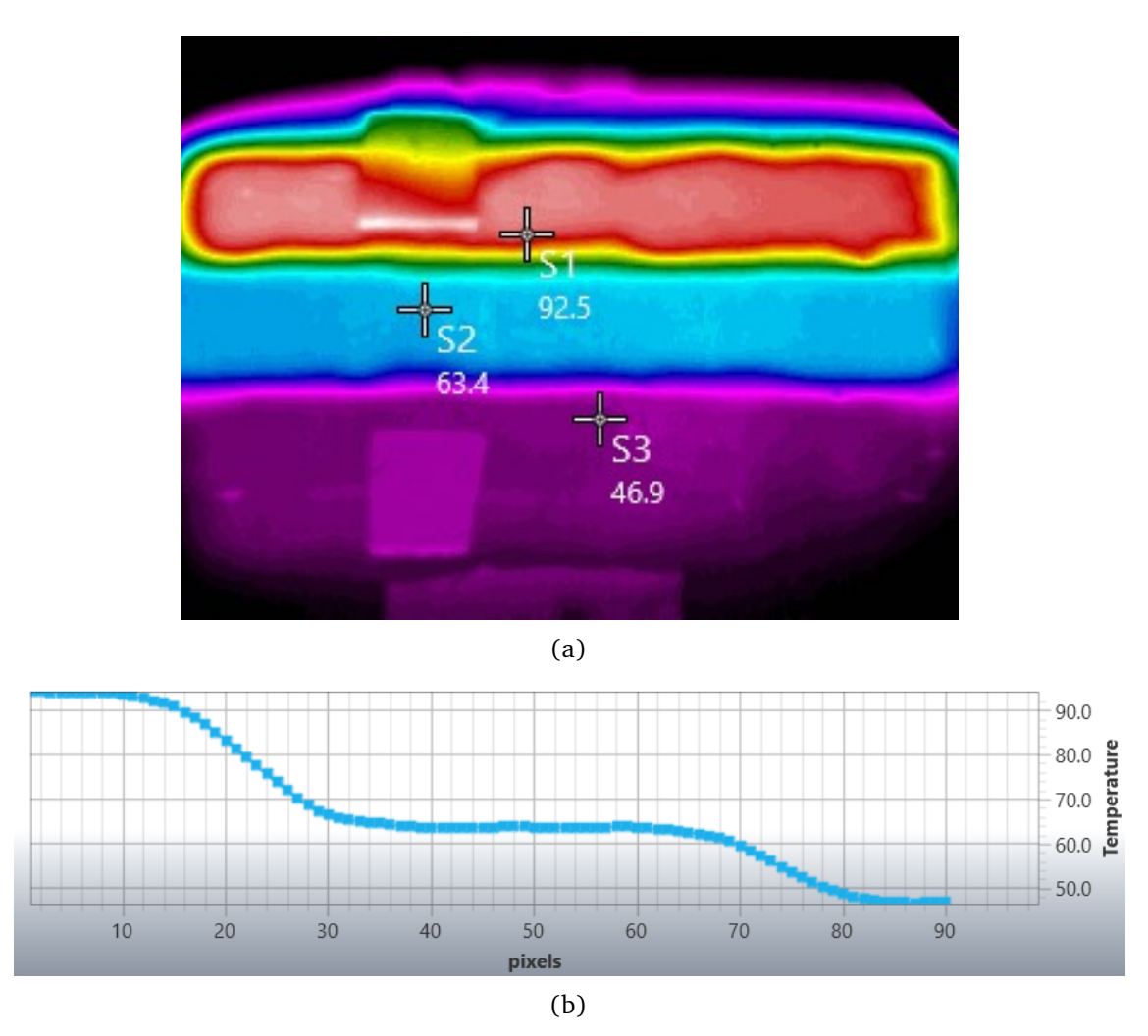


Figure 4.15: a) Image captured on the IR camera, showing the denaturation, extension, and annealing temperatures of 92.5 $^{\circ}$ C, 63.4 $^{\circ}$ C, and 46.9 $^{\circ}$ C, respectively. b) A temperature profile through all three zones.

4.3 Polymerase Chain Reaction

4.3.1 Plasmid Isolation & PCR

The pFCPEX1D plasmid DNA was isolated from DH5 α *E. coli* bacterial cells twice and initially verified by gel electrophoresis. The resulting samples are shown in figure 4.16a with a DNA product shown in lanes (2) and (3). This verified the presence of plasmid DNA was subsequently used as the template for PCR.

The primers used during this project are separated into three sets, and are listed in table 4.3 along with their utilized annealing temperature (A temp.), and size. On the wafer chips, the annealing temperature was approximated as closely as possible.

Name Sequence T_m °C Primer set A temp. (°C) size (bp) pET11a1rev 5'-CCT CTT GCG GGA TAT CCG-3' 52.6 1077 1 48 pET11a2for 5'-GAT GTC GGC GAT ATA GGC-3' 50.3 1 48 1077 5'-AGG AAC TCA GGG GCA GG-3' 2 CutAparev 51.9 48 171 CutStyfor 5'-CCG ACA GGA CCA AGG TC-3' 51.9 2 48 171 CutKpnrev 5'-TGC GGC GCT AGA GGT AC-3' 51.9 3 46.5 118 CutSmafor 5'-TAT GCC CGG GGT TCA AC-3' 49.5 3 46.5 118

Table 4.3: Primers used for PCR, sorted into the set used for the standard PCR mixture

Primer set 1 was the main primer set used for PCR in this project. Before PCR mixtures were used on the fabricated chips, they were tested on a standard thermocycler. Gel electrophoresis results (figure 4.16b) show a strong, visually intense band of close to 1 kb in lanes 2 and 3, which is sufficiently close to the expected 1077 bp, confirming that the PCR produced the correct target product. Additionally, primer set 2 and 3 were tested on the isolated pFCPEX1D plasmid, illustrated in figure 4.16c also showing sizes similar to the correct fragment sizes.

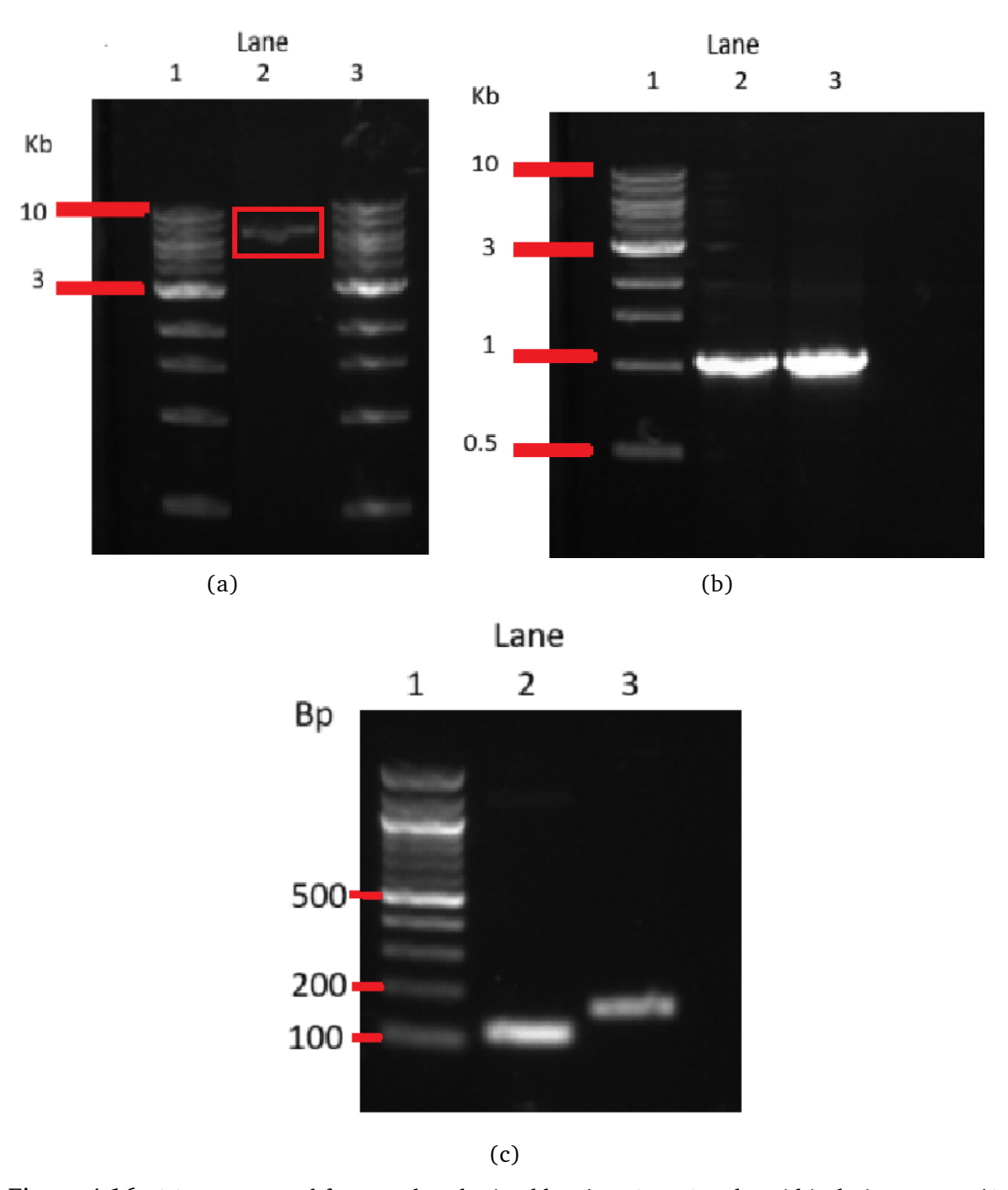


Figure 4.16: 1 % agarose gel for samples obtained by a) pFCPEX1D plasmid isolation. Lanes (1, 3) $5\mu L$ 1kb DNA ladder, lanes (2) contain $5\mu L$ supercoiled plasmid DNA. b) Lane (1) occupied by $5\mu L$ 1kb DNA ladder, and lanes (2, 3) $5\mu L$ PCR products obtained on the thermocycler using primer set 1. c) Lane (1) occupied by $5\mu L$ 100 bp DNA ladder, and lanes (2, 3) $5\mu L$ PCR products obtained on the thermocycler using primer set 2 and 3, respectively.

4.3.2 Color Assay

To visualize the water phase in the chip, dye was added to the PCR mixture. Fluorescein sodium salt was dissolved in DNase-free water at a stock concentration of 2 mg/mL and then serially diluted to assess its effect on PCR. Figure 4.17a shows dilutions from the 2 mg/mL stock to 1:300, while figure 4.17b shows repeated and further dilutions to 1:1000 in a 50 μ L PCR mixture. The illuminated spots below 500 bp observed on the agarose gel correspond to fluorescein separating from the PCR sample.

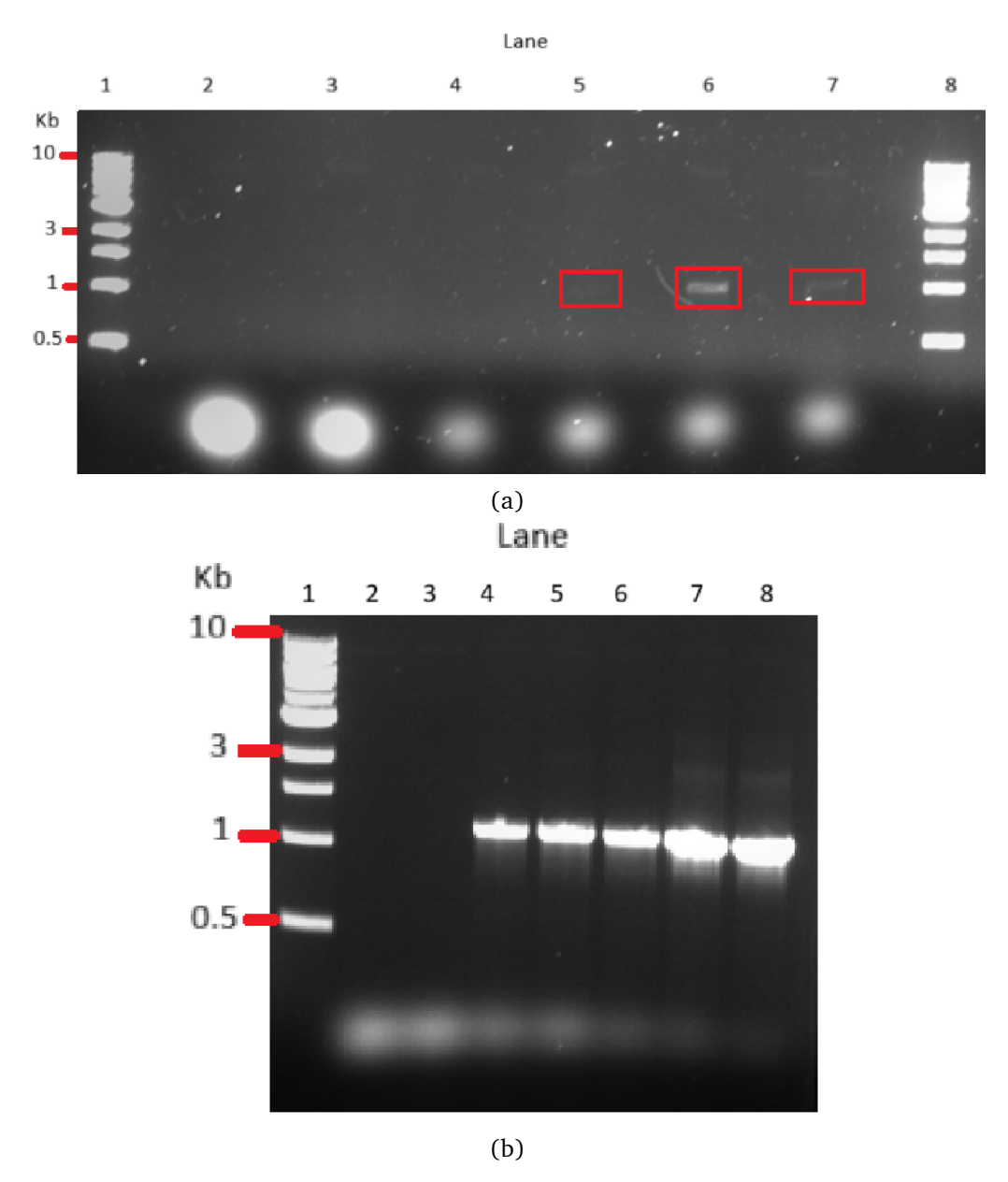


Figure 4.17: 1% agarose gel with sampled dilution assay of fluorescein in PCR mixtures (using primer set 1) using a thermocycler. a) Lanes (1, 8) contain 1kb DNA ladder and lane (2): 2 mg/ml fluorescein PCR mixture. Lanes (3, 4, 5, 6, 7) contain fluorescein dilutions of 1:50, 1:100, 1:150, 1:200, 1:250, and 1:300x, respectively. b) Repeated and continued dilution assay of PCR mixtures. Lane (1) contains 1kb DNA ladder, while lanes (2, 3, 4, 5, 6, 7, and 8) contain 1:100, 1:200, 1:250, 1:300, 1:500, 1:750, and 1:1000 dilutions of the stock 2 mg/ml fluorocine.

The assay was repeated due to a low intensity band in the initial assay, and to find the maximum usable dilution in the chip's tubing. The fluorescein assay showed that PCR was completely inhibited at dilutions up to 1:250. At higher dilutions, the PCR product was less inhibited by the dye. At 1:1000 dilution (PCR mixture with 2 $\mu g/mL$ dye), the fluorescein dye was barely visible, providing a minimal phase indicator in the tubes. In the chip, probably due to the small channel dimensions, the dye was not visually detectable after diluting from the stock concentration.

4.3.3 PCR on a Chip

A PDMS cast from mold 2 was examined in a microscope, as seen in figure 4.18. A channel was measured to be $87.57\mu\mathrm{m}$ deep and $91.06\mu\mathrm{m}$ wide, which is in agreement with the measured depth in table 4.2.

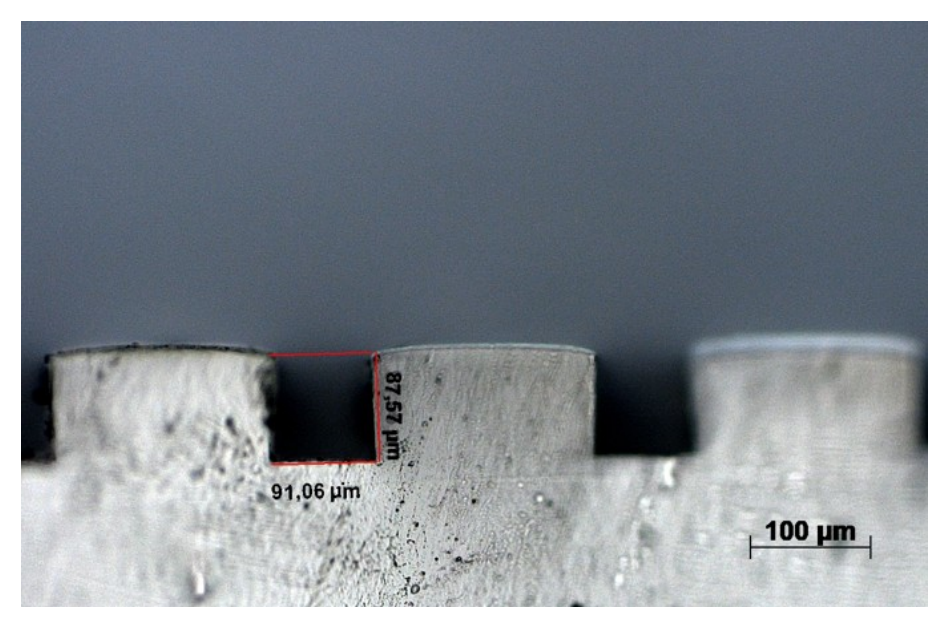


Figure 4.18: Sideview of PDMS microchannel structure visualized in a microscope. A channel is measured to be $87.57\mu m$ deep and $91.06\mu m$ wide.

After the PDMS sheets were bonded to Pyrex or fused silica glass wafers using plasma treatment, the chips were ready for flow testing. Each chip was designated based on the mold from which its PDMS sheet originated. For example, a PDMS sheet fabricated from mold 2 is referred to as a wafer 2 chip.

Figure 4.19 shows the flow inside the channel, visualized with fluorescein disodium salt.



Figure 4.19: Visualization of the channel flow using fluorescein disodium salt as a dye.

4.3.3.1 Initial Issues

Initial testing of the wafer chips using paraffin oil as the continuous phase revealed significant challenges. Because paraffin oil is several times more viscous than water, the increased flow resistance within the already small channel dimensions caused PDMS delamination. This issue occurred both at room temperature and under PCR heating conditions, where reduced viscosity was expected to improve flow.

Delamination most frequently occurred near the wafer chip inlet, often extending into the adjacent channels (see figure 4.20). Even when using wafer 2 chips, which had the largest channel dimensions, the problem persisted at flow rates between 1.5 and 5 μ L/min.



Figure 4.20: Delamination of the area around the inlet of a wafer 2 chip, when injecting with paraffin oil, at a flow rate of 5 μ L/min.

4.3.3.2 One-phase PCR on a chip

Due to PDMS delamination, a 1x PCR buffer diluted in DNase-free water was used as the continuous phase to push the PCR mixture into the injection loop through the wafer 3 chip. This approach provided lower viscosity, reducing flow resistance, but eliminated the phase barrier between the PCR mixture and the surrounding medium.

While the PCR mixture successfully passed through the channels, the fluorescein dye used in the mixture rapidly diffused and diluted, causing the visible position of the PCR sample to disappear within the tubing. As a result, the collected output volume increased by approximately 2–4 times compared to the injected amount. This issue could be addressed by using DNA purification columns (e.g., QIAquick spin columns) to concentrate and recover DNA from the diluted samples. Under standard DNA binding conditions, in this case pH \leq 7.5 and high concentrations of chaotropic salts, 50 μ L of elution buffer provides the DNA bound to the column filter.

To test this, a 1x PCR buffer was prepared and adjusted to pH 6.4 using glacial acetic acid and 1M NaOH, although polymerase. A second 1x PCR buffer was also prepared by simple dilution with DNase-free water, and the collected sample pH was adjusted to pH 7 by adding a few μ L of a 1:5 ratio glacial acetic acid solution.

The results of these experiments on a wafer 3 chip are shown in figure 4.21, which also includes an investigation of the sample injection method. Lane 3 contains a standard PCR product that was incubated for 30 seconds in the glass syringe used to transfer the sample into the injection loop. Samples collected using the 1x PCR buffer as the continuous phase are shown in lanes (4, 5), where lane (4) is the filtered sample and lane (5) is the supernatant that went through the filter. Similarly, samples collected using the pH 6.4-adjusted PCR buffer as the continuous phase are shown in lanes (6, 7), corresponding to the filtered sample and supernatant, respectively.

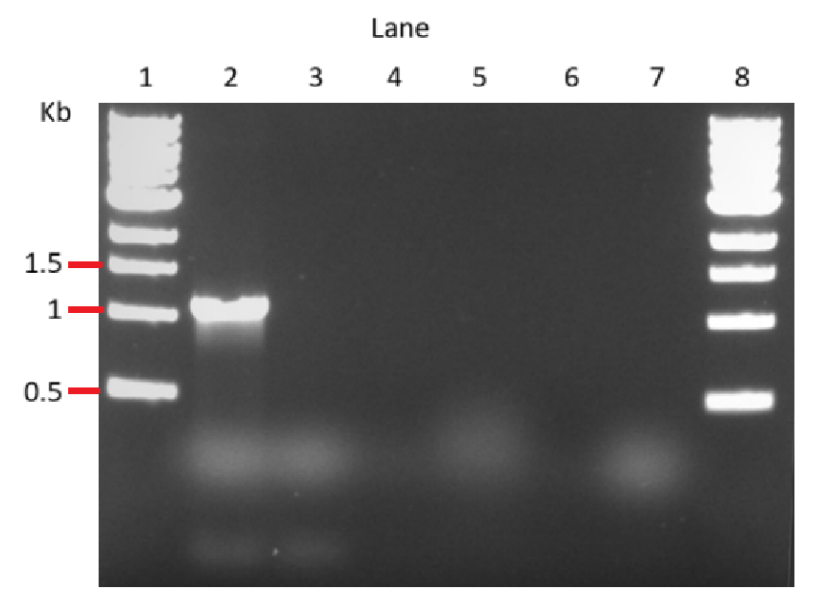


Figure 4.21: 1% agarose gel investigating injection technique, and continuous buffers pushing PCR mixtures using primer set 1. Lanes (1) and (8) contain 5 μ L 1 kb DNA ladder, lane (2) is 5μ L normal PCR product run on the thermocycler, Lane (3) 5μ L PCR mixture retained in the injection glass syringe for 30 seconds before running the sample in the thermocycler. Lane (4) contained 5 μ L filtered product, lane (5) contained 10 μ L filter supernatant flowthrough using 1x PCR buffer. Lanes (6) and (7) contain the same as 4 and 5, respectively, but using the pH 6.4 PCR buffer as the continuous media. The flow rate utilized is 2.5 μ L/min

Since no PCR product was visible in lanes (3) to (7), this result is attributed to inhibition caused by the glass syringe used for sample injection. The syringe's highly hydrophobic surface likely interfered with the reaction components, acting as a major inhibitor. Although this experiment could have been repeated after modifying the injection loop method, the additional steps involving filtration and 1x buffer dilution made the procedure time-consuming and impractical.

4.3.3.3 Two-phase PCR on a chip

After the injection method was changed to a standard pipette, a less viscous oil was introduced as the continuous phase. TMC (Trimethylcyclosiloxane) is a synthetic oil with

a dynamic viscosity of approximately 1.71 mPa·s at 20 $^{\circ}$ C, compared to 1.00 mPa·s for water and 32 mPa·s for paraffin oil at the same temperature.

Before conducting tests using TMC oil as the continuous medium, a wafer 4 chip was silanized with 1% trichloro(1H,1H,2H,2H-perfluorooctyl)silane in TMC oil to improve surface properties and flow behavior. Various flow rates and dye concentrations were tested to evaluate polymerase activity and potential inhibition effects. The results of these tests are shown in figure 4.22.

As shown in figure 4.22, no PCR product was obtained from the chip. At a flow rate of $1.5~\mu\mathrm{L/min}$, the sample should have remained within the extension region of the chip long enough for the polymerase to extend the DNA-primer duplex. Dye concentrations of 1:300 and 1:500 were selected because PCR products obtained with a 1:250 dilution were inconsistent. The dye was included solely to visualize phase separation between the oil and aqueous phases. Although the thermocycler dye dilution assay indicated that PCR amplification should occur at dilutions of 1:250 and above, this behavior may not necessarily translate directly to on-chip conditions. The loss of product can be caused by improper heating, the dye's behavior in small channels, and the inhibition of PCR components by the chip.

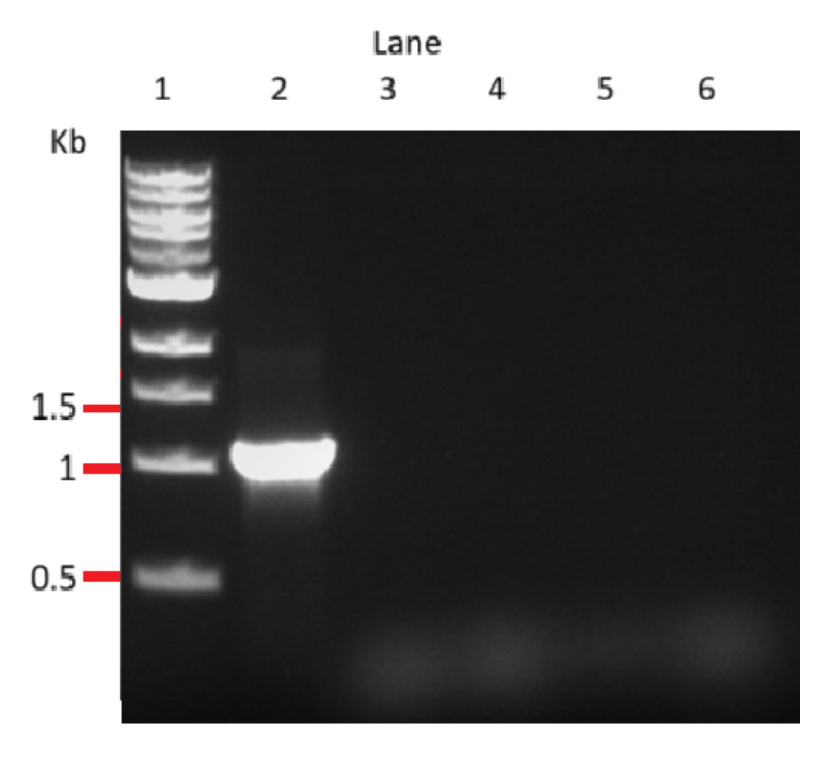


Figure 4.22: 1% agarose gel with samples using TMC oil as the continuous media. All samples used primer set 1. Lane (1) 5 μ L 1kb DNA ladder, Lane (2): 5μ L PCR product using the thermocycler. Lane (3) and lane (4) contains 5 μ L sample with dye dilution concentration of 300x of flow rate 4 μ L/min and 1.5 μ L/min, respectively. Lane (5) and (6) are 5 μ L samples with dye dilution concentration of 500x of flow rate 4 μ L/min and 1.5 μ L/min, respectively.

4.3.3.4 Trouble shooting

A new wafer 4 chip was used for further testing, this time without prior exposure to dye. The PCR mixture contained no dye and included 1 mg/mL BSA to address potential inhibition effects within the chip and to eliminate any dye-related interference. The resulting samples from this experiment were analyzed by gel electrophoresis, as shown in figure 4.23.

Although the presence of dye may have contributed to inhibition in previous experiments, testing under dye-free conditions still exhibited inhibitory effects, likely caused by polymerase or DNA adsorption within the chip. To address this inhibition, a wash was performed on a dye-free wafer 3 chip using a 10 mg/mL BSA solution at a flow rate of 1.5 μ L/min, followed by a 0.6 mg/mL BSA PCR solution, with a small volume of TMC oil separating the two solutions. The resulting PCR sample is shown in lane (2) of figure 4.24. An amplification product was observed, although its size did not correspond to the expected 1077 bp target. Instead, the observed band was between 6–8 kb, indicating nonspecific amplification. While the band size corresponds to that of the supercoiled plasmid DNA used as the template, the DNA concentration was estimated to be only 25–35 ng based on comparison with the ladder (see figure 4.16a). This amount is too low to be detected on an agarose gel stained with ethidium bromide when used as the template in a standard 50 μ L PCR reaction. Thus, it is likely a nonspecific amplification product.

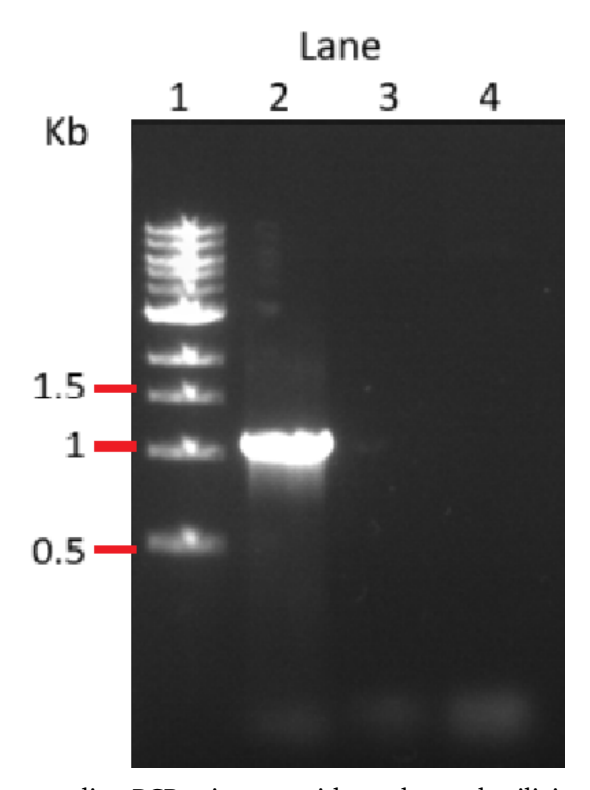


Figure 4.23: 1% agarose sampling PCR mixtures without dye and utilizing BSA and using primer set 1. Lane (1) contains 5μ L 1 kb DNA ladder, lane (2) 5μ L PCR product obtained on the thermocycler. Lanes (3) and (4) are 5 μ L samples from the wafer4 chip without and with 1 mg/ml BSA, respectively. A flow rate of 1.5 μ L/min was used.

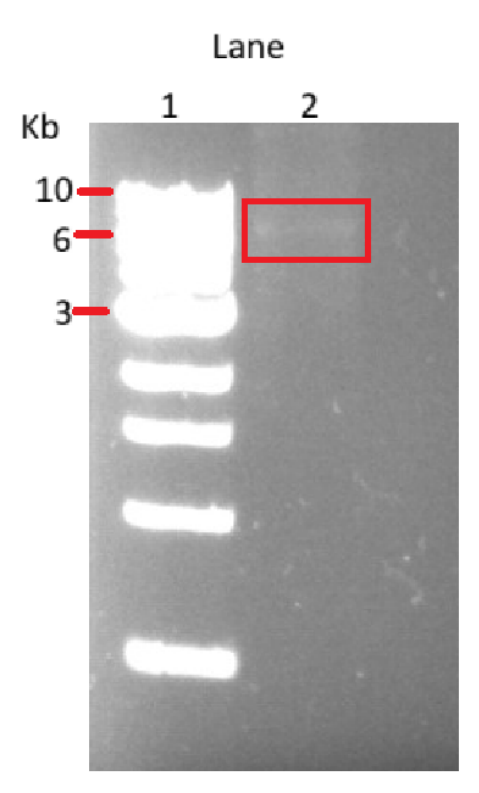


Figure 4.24: Chip wash with 10 mg/ml BSA followed by PCR sample. Lane (1) 5 μ L 1kb DNA ladder, and lane (2) 5 μ L of 0.6 mg/ml BSA PCR sample collected from the chip after chip wash.

To identify the source of inhibition and determine whether improper heating contributed, an experiment was conducted using the wafer 3 chip. Two 15 μ L PCR samples were collected from the chip and reheated on the thermocycler under the correct temperature profile, each supplemented with either 0.5 μ L of template DNA or Taq polymerase. An additional 5 μ L PCR sample from the same chip served as a control. The results are shown in figure 4.25a. The control sample in lane (2) showed no amplification products, consistent with the previous observation in figure 4.23. A faint band appeared in lane (3). This can be caused by primer dimers, nonspecific amplification, or degraded DNA, while lane (4) displayed a large quantity of nonspecific amplification products. To further assess whether the correct target was amplified, the samples from lanes (3) and (4) were used as templates in a subsequent re-amplification PCR. The results of this secondary reaction are shown in figure 4.25b. Both figure 4.25a and figure 4.25b indicate nonspecific amplification, suggesting an improper annealing temperature, and Taq polymerase was the major inhibitory component, as a majority of the amplified products appeared after this addition.

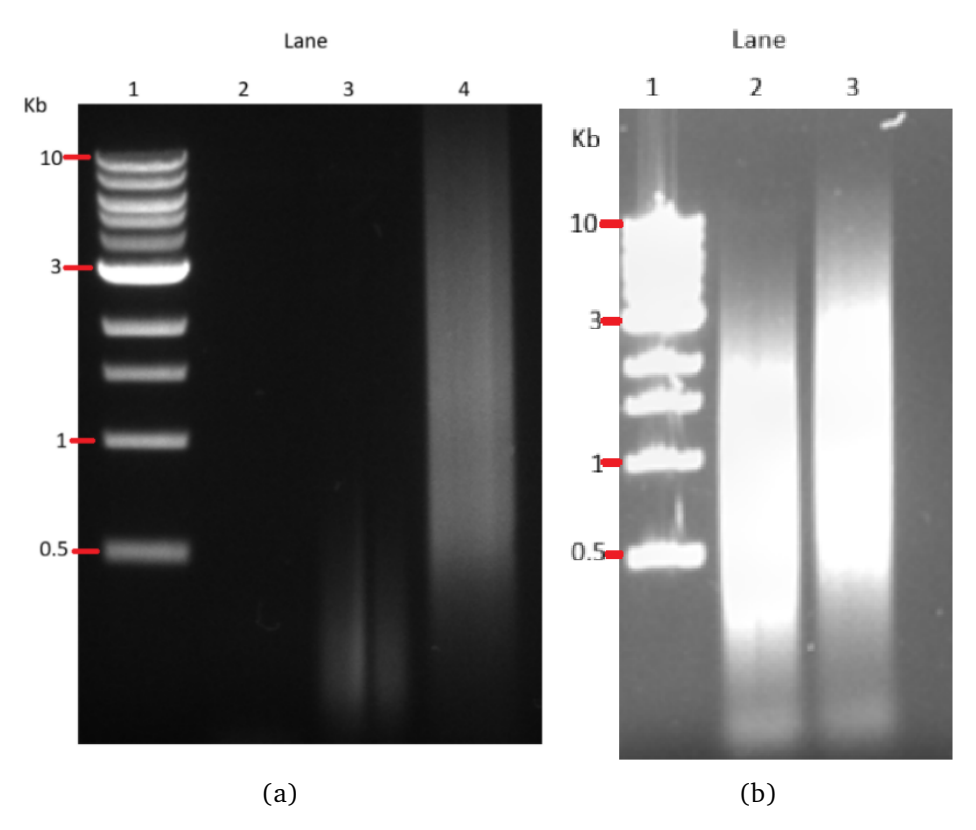


Figure 4.25: a)1% agarose gel to determine the inhibitory components of the PCR mixture. Lane (1) contains 5μ L 1 kb DNA ladder, and lane (2) contains a control sample that is not reheated with the thermocycler. Lanes (3) and (4) contain 5μ L reheated samples in the thermocycler with added template DNA and polymerase, respectively. b) 1% agarose gel to investigate the presence of a correct PCR. Reheated samples illustrated in figure 4.25a lane (3) and (4) were used as DNA templates for lanes (2) and (3), respectively. Lane (1) contains 5μ L 1 kb DNA ladder, and lane (2) contains 5μ L reheated DNA as the DNA template. Lane (3) contains 5μ L reheated polymerase sample as the DNA template.

5.1 The Design and Fabrication of the Chip

The simulations of the design indicate that it is possible to achieve a stable extension zone by taking advantage of heat exchange between the denaturation and annealing zones, as seen in figure 4.3. The original design had a gap between both heaters and the center thermal mass, but due to loss of heat to ambient surroundings, it was necessary to increase the rate of heat transfer between the denaturation and extension zone. This was accomplished in the simulations by replacing the 1 mm gap with 2 mm thick soda-lime glass, raising the temperature to $72^{\circ}\text{C}\pm0.274$. However, during the experiments, the extension temperature was too low regardless. The 2 mm soda-lime glass was replaced with 1.5 mm thermal pad material (2 W/K·m), which helped raise the extension temperature. The temperature of the extension zone was consistent, but it varied significantly between experiments. Figure 4.15a shows the extension zone with a temperature of 63.4 °C, despite the same settings in the heat controllers producing temperatures of much closer to the optimal 72 °C other times. This is thought to be due to variance in the ambient temperature, as well as small variations in heater and chip placements.

The current design does not fit onto a microscope slide, which would have been preferable for testing compared to using an entire silica or Pyrex wafer. The main reason is the extended channel segment that leads to the inlets and outlets, which made the channel structure slightly too wide for the standard 25mm width of a slide. This extension was necessary to avoid puncturing the channel when punching the holes. However, it would have been possible to create a bend, such that the chip would have been made longer rather than wider.

A standard PCR protocol includes an initial denaturation, typically lasting five minutes. This is to ensure that the template DNA is fully denatured and accessible to the primers and polymerase. This, however, is not integrated into the chip design. Lee [63] and Li et al. [64] integrated an initial denaturation by initially looping the channel within the denaturation zone. If integrated into a comprehensive platform, a reaction chamber for mixing the reagents could also serve as a heating chamber for this initial denaturation.

While running the chip, bubbles and small air pockets were frequently observed in the last \sim 4 cycles. The initial concern was that the temperature in the channels were too high and causing water to boil. However, it occurred even when filling the device with TMC-3283, which has a boiling point at 128 °C. Bubbles should also be a consistent issue through the entire channel if the liquid was indeed boiling.

NB4 5. Discussion

It may be explained by the permeability of PDMS and inconsistent flow dynamics. As the fluid undergoes repeated heating, dissolved gases are progressively expelled as described by Henry's Law. PDMS is highly permeable to gases like oxygen, carbon dioxide, and nitrogen, from which gas may redissolve into the liquid phase and cause a net gain of gases within the channel. A paper by Gao *et al.* [65] investigated the mechanism of bubble formation in PDMS when used for microfluidic channels. They concluded that bubble formation was driven primarily by water vapor and came up with a solution by running their device in a high-pressure, liquid seal. Of importance to this project; they observed that the same liquid seal effectively eliminated bubbles within the channels themselves, on top of preventing the evaporation of water through the PDMS.

Defects in the chip may also function as bubble nucleation sites. Several defects were detected during the fabrication of the molds, as seen in figures 4.8, 4.10, 4.11, and 4.12. These defects may be transferred to the PDMS, and subsequently affect the flow.

5.2 Chip Delamination

One of the main issues during the project was PDMS delamination due to the addition of oils. While it was a major issue when using Paraffin oil, TMC would also cause delamination if the heaters were not above 40 °C annealing, and 89°C.

In a paper by Bhattacharya *et al.* [66], they measured the bond strength of PDMS to glass with different parameters during plasma bonding. They achieved a bond strength of 74 psi (510 kPa) when using a chamber pressure of 1000 mTorr. With a chamber pressure of 500 mTorr as was used during bonding in this paper, [42] achieved a bond strength of 68 psi (469 kPa). Comparing this bond strength to the pressure drop calculated in table 4.1, it is clear why the chips delaminated when using paraffin oil to drive the flow. The pressure drop using oil was calculated as 2018.982kPa, and the simulations were performed using the Paryol Electra oil, which is still less viscous than the paraffin oil used for the experiments. Therefore, using paraffin oil would not have been possible even with 90 μ m deep channels. In practice, the chips produced did not have exactly 50, 70 or 90 μ m deep channels (see figure 4.2. The shallowest mold had a depth of 47.588-48.456 μ m, and any defects from the mold or deformation of the PDMS sidewalls could further increase the pressure.

The pressure when using TMC-3283 is substantially lower compared to the Payrole Electra oil (and paraffin oil, by extension), but it is an expensive specialty oil that poses some environmental concerns, as a fully fluorinated liquid with a Global Warming Potential of >5000.[62] It may be preferable to alter the design to allow for more conventional oils to be used. The most obvious change to reduce the pressure drop when using thicker oils, is to increase the channel dimensions. Figure 4.6 and table 4.1 show how changing the channel depth from $50\mu m$ to $70\mu m$ effectively reduced the pressure by $\sim 55\%$. With larger channels, the surface-to-volume ratio would naturally decrease and lower the rate of heat transfer, but larger continues-flow chips have nonetheless been successfully used for PCR. Cao *et al.* [67] were able to successfully amplify a 62 bp and a 150 bp fragment using a continuous-flow chip with channels 100 μm deep and 200-400 μm wide.

Another plasma sealing method was tried during the project, using a plasma pen; however, this was inefficient and tedious, only targeting small areas, and overheating every five minutes. Although the activated surface groups in principle would persist for 30-60 minutes, proper sealing could not be achieved with this method on a relatively large surface area needed for the entire PDMS sheet.

A completely sealed microfluidic system could also be employed to mitigate delamination issues. A study by Kang et~al.~ [68] demonstrated the use of 3D-printed dissolvable molds fabricated from common mold materials and organic solvents such as acetone and methanol in PDMS, successfully producing cylindrical 3D geometries with diameters of approximately 200 μ m. Similarly, Goh and Hashimoto [69] presented a dual dissolvable mold approach utilizing two filaments; high-impact polystyrene (HIPS) and polyvinyl alcohol (PVA), each insoluble in the other's solvent. In principle, dual dissolvable molds can facilitate the fabrication of delicate microfluidic channel structures supported by a secondary material. After the initial PDMS curing step, the secondary support material can be removed. A subsequent PDMS curing step would then seal any open areas within the structure. Finally, dissolving the primary microfluidic mold would yield fully embedded microchannels within the PDMS, eliminating the need for post-fabrication bonding or sealing to additional substrates.

However, the resolution of current 3D-printing techniques limits their application for features smaller than 100 μm , making this approach not yet feasible for the present design. As an alternative, liquid molding could be utilized. By adapting the current design and employing a negative resist, the microfluidic structures could be oriented downward within the silicon mold. A liquid molding material could then be cast, cured, and used as a dissolvable mold within PDMS. Once hardened, this mold could be dissolved away to form microchannels of desired dimensions.

The patented material FlexDymTM, designed for microfluidics, presents another option particularly well suited for design and testing purposes. FlexDymTM can be molded using a simple heat-press and with a structural mold, and can bond to itself at room temperature. Lachaux *et al.* [70] achieved a bond strength able to withstand internal pressure of 600 mbar after 1 hour in contact with another FlexDymTM sheet, and up to 2 bar when bonded at 85 °C. McMillan *et al.* [71] achieved similar results.

5.2.1 PCR & UV

The main issues observed during PCR on the chips were primarily nonspecific amplification and inhibition of *Taq* polymerase. This was evident upon reheating the samples in the thermocycler, as shown in figures 4.25 and 4.24. The apparent smears in figure 4.25 may be many small bands that result from nonspecific primer annealing that occurred in the chip, and were then successfully amplified with a thermocycler during testing for reagent inhibition. Although inhibition of the template may also have occurred, *Taq* polymerase inhibition appears to have been the predominant factor. Three common causes of nonspecific amplification in PCR microchips include insufficient initial denaturation of the DNA template, incomplete extension, and nonspecific primer annealing.

NB4 5. Discussion

Compared to the standard PCR protocol, a longer initial denaturation is used to fully separate the template strands. Subjecting the template to only a short denaturation, as in the chip design, can lead to incomplete separation. This can cause incorrect primer annealing, or prevent the primers from annealing entirely. With non-specific annealing, it is probable that the forward and reverse primers may not anneal in matching positions, whereby the resulting strands cannot anneal to each other. This would result in an abundance of ssDNA in the solution, which would be amplified each cycle.

An incomplete extension during PCR may also contribute to the large size variance observed in figure 4.25. With the flow rate of 1.5 μ L/min, and the suboptimal extension temperature measured in figure 4.15a, Taq polymerase activity was estimated to be approximately 50% of its activity at the optimal 72 °C. This would consequently lead to inconsistent and incomplete amplification products. A lower flow rate would be required if the extension temperature is consistently as low as measured in figure 4.15a. However, this is not the step resulting in the majority of nonspecific amplifications, but would have exacerbated the problems already present with the chip. To more easily reach the optimal extension temperature for Taq polymerase, a different primer set of with higher CG-content that anneals at a higher temperature could have been used, which would have increased the gradient that forms the extension zone.

Nonspecific amplification in continuous-flow PCR chips can also arise when the annealing temperature is too low or when there are prolonged transition times between thermal zones. As the transition between the extension and annealing zones occurs within a few seconds, it is more likely to be a problem related to the annealing temperature. Infrared camera measurements in figure 4.15 showed that the annealing zone ranged from 52 to 46 °C, approximately 3-5 °C below the primer's melting temperature (T_m). It is assumed that the temperature within the channels differ from that measured on a substrate without PDMS. Therefore, a more accurate method for determining the in-channel temperature is required.

Assuming the change in temperature from the PCR mixture to TMC is minimal, a more accurate temperature measurement of the current design could be obtained by inserting Pt1000 sensors directly into a non-functional PDMS wafer chip containing nonconductive TMC. Alternatively, the design could incorporate sensors within a separate microchannel adjacent to the main flow channels, thereby accounting for variations in PDMS thickness between chips.

Tomasz Glawdel and Ren [72] measured the temperature within microchannels using fluorescence thermometry with Rhodamine B (RhB). This technique involves introducing a temperature-sensitive RhB solution into the microchannels, as fluorescence intensity decreases with increasing temperature. However, since RhB tends to adsorb onto PDMS surfaces, continuous photobleaching is required during measurement to reduce background fluorescence and obtain accurate temperature readings.

To better ensure an increase in specificity of primer annealing, the primer length could also be changed. In a paper by Montera and Nicoletti [73], it is described how non-specific

annealing is more likely to occur when using shorter primers. The primers pET11a1rev and pET11a2rev are both 18 nucleotides, within the recommended 18–30 nucleotides in length. However, they are the smallest recommended size, and a choice of longer primers may have been prudent for better primer hybridization. [73]

5.2.2 Inhibition

As shown in figure 4.25a, *Taq* polymerase was inhibited in the chip. Reamplification with the addition of new polymerase resulted in a large quantity of nonspecific amplification products as compared to the same procedure, but with the addition of DNA template instead.

The choice of materials used for the chips was made to minimize potential inhibition of PCR components, as PDMS, Pyrex, and silica are known to exhibit low inhibitory effects, as shown in figure 1.5. Two common approaches to reduce inhibition include washing or incubating a surface-passivating agent within the chip, or adding the agent directly to the PCR mixture. Both strategies were tested in this project.

Although previous studies have demonstrated that BSA can act as a competitive inhibitor of adsorption and improve PCR performance, testing with 1 mg/mL BSA (figure 4.23) produced no detectable amplification. It is possible that higher concentrations of BSA could have mitigated inhibition more effectively, as other studies have used up to 2.5 mg/mL BSA in PCR mixtures.[43, 74] Given that each chip may have unique surface properties, testing a range of BSA concentrations could help identify optimal conditions for consistent amplification.

A washing step using 10 mg/mL BSA, followed by PCR with 0.6 mg/mL BSA in the reaction mixture, produced a visible but nonspecific amplification product (figure 4.24). This suggests that inhibition was sufficiently reduced to allow partial amplification and that proper heating of the chips might enable generation of the desired target product. To ensure effective BSA adsorption, prior to introducing the PCR mixture, the BSA solution could be incubated within the microchannels. Chen and Qiu [43] and J M Haber [75] performed up to one-hour incubations to achieve sufficient surface passivation. However, this approach is time-consuming and therefore not ideal for routine use.

Another possible source of inhibition may lie outside the wafer chip itself, arising instead from the hydrophobic PTFE tubing and/or the injection loop. To minimize potential adsorption of *Taq* polymerase and dNTPs, Peham *et al.* [76] used a 1 mg/mL BSA solution wash solution before the PCR mixture. However, since the majority of the surface area in contact with the PCR mixture resides within the chip, it is likely that the chip remains the primary source of inhibition.

5.2.2.1 PCR Microdroplets

The chip design could be modified to better mitigate PCR inhibition. Zhang and Jiang [77] proposed using PCR microdroplets, which can reduce inhibition and contamination by compartmentalizing the reaction. This approach also enables digital PCR, in which

NB4 5. Discussion

each droplet contains one, very few, or no template molecules. As a result, undesirable amplification can be confined to specific droplets, potentially improving overall reaction specificity and amplification.

Conclusion 6

Three continuous-flow PCR chips were successfully designed and fabricated using a silicon mold to engrave microchannels into PDMS, which were then plasma-treated and sealed with Pyrex and silica wafers. The fabricated chips featured channel widths of 90 μm and depths of 48, 76, and 87 μm , respectively. The PCR mixture was introduced through an injection loop and driven by both aqueous and oil phases to the chip by a syringe pump.

Simulations of the design indicate that a stable extension temperature of $72^{\circ}\text{C}\pm0.274$ is achievable by leveraging the gradient between the annealing and denaturation zones. The pressure drop across the channel prevents the use of conventional oils for driving the flow, which could be remedied with larger channels.

Although the primary goal of the project was to develop functional continuous-flow PCR chips to use as a basis to generate high-throughput mutant libraries, testing with a custom-built heating system revealed significant *Taq* polymerase inhibition and nonspecific amplification. These effects were likely amplified by the small channel dimensions and suboptimal temperature control within the PDMS channels. Inhibition could be partially mitigated by applying a BSA washing solution prior to introducing the PCR mixture into the wafer chips.

Potential design modifications to address PDMS delamination and improve environmental safety were discussed. Additionally, surface passivation strategies were considered based on findings from previous studies to further reduce inhibition and improve PCR performance in future designs.

Bibliography

- [1] J. D. Kaunitz, "The discovery of PCR: Procurement of divine power," *Dig Dis Sci.*, vol. 60, no. 8, pp. 2230–2231, 2015.
- [2] A. M. Christian D. Ahrberg and B. G. Chung, "Polymerase chain reaction in microfluidic devices," *Lab on a Chip*, 20 2016.
- [3] S.-F. M. Joe G N Garcia, "Polymerase chain reaction: A landmark in the history of gene technology," *Critical Care Medicine*, vol. 33, pp. 429–432, 12 2005.
- [4] Y. I. Sonoko Ishino, "Dna polymerases as useful reagents for biotechnology the history of developmental research in the field," *Frontiers in Microbiology*, vol. 5, 2014.
- [5] E. Navarro, G. Serrano-Heras, M. J. Castaño, and J. Solera, "Real-time PCR detection chemistry," *Clinica Chimica Acta*, vol. 439, pp. 231–250, 2015.
- [6] E. M. Elnifro, A. M. Ashshi, R. J. Cooper, and P. E. Klapper, "Multiplex PCR: Optimization and application in diagnostic virology," *Clinical Microbiology Reviews*, 2000.
- [7] R. Chen, "Enzyme engineering: Rational redesign versus directed evolution," *Trends in Biotechnology*, vol. 19, pp. 13–14, 1 2001.
- [8] K. M. Poluri and K. Gulati, *Protein Engineering Techniques Gateways to Synthetic Protein Universe* (SpringerBriefs in Forensic and Medical Bioinformatics). Springer Nature Singapore Pte Ltd., 2017, pp. 27–30.
- [9] H. Zhu et al., "Pcr past, present and future," BioTechniques, vol. 69, 4 2020.
- [10] I. S. P. Nimrat Khehra and M. Zubair, "Polymerase chain reaction (pcr)," *StatPearls* [*Internet*], vol. 5, 2025.
- [11] X.-N. Li *et al.*, "Rna sequencing reveals the expression profiles of circrna and indicates that circddx17 acts as a tumor suppressor in colorectal cancer," *Journal of Experimental & Clinical Cancer Research*, vol. 37, 325 2018.
- [12] J. Y. Jung *et al.*, "Rapid oral bacteria detection based on real-time pcr for the forensic identification of saliva," *Scientific Reports*, vol. 8, 10852 2018.
- [13] D. Marsic *et al.*, "Pcr-based gene synthesis to produce recombinant proteins for crystallization," *BMC Biotechnol.*, vol. 8, 44 2008.
- [14] P. J. Carter, "Introduction to current and future protein therapeutics: A protein engineering perspective," *Experimental Cell Research*, vol. 317, pp. 1261–1269, 9 2011.
- [15] W. Xiong *et al.*, "Protein engineering design from directed evolution to de novo synthesis," *Biochemical Engineering Journal*, vol. 174, pp. 13–14, 108096 2021.

- [16] H. Xu, E. I. Petersen, S. B. Petersen, and M. R. El-Gewely, "Random mutagenesis libraries: Optimization and simplification by PCR," *BioTechniques*, vol. 27, pp. 1102–1108, 1999.
- [17] G. O. Ndochinwa *et al.*, "New advances in protein engineering for industrial applications: Key takeaways," *Open Life Sci.*, vol. 19, 1 2024.
- [18] A. Hoffmann, A. Timm, C. Johnson, *et al.*, "Automation of customizable library preparation for next-generation sequencing into an open microfluidic platform," *Scientific Reports*, vol. 14, 1 2024.
- [19] C. Zhang *et al.*, "Pcr microfluidic devices for dna amplification," *Biotechnology Advances*, vol. 24, no. 3, pp. 243–283, 2006.
- [20] S. Li *et al.*, "A continuous-flow polymerase chain reaction microchip with regional velocity control," *J Microelectromech Syst.*, vol. 15, no. 1, pp. 223–236, 2009.
- [21] M. Kopp *et al.*, "Chemical amplification: Continuous-flow PCR on a chip," *SCIENCE*, vol. 280, no. 5366, pp. 1046–1048, 1998.
- [22] B. Yang *et al.*, "A continuous flow PCR array microfluidic chip applied for simultaneous amplification of target genes of periodontal pathogens," *Lab Chip*, vol. 22, pp. 733–737, 2022.
- [23] K. T. L. Trinh and N. Y. Lee, "Glass-polytetrafluoroethylene-glass based sandwich microdevice for continuous-flow polymerase chain reaction and its application for fast identification of foodborne pathogens," *Talanta*, vol. 176, pp. 544–550, 2018.
- [24] J. Chen *et al.*, "One-heater flow-through polymerase chain reaction device by heat pipes cooling," *Biomicrofluidics*, vol. 9, no. 1, 2015.
- [25] M. Bu *et al.*, "Design and theoretical evaluation of a novel microfluidic device to be used for PCR," *Journal of Micromechanics and Microengineering*, 2003.
- [26] P. O. Yonghao Zhang, "Microfluidic dna amplification—a review," *Analytica Chimica Acta*, vol. 638, no. 2, pp. 115–125, 2009.
- [27] N. Coccaro *et al.*, "Digital pcr: A reliable tool for analyzing and monitoring hematologic malignancies," *J. Mol. Sci.*, vol. 21, 9 2020.
- [28] Z. Li *et al.*, "A rapid and low-cost platform for detection of bacterial based on microchamber pcr microfluidic chip," *Biomedical Microdevices*, vol. 26, 20 2024.
- [29] J. C. Layton and P. L. Foster, "Error-prone dna polymerase iv is controlled by the stress-response sigma factor, rpos, in escherichia coli.," *Molecular microbiology*, vol. 50, pp. 549–561, 2 2003.
- [30] A. Gonzalez *et al.*, "Interaction of quantitative PCR components with polymeric surfaces," *Biomed Microdevices*, 2007.
- [31] R. Kodzius *et al.*, "Inhibitory effect of common microfluidic materials on PCR outcome," *Sensors and Actuators B: Chemical*, 2012.
- [32] S. Maddocks and R. Jenkins, *Understanding PCR: A Practical Bench-Top Guide*. Elsevier Inc, 2017, pp. 1–30.
- [33] C. D. Kuslich, B. Chui, and C. T. Yamashiro, "Overview of pcr," *Current Protocols Essential Laboratory Techniques*, 2018.

NB4 Bibliography

[34] J. M. Berg et al., Biochemisstry. W. H. Freeman & Company, 2015, pp. 105–134, 827–858.

- [35] W. Xu, Basic Rules in Nucleic Acid-Mediated Amplification and Hybridization Methods in Food Safety Detection: A Review. Springer, 2025, pp. 39–67.
- [36] van Pelt-Verkuil et al., Principles and Technical Aspects of PCR Amplification. Springer, 2008, pp. 103–107.
- [37] J. M. T. A Chien D B Edgar, "Deoxyribonucleic acid polymerase from the extreme thermophile thermus aquaticus," *J Bacteriol* 127, 1976.
- [38] S. O. Lee and S. D. Fried, "An error prone pcr method for small amplicons," *Analytical Biochemistry*, vol. 628, p. 114266, 2021.
- [39] A. K. Vashishtha, J. Wang, and W. H. Konigsberg, "Different divalent cations alter the kinetics and fidelity of dna polymerases*," *Journal of Biological Chemistry*, vol. 291, no. 40, pp. 20869–20875, 2016.
- [40] T. B. Christensen *et al.*, "Multiplex polymerase chain reaction (PCR) on a su-8 chip," *Microelectronic Engineering*, 2008.
- [41] T. B. Christensen *et al.*, "PCR biocompatibility of lab-on-a-chip and mems materials," *Journal of Micromechanics and Microengineering*, 2007.
- [42] H. J. Crabtree *et al.*, "Inhibition of on-chip pcr using pdms–glass hybrid microfluidic chips," *Microfluidics and Nanofluidics*, vol. 13, pp. 383–398, 2012.
- [43] J. J. Chen and X. C. Qiu, "The effect of the surface passivation on polymerase chain reaction inside a continuous flow microfluidic chip," *Microsystem Technologies*, vol. 31, pp. 25–43, 2025.
- [44] N. Ramalingam *et al.*, "Acetylated bovine serum albumin differentially inhibits polymerase chain reaction in microdevices," *Biomicrofluidics*, vol. 11, no. 3, 2017.
- [45] C. Zhang and D. Xing, "Miniaturized PCR chips for nucleic acid amplification and analysis: Latest advances and future trends," *Nucleic Acids Res.*, vol. 35, no. 13, pp. 4223–4237, 2007.
- [46] H. J. Levinson, *Principles of Lithography* (SID Series in Display Technology), 2ed. SPIE-The International Society for Optical Engineering, 2005, pp. 1–6, 53–69, 79–83, 123.
- [47] J. Souk *et al.*, *Flat Panel Display Manufacturing* (SID Series in Display Technology), 1st. Wiley, 2018, pp. 287–328.
- [48] DTU. "Dtu nanolab tpt: Lithography co 56t10 jan2021." Course Accessed Through "learn.inside.dtu.dk. ().
- [49] L. D. Nanolab. "Specific process knowledge/lithography/mir." Course Accssed Through "labadviser.nanolab.dtu.dk". ().
- [50] H. Ito, "Chemically amplified resists: Past, present, and future," in *MICROLITHOG-RAPHY* '99, 1999.
- [51] DTU. "Dtu nanolab tpt: Dry etch co 56t40 fall2020." Course Accssed Through "learn.inside.dtu.dk. ().

- [52] K. Nojiri, *Mechanism of Dry Etching*. Springer Cham Heidelberg New York Dordrecht London, 2012, pp. 11–30.
- [53] H. Jansen *et al.*, "A survey on the reactive ion etching of silicon in microtechnology," *J. Micromech. Microeng.* 6, pp. 14–28, 1996.
- [54] M. Huff, "Recent advances in reactive ion etching and applications of high-aspectratio microfabrication," *Micromachines*, *12*(8), *991*, 2021.
- [55] G. S. N Roxhed P Griss, "A method for tapered deep reactive ion etching using a modified bosch process," *J. Micromech. Microeng.* 17, 2007.
- [56] V. T. H. Nguyen *et al.*, "Ultrahigh aspect ratio etching of silicon in sf6-o2 plasma: The clear-oxidize-removeetch (core) sequence and chromium mask," *Journal of Vacuum Science & Technology A*, 2020.
- [57] R. L. Bates *et al.*, "Silicon etch using sf6/c4f8/ar gas mixtures," *J. Vac. Sci. Technol. A 32*, 2014.
- [58] B. Yang *et al.*, "Simultaneous amplification of dna in a multiplex circular array shaped continuous flow pcr microfluidic chip for on-site detection of bacterial," *Lab Chip*, vol. 23, pp. 2633–2639, 11 2023.
- [59] A. Mohammed, A. Adeniyi, and A. Hassan, "Modelling of serpentine continuous flow polymerase chain reaction microfluidics," *International Journal of Engineering Science and Technology (IJEST)*, vol. 4, pp. 1183–1189, Mar. 2012.
- [60] D. B. Kolesky, R. L. Truby, A. S. Gladman, and J. A. Lewis, "3d-bioprinting of vascularized, heterogeneous cell-laden tissue constructs," *Lab on a Chip*, vol. 16, no. 12, pp. 2202–2211, 2016.
- [61] G. De Bellis, M. Pompili, and M. Sarto, "Temperature dependence of the shear viscosity of mineral oils and natural esters," in *IEEE 20th International Conference on Dielectric Liquids*, Jun. 2019, pp. 1–4.
- [62] T. Industries, *Tmc-3283 electronic liquid*, Accessed 13 Oct. 2025. Available: https://tmcindustries.com/.
- [63] N. Y. Lee, "A review on microscale polymerase chain reaction based methods in molecular diagnosis, and future prospects for the fabrication of fully integrated portable biomedical devices," *Microchimica Acta*, vol. 185, 285 2018.
- [64] S. Li *et al.*, "A continuous-flow polymerase chain reaction microchip with regional velocity control," *ournal of Microelectromechanical Systems*, vol. 15, pp. 223–236, 1 2006.
- [65] S. Gao *et al.*, "Overcoming bubble formation in polydimethylsiloxane-made pcr chips: Mechanism and elimination with a high-pressure liquid seal," *Microsyst Nanoeng*, vol. 10, 1 2024.
- [66] S. Bhattacharya, A. Datta, J. Berg, and S. Gangopadhyay, "Studies on surface wettability of poly(dimethyl) siloxane (pdms) and glass under oxygen-plasma treatment and correlation with bond strength," *Journal of Microelectromechanical Systems*, vol. 14, no. 3, pp. 590–597, 2005.

NB4 Bibliography

[67] Q. Cao, M. Kim, and C. Klapperich, "Plastic microfluidic chip for continuous-flow polymerase chain reaction: Simulations and experiments," *Biotechnology Journal*, vol. 6, 2 2011.

- [68] K. Kang *et al.*, "Fabrication of truly 3d microfluidic channel using 3d-printed soluble mold," *Biomicrofluidics*, vol. 12, 2018.
- [69] W. H. Goh and M. Hashimoto, "Dual sacrificial molding: Fabricating 3d microchannels with overhang and helical features," *Micromachines*, vol. 9, 10 2018.
- [70] J. Lachaux *et al.*, "Thermoplastic elastomer with advanced hydrophilization and bonding performances for rapid (30 s) and easy molding of microfluidic devices," *Lab on a Chip*, vol. 17, p. 2581, 2017.
- [71] A. H. McMillan, E. K. Thomée, A. Dellaquila, H. Nassman, T. Segura, and S. C. Lesher-Pérez, "Rapid fabrication of membrane-integrated thermoplastic elastomer microfluidic devices," *Micromachines*, vol. 11, no. 8, 2020.
- [72] S. W. Tomasz Glawdel Zeyad Almutairi and C. Ren, "Photobleaching absorbed rhodamine b to improve temperature measurements in pdms microchannels," *Lab Chip*, vol. 9, pp. 171–174, 2009.
- [73] L. Montera and M. C. Nicoletti, "The pcr primer design as a metaheuristic search process," in *Artificial Intelligence and Soft Computing ICAISC 2008*, L. Rutkowski, R. Tadeusiewicz, L. A. Zadeh, and J. M. Zurada, Eds., Springer Berlin Heidelberg, 2008, pp. 963–973.
- [74] J. N. Pham *et al.*, "Fabrication of 3d continuous-flow reverse-transcription polymerase chain reaction microdevice integrated with on-chip fluorescence detection for semi-quantitative assessment of gene expression," *Analyst*, vol. 143, pp. 5692–5701, 2018.
- [75] K. S. J M Haber P R Gascoyne, "Rapid real-time recirculating pcr using localized surface plasmon resonance (lspr) and piezo-electric pumping," *Lab Chip*, vol. 17, pp. 2821–2830, 16 2017.
- [76] J. R. Peham *et al.*, "Long target droplet polymerase chain reaction with a microfluidic device for high-throughput detection of pathogenic bacteria at clinical sensitivity," *Biomedical Microdevices*, vol. 13, pp. 463–473, 2011.
- [77] Y. Zhang and H.-R. Jiang, "A review on continuous-flow microfluidic pcr in droplets: Advances, challenges and future," *Analytica Chimica Acta*, vol. 914, pp. 7–16, 2016.

A.1 GeneJET Plasmid Miniprep Kit

This is the protocol used for plasmid isolation from cells. The cell tube has already been incubated overnight at 37° C. The contents of the tube are transferred into a 15 mL tube with a screw lid for easier centrifugation and is centrifuged at 6° C at 6.000 rpm for 7 minutes. The supernatant is discarded leaving the cell pellet facing upward in the tube.

Step 1:

250 μ L Resuspension Solution is added into the 15 mL tube with the pellet and vortex.

The supernatant is transferred into an Eppendorf tube and 250 μ L Lysis solution is added to the tube and inverted 6 times. 350 μ L Neutralization Solution is added and again inverted 6 times. This is centrifuged for 10 minutes at 12.000 rpm.

Step 2:

Transfer only the supernatant to the Thermo Scientific GeneJET spin Column (as pellet fragments may clock up the filter). This is done with a pipet. The liquid is centrifuged for 1 minute at 12.000 rcf through the GeneJET spin Column filter and the eluate is discarded. If there is not enough room for all the eluate to flow through, the eluate is discarded and the tube is centrifuged again.

Step 3:

Add 500 μ L of Wash Solution and centrifuge for 1 minute at 12.000 rcf.

Discard the flow through. This is repeated.

Centrifuge the empty column tube for 1 minute at 12.000 rcf.

Step 4:

Transfer the column into a new tube.

Add 50 μ L Elution Buffer to the column and incubate for 2 minutes Centrifuge for 2 minutes (the Eppendorf lid can be orientated so it matches the counterweight) at 12.000 rcf. The flowthrough is collected in a new Eppendorf tube.